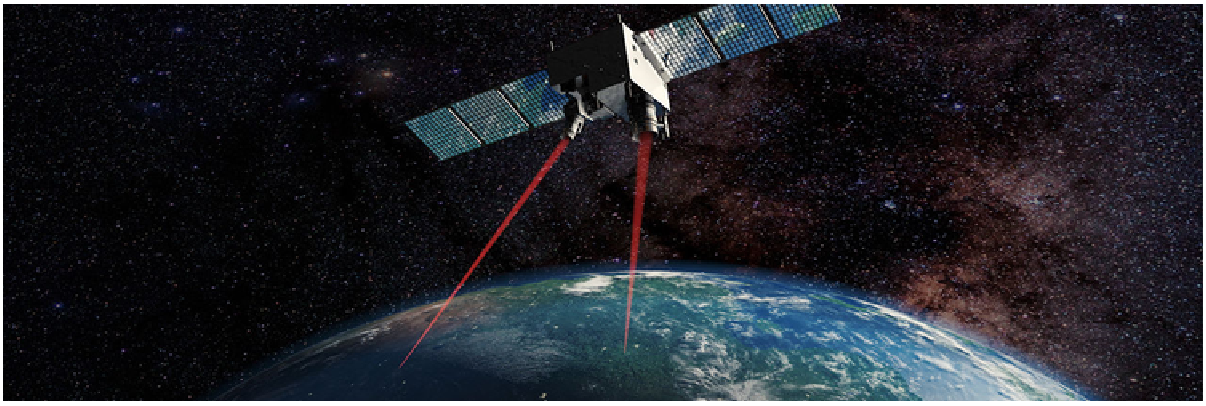

End-to-end simulation of satellite based quantum key distribution

Vladlen Galets’Ky

Thesis to obtain the Master of Science Degree in

Engineering Physics

Supervisors: Prof. Manfred Niehus
Prof. João Carlos Carvalho de Sá Seixas

Examination Committee

Chairperson: Prof. Pedro Miguel Félix Brogueira
Supervisor: Prof. Manfred Niehus
Members of the Committee: Prof. Vítor Manuel dos Santos Cardoso
Dr. Nuno Alexandre Peixoto Silva

December 2021

Acknowledgments

Ad astra per aspera[1] is one of the main principles being defended in this thesis and in my on going professional career. Being here, would not be possible without my parents, thus I want to thank them personally and acknowledge it in my mother tongue:

Родители, без вашего терпения, труда и поддержки я не смог бы стать кем я всегда хотел. Я горжусь вами и буду вас всегда любить и уважать. Спасибо вам за всё.

I would also like to thank my dear friends: Raul Santos, Miguel Gonçalves, Francisco Mendonça, Sofia Monteiro, Mariana Pliças, Tiago Terenas, Joaquim Quadrado, Luis Parreira and Madalena Pereiro, for all the time and support that was given. They were there to reason with all my thoughts and hardships, they were there when I was in my most vulnerable stages of my life making me into who I am now. Maria Faria, even in the darkest of days you showed me that there is always light coming from the stars. Even though time flows differently when I am with you, I will treasure every second of it and I am grateful for that.

I would also like to show my gratitude to Dr. Manfred Niehus, Dr. Ilidio Lopes and Dr. Joao Seixas. Without their patience and time the current work of my thesis would not be possible. As a student I would like to thank my university, collegues and professors for all the experience given challenging my capabilities to another level.

Thank you all for everything

---

[1] From Lucius Annaeus Seneca meaning "through hardships to the stars".

Resumo

Neste trabalho iremos simular uma missão de distribuição de chave quântica (QKD) para Cubesats em ligacões descendentes para os protocolos BB84 e E91. Este simulador foi desenvolvido durante as fases de análise de viabilidade e design preliminar do ciclo de vida do projecto do QuantSat-PT. Considerando o estado da arte em QKD, identificou-se incoerências em perdas de sinal devido à turbulência e atenuações atmosféricas. Assim, este trabalho incentiva um estudo alargado nesse domínio. Como produto da análise, obteve-se para o protocolo BB84 a taxa de sinal de 32.1 kbit/s e QBER de 4% para o zênite de uma orbita de Cubesat de 750 km. Para o protocolo E91, fez-se o teste do Clauser, Horne, Shimony e Holt (CHSH) simulando um circuito quântico com perdas de sinal, obtendo-se um coeficiente de correlação no zênite de $S \in [-2.63 \pm 0.02, -1.91 \pm 0.03]$. Todos os resultados apresentados neste trabalho estão coerentes com o estado da arte em QKD.

Para protocolos dependentes de fase há uma perda de sinal adicional que perturba a frente de onda ao propagar-se ao longo da atmosfera. Como tal, neste trabalho propoem-se um método novo de correção de perfis de intensidade de sinais baseando-se num algoritmo cíclico e fechado usando uma rede neural convolucional com ótica adaptativa. Este método proposto consegue recuperar até 93.12% do perfil da imagem original, contribuindo fortemente para a qualidade do sinal.

Palavras - Chave

Simulação de QKD, Ligações descendentes em Cubesats, Turbulência, Comunicação ótica, CNN

Abstract

We simulate a satellite Quantum Key Distribution (QKD) downlink which was created during the concept development and preliminary design completion phases of the QuantSat-PT project mission life cycle. We shall consider in great detail all the losses for the mission accordingly to the defined requirements, with special attention to the turbulent and atmospheric losses for BB84 and E91 protocols which remained inconsistent with real data. We have obtained for the BB84 protocol a sifted key rate and Quantum Bit Error Rate (QBER) of 32.1 kbit/s and 4% at zenith respectively for a 750 km orbit. For the E91 protocol the Clauser, Horne, Shimony and Holt (CHSH) test was performed obtaining a correlation factor of $S \in [-2.63 \pm 0.02, -1.91 \pm 0.03]$ for the mission. All results are consistent with the state of the art simulators and experiments in field of QKD.

For phase-dependent protocols a new Convoluted Neural Networks (CNN) algorithm is proposed, to recover the disturbed intensity profiles of the signal at the ground station with the use of Adaptive Optics (AO), improving up to an order of magnitude the mean square error between the disturbed images and the corrected ones.

Keywords

QKD simulation, Cubesat downlink, Turbulence modelling, Optical communications, CNN

Contents

List of Figures

List of Tables

Acronyms

ADCS	Attitude Determination and Control System
ANN	Artificial Neural Networks
AO	Adaptive Optics
ATP	Acquisition, Tracking and Pointing
CDH	Command and Data Handling
CHSH	Clauser, Horne, Shimony and Holt
CNN	Convoluted Neural Networks
COMS	Communications system
CV-QKD	Continuous Variable Quantum Key Distribution
DNB	Day and Night Band
DoP	Degree of Polarization
EPS	Electronic Power System
FoV	Field of View
GDO	Gradient Descent Optimization
GNSS	Global Navigation Satellite System
GS	Ground Station
IR	Infrared Range
IT	Institute of Telecommunications
LEO	Low Earth Orbit
ME	Mean Error
MPN	Mean Photon Number
MSE	Mean Square Error

OAM	Orbital Angular Momentum
OBC	On-Board Computer
PDF	Probability Distribution Function
PDTC	Probability Distribution Transmission Coefficient
PSF	Point Spread Function
QBER	Quantum Bit Error Rate
QKD	Quantum Key Distribution
RAAN	Right Ascension of the Ascending Node
RF	Radio frequency
RSA	Rivest–Shamir–Adleman
RTE	Radiative Transfer Equation
S/C	Spacecraft
SLM	Spatial Light Modulators
SNR	Signal to Noise Ratio
SPD	Single Photon Detector
SPS	Single Photon Source
TRL	Technology Readiness Level

1

Introduction

1.1 Classical cryptography turns Quantum

Modern cryptography plays an essential role for the security of the transmission of information. Encryption, authentication and signature scheme processes favor users to stay protected from classical attackers. Most of these protocols are based on Rivest–Shamir–Adleman (RSA) [10,11] method, where the pillar of encryption is primarily centered on factorization, the discrete logarithmic and eliptic-curve discrete logarithmic problems.

Recent advances in quantum computing [12] performed by Google quantum AI claimed to reach for the first time quantum supremacy in 2019 [13]. More recently in 2021 by studying a new series of *Quantum Falcon* processors, IBM increased the quantum volume of circuits to 64 for their current architecture [14]. Moreover in the same year, it has been claimed that the superconducting quantum processor, *Zuchongzhi*, also achieved quantum supremacy [15] creating an opening for a new era of quantum computing. However, to this day, no architecture reaches more than 127 qubits [16]. Assuming that in the next years a powerful quantum computer reaches an order of twenty billion qubits, by running Shor's or Grover's algorithm [17] it will lead to a collapse of most modern classical public key cryptosystems. Despite of existing symmetric key algorithms that are resistant to quantum computation attacks (AES-256) [18], not all of them share this trait. As this reality may not be far so distant, the reader may start to feel concerned about his own data protection, wondering how fragile may our current classical cryptography be, to be challenged by these quantum systems when one day they become a threat.

Two main solutions were found that offered to restore security and confidentially of the information even with eavesdropping, post-quantum cryptography and Quantum Key Distribution (QKD). The former [17], looks into a specific category of classical cryptosystems based on symmetric algorithms and hash functions that provide fidelity against quantum computers. The latter [19–21], applies the rules of the quantum computers against themselves, using the uncertainty principle and entanglement of states [22]. For this thesis we will be focusing on this solution.

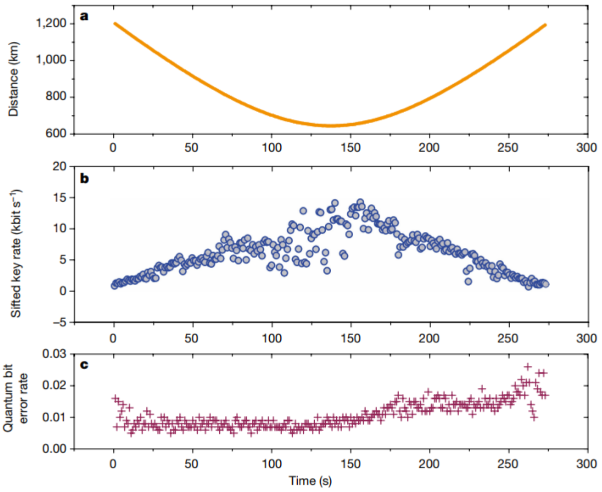

Figure 1.1: Image taken from [1]. **a)**: The trajectory of the Micius satellite measured from Xinglong Ground Station (GS). **b)**: The sifted key rate as a function of time and physical distance from the satellite to the station. **c)**: Observed Quantum Bit Error Rate (QBER).

The state of the art technologies in QKD unravel numerous of problems still to be addressed in this field, namely the trade off between security, distance and secret key rates influencing the practicality of such state of the art systems. Another major problem is authentication [23] which is crucial to be performed in untrusted channels. One of the end goals of QKD, relies on space to ground application for the quantum key exchange, as we will see in the next section.

1.2 QKD on satellites

In order to globalize the protection to exchange information, a solution via a satellite link to ground is performed. Uplink and downlink quantum key exchanges are performed from the GS to Spacecraft (S/C) and S/C to GS respectively. They are significantly different [24], and should be considered depending on the different needs of the mission. A downlink considers that the optical apparatus is located in the payload, leading to heavier requirements in the mass, energy consumption and higher risks. Therefore, an additional need appears to test the maturity of the setup within the space environment increasing the Technology Readiness Level (TRL) classification of the optical subsystem. Furthermore, this approach is more challenging due to constant satellite drifts and pointing errors. On the other hand for an uplink, the information transmission is more stable however the atmospheric and turbulent effects are more dominant thus decreasing the average key rate and QBER.

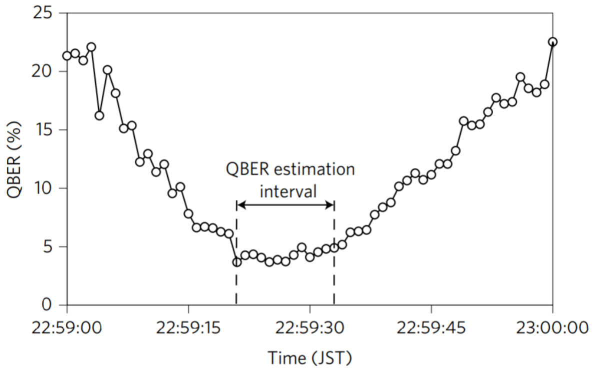

Figure 1.2: Image taken from [2]. Variation of the QBER in the emulated B92 protocol for a 1 min duration on 5 August 2016 for SOCRATES mission.

Even with this requirements the state of the art missions proved that key distribution under this circumstances is still viable as stated by Micius and SOCRATES. Micius was successfully launched on August 2016 [1] from Jiuquan, China, and now orbits at an altitude of about 500 km in LEO. One of the satellite payloads had a BB84 decoy-state [25] QKD transmitter at a wavelength of 850 nm cooperating with Xinglong ground observatory station. At optimal distance of 600 km, it achieved a QBER $\sim$ 2$\%$ and a sifted key of 14 kbps as seen in Fig 1.1. In 2017 the mission concept went onto a second phase [1], establishing a space-to-ground two-downlink channel creating a 1200 km distance QKD between two GS (Nanshan and Delingha), however, a secured node configuration was assumed, meaning that no Eve was present (QBER $\sim$ 8.1$\%$ with sifted key rate of 1.1 Hz). The measured overall two-downlink channel attenuation was at peak 82 dB which was more than predicted. In 2020 this mission was the first to achieve a non-secure node configuration [26], assuming that Eve could be present between the two ground stations. QBER dropped to 4.5$\%$ due to optical optimizations at the ground, therefore, enabling the realization of satellite-based entanglement QKD.

On the other hand, SOCRATES micro-satellite was first launched in 2014, with the main objective of technology demonstration for position and attitude control. SOTA, lasercom payload, had a secondary mission in 2016 of creating a B92-like QKD protocol at 800-nm band to perform the first-time quantum limited demonstration from space. For the B92 protocol [25] an emulated QBER $\in [3, 6]\%$ was obtained as can be seen in Fig 1.2. From the results given [2], it's mentioned that the total loss budgets from the simulation analysis and the real data losses received were off from a range of 29.5 dB to 13.8 dB. Thus, pointing to unmet simulation conditions for QKD analysis due to the complexity of the problem in study. In the article, these values are attributed to atmospheric scintillation, which typically could change losses by that order of magnitude, hence the thesis being incentivized for a more detailed study on the turbulence influence for the quantum laser communications.

1.3 State of the art QKD simulators

In order to have a better understanding of the motivation for the approach taken during this thesis a diverse number of state of the art simulators are presented. Mainly from the Bourgoin et al [24], QUARC [27], Carlo Liorni et al. [28] and statistical methods [29, 30].

Burgoin et al. simulated and calculated the expected performance for a year-long 600 km satellite conducting a QKD link at 670 nm for a sun-synchronous orbit implementing a decoy state BB84 protocol. A Rayleigh–Sommerfeld diffraction [31] was considered with a custom beam profile with a convoluted pointing error. MODTRAN [32] was used for the atmospheric attenuation calculation, artificial and natural background was considered. An in-depth comparison between up-link and downlink approaches were also performed. For a 600 km downlink, considering a beam waist of $w_0 = 0.05$ m and diameter of receiver of $D_R = 1.0$ m at the ground station (GS), the author's achieve a mean QBER of 4.3% between zenith angles of $\theta_{zen} \in [0, 70]$ deg. For high zenith angles it reaches up to 11%.

QUARC opted to simulate how a constellation comprising 15 low-cost 6U CubeSats with the BB84 protocol usage can form a secure communication backbone for ground-based and metropolitan networks across 43 GS in United Kingdom. It has an in-depth study of the satellite tracking and the telescope Field of View (FoV). Something of the utter importance for high precision laser communications to guarantee an optimal key rate. For a 574 km orbit, with a laser wavelength of 808 nm and assuming transmitter and receiver apertures of 0.090 m and 0.7 m respectively, the author's obtained a loss range from approximately 47 dB to 35 dB.

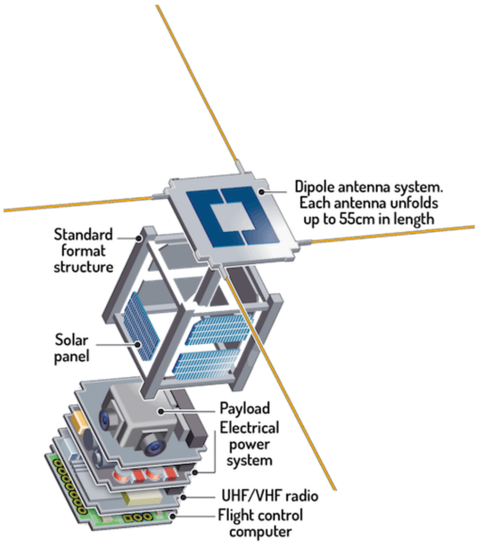

Figure 1.3: A standard structure for a 2U Cubesat. Image taken from [3].

A different take on the approach looks into Probability Distribution Transmission Coefficient (PDTC), a statistical interpretation for the off-pointing, turbulence disturbance and atmospheric effects. It examines the effect of channel fluctuations in Continuous Variable Quantum Key Distribution (CV-QKD), using in the simulator a derivation of the equations for the secret key rate over generic fading channels. Overall, for a 800 km orbit a downlink transmissivity of 1.8% is achieved.

Another method considers that imperfections from the truncation of the border in optical elements, conditions in the far field an additional broadening of the beam. Thus, it considers an imperfect quasi-

Gaussian beam in a turbulent environment characterized by a Probability Distribution Function (PDF) model. The author's work achieves for Cubesats a $QBER = 3\%$ at low zenith angles going up to $QBER = 14\%$ at zenith angles above $\theta_{zen} = 75\%$. The results on different approaches come close to the same order of magnitude.

1.4 What are Cubesats?

Cubesats are usually defined by their size and mass being within a range of 1–10 kg. For the QuantSat-PT mission a 2U (20x10x10 cm) architecture has been proposed. These nanosatellites, are recently becoming more popular due to the availability and low cost for companies and institutions to perform their research [33]. Their standardization, high degree of modularity as well as their extensive use leads the Cubesat projects to be readier to fly compared to other traditional satellite schedules. Typically, as seen in Fig 1.3, each Cubesat is composed by the On-Board Computer (OBC) system which controls the data flow and main operations in the satellite. Attitude Determination and Control System (ADCS) is a crucial subsystem which provides attitude and position determination of the S/C maintaining the stability and the accuracy of the off pointing of the payload and the Communications system (COMS) subsystems. Electronic Power System (EPS) is responsible for the energy levels of the Cubesat. For non active mission times, the satellite should perform in standby mode to lower its vital energy consumption. During this mode, only ADCS, EPS and OBC are powered up.

Command and Data Handling (CDH) subsystem should also be present and for QKD mission it is an essential component for key analysis from the transmitter, allowing to handle all information that is sent. The S/C payload is the heart of the mission. Usually for QKD missions this subsystem is composed by an optical apparatus and a telescope. Thus, allowing to encode information and propagate optically towards the GS.

1.5 Objectives and organization

As *I would rather have questions that cannot be answered than answers that cannot be questioned*, the purpose of the following work is to test, find and explore a possible Cubesat mission concept, where QKD can be demonstrated. Thus, this thesis focuses on the simulation and feasibility analysis of the Quantsat-PT project from Institute of Telecommunications (IT), having the ambition of creating the first ever QKD space mission in Portugal.

The main objective for the thesis is the generation of a possible mission concept, testing its parameters by demonstrating its feasibility for different QKD protocols resulting into additional constrains. We consider atmospheric and turbulent attenuations as well as the influence from background in order to

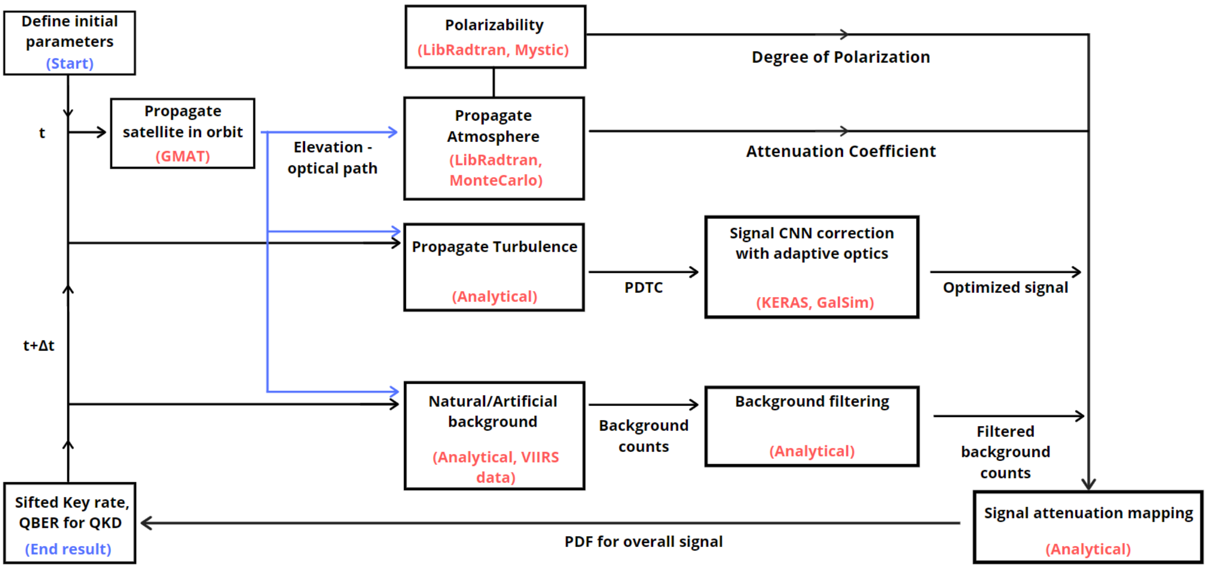

Figure 1.4: Architecture of the simulator. Tasks are defined for which below the method is provided as well as the output.

calculate the QBER and sifted key rate for each S/C elevation. The architecture used for the software is bottom-up, meaning that each chapter of this thesis will add a layer of complexity to the simulator, resulting into a top-level system.

The architecture of the simulator is defined in Fig 1.4. As seen, below each task a method is provided as well as the output parameters. It starts off with a random seed, propagating the atmosphere, turbulence and satellite position along the orbit. Monte-Carlo, statistical and analytical models provide an attenuation coefficient for each domain. In phase-dependent protocols, after the aberration of the signal's wave-front due to turbulence, a method is introduced using a closed feedback loop to correct with Convoluted Neural Networks (CNN) and adaptive optics the efficiency of the signal. As a result, for each time-step, key rates and QBER are calculated. Thus, end-to-end is defined as going all the way from a possible mission concept creation to the testing of different parameters at the GS and S/C in order to evaluate the feasibility of the mission, optimizing it.

The code has been written in Python, interchanging with Bash, C, C++ packages. At the beginning of each chapter the methodology is presented linking to a table of simulation parameters.

This work is organized as follows: In chapter 2 orbit is simulated and defined as well as some of the parameters for the payload and ground site. In chapter 3 the link between the satellite and ground is explained for the BB84 protocol [25], simulating the results geometrically. Furthermore, in chapter 4 background is estimated as well as some techniques are introduced for its own filtering. Background polarizability study will be also taken into account. In chapter 5 atmospheric effects are considered simulated with Monte-Carlo. An in-depth study of quantum laser performance in a turbulent domain is simulated for a better grasp for the sources of error in current QKD missions. The signal's Degree of Polarization (DoP) will be also analysed. In chapter 6 we study the influence of the three main dominant turbulent effects: scintillation, beam wandering and beam spreading on our signal. In chapter 7 a phase dependent study is performed, establishing a new closed feedback loop technique with convoluted neural networks to correct with adaptive optics the wave-front of the disturbed signal. In chapter 8 all the pieces fall together for an optical link budget performance, and by interpreting the final results we will come to a better understanding of the limits of QKD.

2

Mission concept

2.1 Requirements definition

If you wish to make an apple pie from scratch, you must first invent the universe [1]. We apply this ideology for our own purposes. In order to build a space mission we must first define the rules which it relies on by determining its own requirements.

We have selected for the simulator the most relevant requirements for the mission concept. They will influence directly on the performance and on its own structure.

Technical Requirements are defined in TR [01-04], Table 2.1. They often coexist with the basic needs of the mission to perform QKD. To emphasise, TR [02-04] are fundamental mission requirements that provide the basic needs to construct the simulator. Contractor requirements are present in CR [01-05], Table 2.1. They commonly differ from the first ones by being created for the specific needs of the mission. In our case they sub-categorize mainly into Operational and Environmental Requirements. Operational requirements add constrains on the QBER, defining that the mission uses a 2U Cubesat [34] which restricts the mass and size of the optical apparatus. It gives us an expected minimum duration of the

---

[1] From Carl Sagan, Cosmos

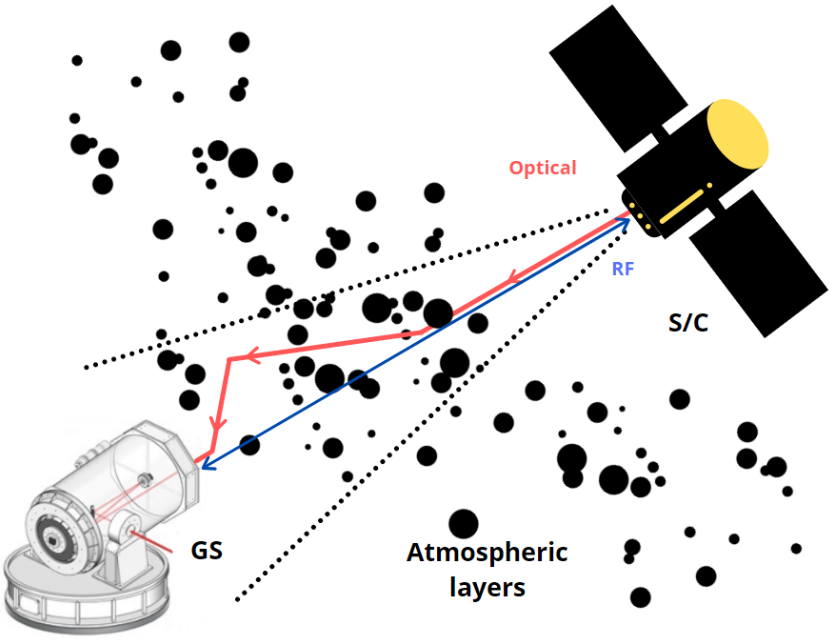

Figure 2.1: Schematic of the optical path for the QKD.

ID	Name	Text	Rationale
TR-01	Tracking	GS shall be able to track light from S/C with accuracy higher than 1.0×10^{-04} rad for FoV.	To diminish losses in key rate.
TR-02	Detection	GS shall be able to detect single photons from S/C.	To correctly distinguish the encoded information in QKD.
TR-03	Key sifting	GS shall be able to perform key sifting on the chosen QKD protocol.	To successfully perform QKD.
TR-04	Polarization Decoding	GS shall demultiplex polarization encoded photons.	To successfully perform polarization encoded QKD.
CR-01	Security	Mission shall be able to maintain secure communications with GS. QBER $< 11\%$ for BB84 and $S > 2$ for E91 (This being further explained in chapter 3)	To successfully perform QKD.
CR-02	Mission Duration	Mission shall prevail for a life-time of at least 3 years.	To acquire enough data to successfully study QKD.
CR-03	Size of Satellite	Mission's S/C shall be a 2U Cubesat (20x10x10 cm).	To test QKD on a nanosatellite.
CR-04	Ground Location	GS shall be defined in Alqueva, Portugal.	To account for the lowest artificial background environment.
CR-05	Time measurements	S/C shall pass-by GS at least once after 23:00 (GMT+1).	To account for the lowest natural background environment.

Table 2.1: Requirements that directly define the properties of the simulator.

mission. Environmental constrains optimize the key rate by defining an active time and a location for the mission, by minimizing the artificial and natural background. The structure for the requirements follows ECSS-E-ST-40C [35, 36] and IEEE 15288.2 [37] for ESA and NASA standardization procedures.

The schematic of the mission is defined in Fig 2.1. As seen, an optical downlink between S/C and GS is performed. Optical and Radio frequency (RF) links are needed to perform QKD. The first is used to send and exchange the encoded information between Alice and Bob for polarization/phase encoding, decoding it afterwards at GS. The latter is used to compare the quantum basis between S/C and GS, sharing it via a public channel (RF), thus shortening the key by sifting it.

2.2 Optical payload and Ground site

With the requirements defined, we encounter our first challenge that will follow through all chapters to come. What are *the right ingredients for our apple pie*? In other words, what guarantees me that the initial parameters used for the simulator are optimal for the mission in cause? The parameters are characterized by being either geometrically dependant, background dependant or hardware dependant. The latter one is based on the performance of the state of the art technologies available for QKD. The former two are the ones tested in the simulator and optimized for the key rate and QBER. For these, trial by error needs to be performed minimizing each parameter conditioned on cost, energy and size. This may sound challenging but *Nil desperandum*[2], as we will have a clearer view on the results in chapter 3.

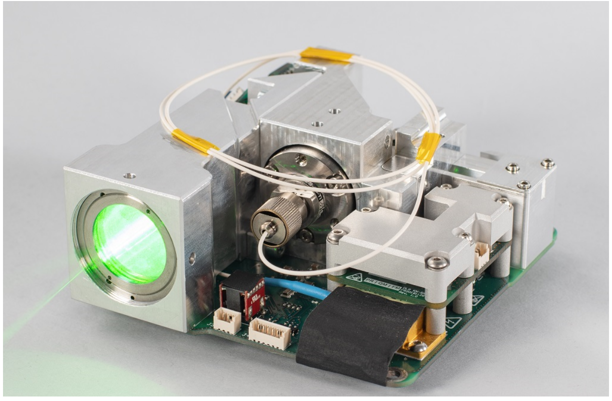

Figure 2.2: PIXL-1 payload named CubeLCT [4] launched on 24 January 2021 at 16:00 CET, image taken from [5].

Optical Payload

For the optical payload in Cubesats, one of the most pivotal parameters to be considered is the diameter of the transmitter (D_T). It's directly restrained by the requirement CR-03 from Table 2.1. Later in chapter 3 this parameter is studied, being dependent on the performance of the optical link.

A Single Photon Source (SPS) based on an attenuated laser was chosen for the optical payload,

---

[2] From Horace, 65-8 BC, meaning: "Never despair".

Parameters	Description	Units
D_T	0.03	m
Wavelength	850.0 ± 1.0	nm
Pulse rate	100.0	MHz
MPN	0.5	-
Optical efficiency (η_{opt})	0.5	

Table 2.2: Optical transmitter main parameters for simulator (S/C).

having the architecture based on CubeLCT one of the smallest QKD optical terminal up to date [4] as seen in Fig 2.2. Another approach is to choose an InGaN based single quantum emitter [38], which would optimize the photon statistics as a near ideal single photon source ($g^2(0) << 1$). However, the source is expensive as well as vulnerable to space-grade thermal oscillations being not so reliable for our purposes.

A wavelength of 850.0 ± 1.0 nm was selected for the mission due to the low attenuation coefficient for the transmission of the laser through the atmosphere [39] as seen in depth in chapter 5. In addition, reliable, high performance and inexpensive components are available such as the silicon avalanche photodiodes and advanced vertical cavity surface emitting laser technologies which operate at these range of wavelengths [40].

The pulse rate being highly dependent on the SPS was considered 100 MHz based on typical free-space optical communication missions. The Mean Photon Number (MPN) which considers the excitation rate per pulse, the optical efficiency and quantum efficiency are solely dependent on the hardware. Based on the work of L. Mazzarella et al. [27] their typical values can be obtained as seen in Table 2.2.

Ground site

As it was considered for the optical payload, the ground site is also highly dependent on the diameter of the receiver (D_R). However here, background dependant parameters also prevail such as the total and artificial brightness as seen by the requirements CR-04 and CR-05 from Table 2.1. The probability of the dark count is dependant on the thermal oscillations in the optical receiver, the ratio is estimated by the work of L. Mazzarella et al. [27] where every 10^5 received photons one of them is a dark count.

Geometrically the misalignment between the quantum basis on the S/C and GS is considered to have a mean error of 3.3% based on the work of the QUARC mission [27]. The field of view (FoV) follows the requirement of TR-01 from Table 2.1, being based on the performance of the telescope from the work of Emily Clements et al. [41]. In Table 2.3 the summary is presented for all the parameters used in GS simulation.

Parameters	Description	Units
D_R	2.0	m
Dark count probability (Y_0)	10^{-5}	-
Basis Misalignment (e_{det})	0.033	
Quantum efficiency (η_{quant})	0.4	
FoV	7.14×10^-4	rad
Total brightness	2.22×10^{-4}	cd m^{-2}
Artificial brightness	5.10×10^{-5}	
Latitude	38.21585	deg
Longitude	-7.58783	

Table 2.3: Optical receiver main parameters for simulator (GS).

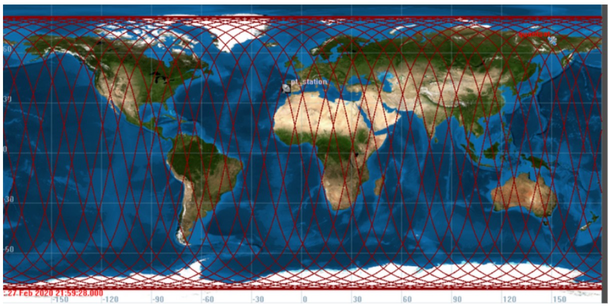

Figure 2.3: Ground track in GMAT representing the satellite propagation for 400 km in altitude.

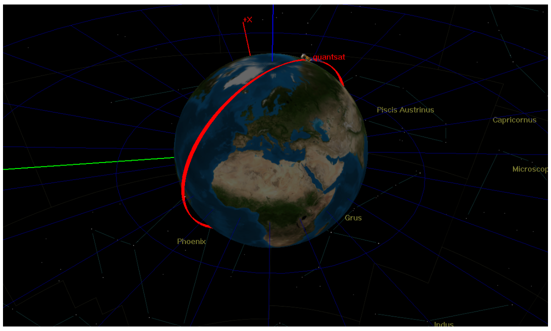

Figure 2.4: Orbit view of the satellite in red for 400 km in altitude.

2.3 Orbit definition

With the laws of our simulator defined, we start to propagate the geometric relation between the satellite and ground. Our objective here is to have a simplified understanding of how a Gaussian beam would be viewed at GS and what would be the performance of our protocol depending on the orbit and elevation taken.

In our case we use GMAT R2020a [3] in order to propagate and obtain the distance of the satellite with respect to ground. Either a numerical integrator type, or an ephemeris type propagator must be defined. In this thesis we have chosen a numerical type propagator due to the high accuracy that it provides. The choice made requires a force model to solve numerically the orbital equations of motion, containing spherical harmonic gravity models, atmospheric drag, solar radiation pressure, tide models, and relativistic corrections [42].

For the following simulator, a sun-syncronous orbit is established which allows for a regular revisit of the satellite during night-time. This formation guarantees an orbit periodicity of at least twice per night following requirement CR-05 in Table 2.1.

In order to optimize the orbit for the satellite, different sets of altitudes were chosen influencing directly

---

[3] General Mission Analysis Tool - NASA's open source software for satellite's orbit propagation.

Parameters	**Description**	**Units**
Starting date	25 Feb 2021 22:00:00	-
Drag coefficient	2.20	
Reflectivety coefficient	1.30	
Coordinate system	Earth centered inertial (J2000)	
State type	Keplerian	
Integrator	RK89	
Eccentricity	1.21×10^{-16}	
Semi-major axis	6771.00	km
Inclination	98.00	deg
Right Ascension of the Ascending Node	295.00	
Argument of Perigee	0.00	
True Anomaly	1.48×10^{-6}	
Minimum GS elevation visibility	10.00	

Table 2.4: Orbital parameters for 400 km altitude propagation of the spacecraft in GMAT

on the QBER and key rate for the chosen protocol. A Low Earth Orbit (LEO) has been specified to reduce the optical pathway between S/C and GS increasing the performance of the signal. For minimum altitudes of 400, 500, 600 and 750 km above ground the performance was tested and the satellite was propagated during 7 days as seen in Fig 2.3 and Fig 2.4 for 400 km. The parameters chosen for the orbit simulation can be seen in Table 2.4.

At these altitudes, drag is the main source of error for S/C pointing accuracy. Only with an accurate enough pointing acquisition at ground and stabilization in the optical apparatus the key exchange is possible. Another source of error is centered on the integrator chosen for the propagation as we will study in the next section.

Integration methods

GMAT uses an Earth centered propagator with a 4x4 gravity model which disturbs the trajectory of the orbit, for each S/C time-step we must then solve the initial-value problem which requires a precise integrator. Among all types of single step propagators as seen below, RK89 is chosen due to high accuracy that it provides.

1. Runge-Kutta ninth order with eighth order error control (RK89).
2. Runge-Kutta Dormand-Prince, eighth order with seven order control (RK-DP78).
3. Runge-Kutta Dormand-Prince, eighth order with fifth order error control with third order correction (RK-DP853).
4. Runge-Kutta, fifth order with fourth order error control (RK45).
5. Runge-Kutta, fourth order (RK4).

Runge-Kutta methods

A family of these integrators are defined by their type and order of error control, leading to a set of coefficients. Despite of choosing RK89, all other type of integrators will be also compared in order to extract the systematic errors from the satellite propagation. A general formula for the explicit Runge Kutta method can be expressed as follows:

$$y_{n+1} = y_n + h\sum_{i}^{s} b_i k_i \tag{2.1}$$

$$k_i = f(t_n + c_i h, y_n + h\sum_{j}^{i-1} a_{ij} k_j) \tag{2.2}$$

The parameters a_{ij}, b_i and ci are dependent on the choice of the method, s defines its order. The coefficients used for RK89 are taken from J. Verner [43] work, different sets were proposed where the chosen one may infer a source of error for the numerical integration due to the robustness of the parameters specific for the mission.

Propagator errors

By propagating the spacecraft for long periods of time, the integrator method originates a systematic error. Those errors may cause a deviation in the position of the spacecraft resulting in a divergence of the key rate and QBER for each elevation above the GS.

A methodology is proposed to find the systematic error. For a period of 30 days and a time-step of 10s the satellite is propagated where the Mean Error (ME) between the method of choice RK89 and all other integration methods is performed for the same orbital parameters. The systematic error is taken between the two most accurate integration methods during the quantum key exchange. The performance is evaluated depending on the position and velocity parameters along $\hat{i_1}, \hat{i_2}, \hat{i_3}$ axis in the Earth centered equator inertial frame of reference [44]. In Table 2.5 the maximum mean errors are provided after a simulation of the spacecraft for 30 days. Every 1 in 1000 points are chosen to be plotted where all of the results of position and velocity for every integrator are presented in Appendix.A.

By comparing RK-DP78 and RK89 the systematic error of the propagator used in the simulation is up to an order of 10^{-5} km, which becomes negligible in contrast to the order of magnitude for the optical path between S/C to GS $\in [10^2, 10^3]$ km. The same analysis is performed for ME of the S/C velocity, which is negligible compared to the mean velocity of the spacecraft in LEO orbit of $\sim$ 7.5 km/s.

Parameter	RK4	RK-DP45	RK-DP78	RK-DP853	Units
$\|E_1\|$	2.3×10^{-1}	6.11×10^{-4}	4.35×10^{-5}	2.22×10^{-3}	km
$\|E_2\|$	1.14×10^{-1}	2.98×10^{-4}	4.73×10^{-5}	1.08×10^{-3}	
$\|E_3\|$	2.53×10^{-1}	6.67×10^{-4}	6.28×10^{-5}	2.42×10^{-3}	
$\|E_{v1}\|$	2.69×10^{-4}	6.85×10^{-7}	5.00×10^{-8}	2.48×10^{-6}	km/s
$\|E_{v2}\|$	1.32×10^{-4}	3.39×10^{-7}	5.35×10^{-8}	1.23×10^{-6}	
$\|E_{v3}\|$	2.92×10^{-4}	7.55×10^{-7}	7.11×10^{-8}	2.74×10^{-6}	

Table 2.5: Absolute mean error between RK89 and the a chosen integrator used for orbit propagation.

Orbit end-of-life

One important factor for defining the orbit is its own end of life cycle. The requirement CR-02 from Table 2.1, creates a restriction on the altitude of S/C. Additionally, this parameter tell us about the resources needed for the active removal of the satellite upon the end of mission.

To have this study we use DRAMA [45], an open source ESA software for space debris mitigation. More specifically, we focus on the OSCAR tool [46], which provides an endorsing accordingly to the space debris mitigation guidelines for the end of life cycle of an orbit. OSCAR allows to use Monte-Carlo with generated data of solar flux and geomagnetic activity on the satellite's trajectory deviating it. The software used meets the ISO 27852:2011 (Space Systems - Estimation of orbit lifetime) standards [47].

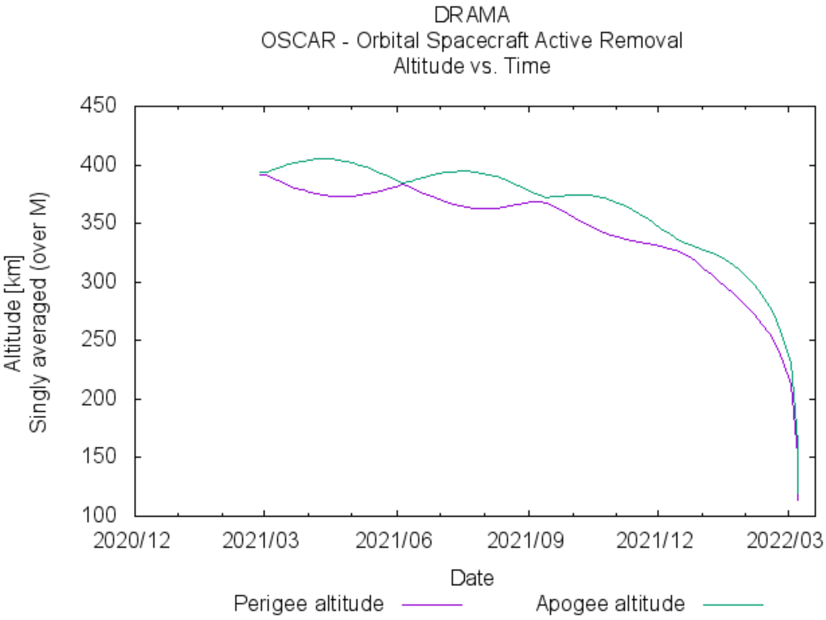

Figure 2.5: Altitude above ground of S/C in terms of time for 400 km.

The simulations were performed with the same orbital parameters as in the Table 2.4. The altitude, eccentricity, inclination and solar activity in terms of time was calculated. The results are shown in Appendix.B.

It is estimated that for 400 km in altitude the orbit reaches a life time of one year as seen in Fig 2.5. Therefore, the orbit becomes not viable considering the requirement for the mission to have a life-time of at least three years.

For 500 and 600 km in altitude the simulations show respectively 4 years and 20 years for the end-life cycle of the orbit. However, due to the hardware endurance and malfunctions the mission may never reach those estimations but it allows us to know if an active removal of the satellite is needed.

With the trajectory of the satellite and optical path defined, in the next chapter we provide a geometrical estimation on the performance of the space mission for different QKD protocols to finally analyze and optimize the geometrically dependent parameters from Tables 2.2 and 2.3.

3

Geometric losses

3.1 BB84

The objective of this section is to obtain the key rate and QBER for the altitudes of 400, 500, 600 and 750 km. Also the geometrical parameters presented in Tables 2.2 and 2.3 from the previous chapter are studied in depth.

In the geometrical analysis the BB84 polarization encoded protocol is used. The E91 and phase-dependent protocols in this analysis give similar results geometrically. They will be analysed when in chapter 4 and chapter 5 the background interaction and atmospheric attenuation are introduced, differing considerably from the results of this approach.

As for the methodology, we consider time dependent distances of the satellite simulated by GMAT from the previous section. We then derive the elevation of the satellite in terms of the active time where the key distribution can be performed. For this section we will focus on a decoy state BB84 protocol. First of all, the size of the key is defined. The information is then send from the S/C to GS and every bit is encoded with a basis vector. Furthermore, the basis are decoded and compared, sifting the whole key.

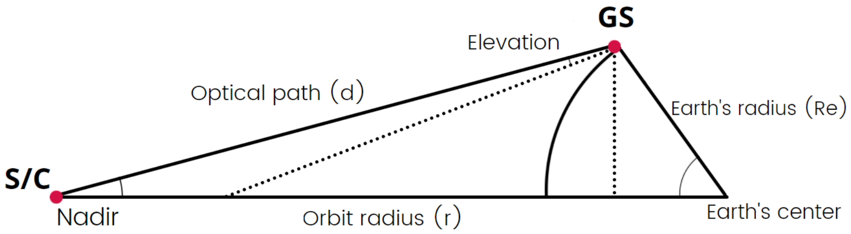

Figure 3.1: Trigonometric relation with cosine law to find elevation (ϵ).

S/C elevation

For this section we explain the conversion between the dataset provided from GMAT in J2000 Earth centered coordinate system to a GS based coordinate system.

The dataset provides the distance from the Earth's center to the GS and to the S/C. In order to have a ground station based coordinate system we must redefine all distances into elevation above horizon. Accordingly, we must use the law of cosines for this conversion as seen in the following equation [48]:

$$r^2 = R_E^2 + d^2 - 2R_E d cos(90 + \epsilon) \tag{3.1}$$

All parameters can be seen in Fig 3.1. The optical path (d) between the S/C and GS is present. The Earth's radius (R_e) is considered as well as Nadir from the S/C view.

The results of all distances and elevations (ϵ) for each altitude can be seen in Fig 3.3 and 3.2 respectively. An uncertainty arises from the choice of Right Ascension of the Ascending Node (RAAN) in order to maximize the elevation for different altitudes. This uncertainty is calculated by comparing the obtained results with the estimated ones when $\epsilon = 90$ deg. Let me emphasise that this error has only been considered in the simulation domain, being totally different from an experimental setup. In a experimental setup for optical communications the uncertainty can be much lower with the introduction of Global Navigation Satellite System (GNSS) [49], tracking and GS beacon systems which decrease the uncertainty down to an order of 10^{-3} s to 10^{-5} s. As a result, as seen in Fig 3.3, we obtain the S/C minimal optical paths of 400 ± 0.11 km, 500 ± 2.95 km, 600 ± 1.20 km and 750 ± 0.34 km respectively.

Optical gain

For this section a estimation of the optical gain for 400, 500, 600 and 750 km is provided as well as a study and justification of the geometrical parameters from chapter 2.

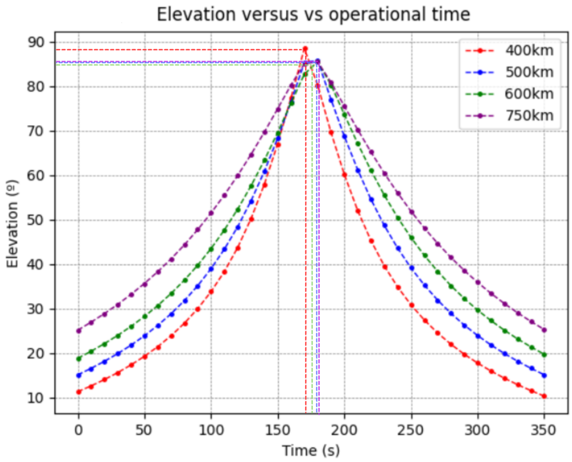

Figure 3.2: Elevation above horizon at GS for 400, 500, 600 and 750 km. The centroid and maximum elevation is presented for each orbit.

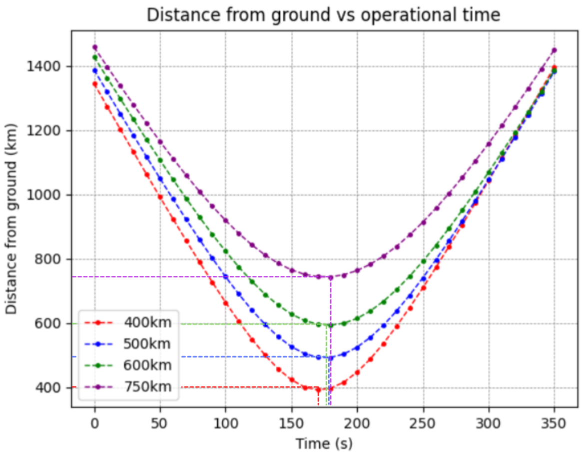

Figure 3.3: Optical path from S/C to GS for 400, 500, 600 and 750 km. The centroid and minimum distance is presented for each orbit.

With the elevation calculated we can start to propagate a Gaussian beam along time. A non-truncated Gaussian beam model with paraxial approximation is considered. Truncation pays an essential role [50] in most of the realist optical devices, leading to deviations in the intensity profile viewed at GS. Therefore, instead of having a Gaussian profile, in a more realistic scenario it is more proper to consider an eliptical [28] model.

In the simulator only from chapter 6 this effect is taken into consideration, characterizing in a more realistic way the intensity profile. For now we will stick to our usual Gaussian profile. In order to have a estimation of the main geometrical parameters we use the following equation [51] representing the Gaussian optical loss (dB):

$$\frac{P_R}{P_T} = 20log\left(\frac{D_R D_T}{D_T^2 + 2.44mL\lambda}\right) \tag{3.2}$$

P_T and P_R are the laser power transmitted from the satellite and received at GS respectively. L is the optical link distance between GS and S/C, λ is the wavelength at which the source operates, D_T and D_R are the diameter of the transmitter and receiver respectively. Combining the Equation 3.2 with the elevation dataset it is now possible to estimate the optical geometric loss for each orbit as seen in Fig 3.4.

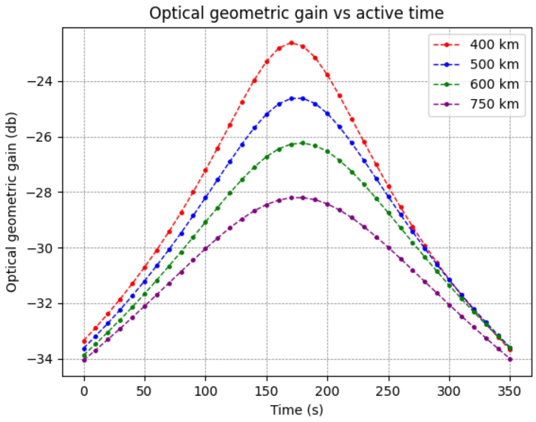

Figure 3.4: Optical loss for 400, 500, 600 and 750 km in altitude.

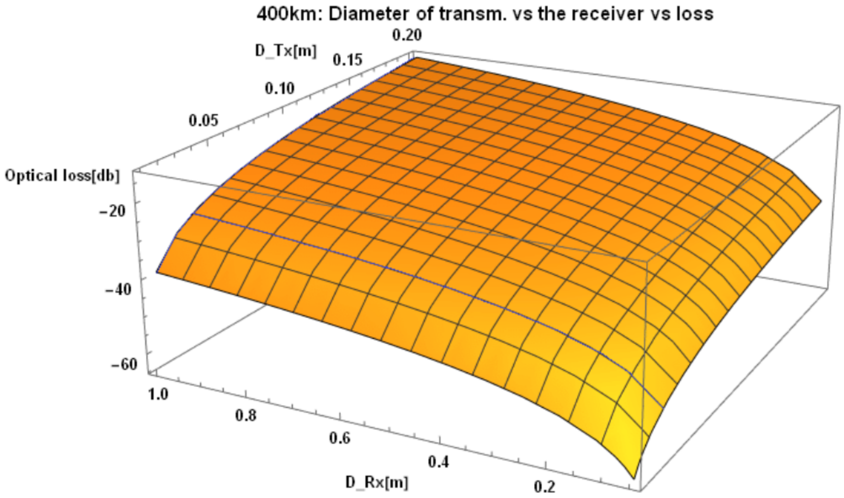

Figure 3.5: Geometrical loss analysis in terms of D_T and D_R.

In Fig 3.5 a representation of Equation 3.2 can be seen for 400 km, allowing to minimize each of the three main geometrical parameters D_T, D_R and $\frac{P_R}{P_T}$. We have considered typical diameters of the telescope apertures at the ground station for optical communications as well the 2U Cubesat size constrains for the mission (CR-03 from Table 2.1). Thus, obtaining $D_R = 2.0$ m and $D_T = 0.03$ m as seen in Tables 2.3 and 2.2 from the previous chapter.

Sifted key rate and QBER

In this section we estimate the key rate and QBER for different altitudes. A justification and analysis on the choice of the most efficient altitude is also provided allowing to conclusively set all the geometrical parameters.

In order to calculate the key rate that we would obtain at GS, we should first estimate the number of photons sent by the SPS with a step of $\Delta t = 10$ s between each key exchange. Afterwards, the expected number of photons is calculated from the expected power received at GS as seen from the following equations [52]:

$$P(d, D_R) = P_0(1 - e^{\frac{-D_R^2}{2w_d^2}}) \tag{3.3}$$

$$Q = \eta_q \eta_{opt} \Delta t \frac{P(d, D_R)}{E_\gamma} \tag{3.4}$$

$P(d, r_0)$ is the expected power received at GS. The Gaussian spot size (w_d) is also provided in terms of optical path (d). As stated in Table 2.3 in chapter 2, η_q and η_{opt} are the quantum and optical

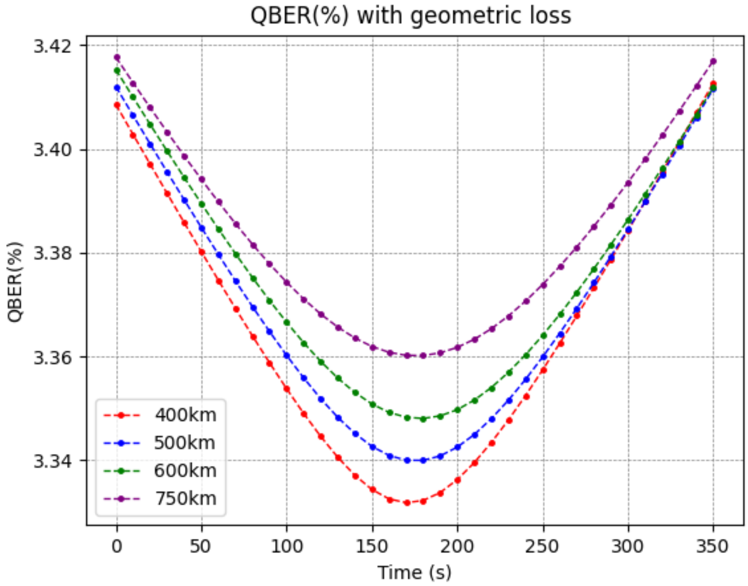

Figure 3.6: QBER for 400, 500, 600 and 750 km in altitude. Considering only the geometric loss, all the results for BB84 protocol are below the limit of 11%.

efficiencies respectively. Q is the expected photon fraction recieved at GS.

3.1.1 QBER

From the loss function stated in Equation 3.4 we can obtain via a comparison between the basis of the encoded information the respective QBER. Using Equation 3.5 [27] we can obtain the QBER for altitudes of 400, 500, 600 and 750 km only considering for now the geometric loss.

$$QBER = \frac{\frac{Y_0}{2} + e_{det}(1 - e^{-\eta L(\theta)\mu(\theta)})}{\frac{Y_0}{2} + 1 - e^{-\eta L(\theta)\mu(\theta)}} \tag{3.5}$$

As stated in chapter 2 in Table 2.3, Y_0 and e_{det} are the dark count probability and the basis misalignment respectively. L is the optical path which is dependent on elevation (θ), η contains the optical and quantum efficiencies. Finally, $\mu(\theta)$ is the generalized loss function which is also geometrically dependent on elevation.

From this results we obtain in Fig 3.6 the QBER for different altitudes. As seen, above the grey margin of 11% the BB84 protocol becomes not suitable due to high error between the transmitter and the receiver. Thus, allowing for an attacker (Eve) to easily penetrate into the protocol and retain information. Due to this margin, the active time shortens with the increase of the S/C altitude. The active time of the mission not only plays an essential role to determine the optimal S/C altitude but also to successfully

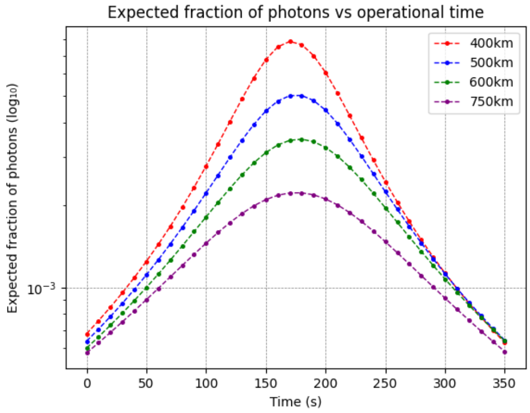

Figure 3.7: Expected photon ratio for 400, 500, 600 and 750km in altitude.

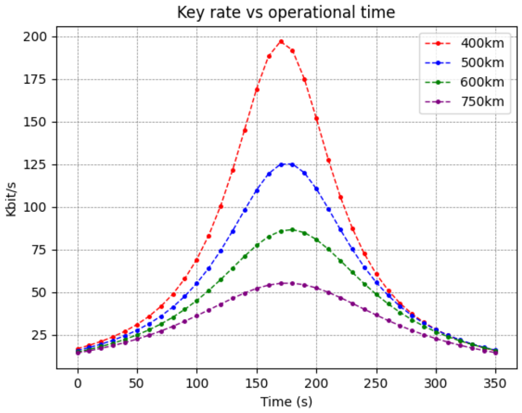

Figure 3.8: Sifted key rate for 400, 500, 600 and 750 km in altitude.

perform QKD influencing directly on the requirement CR-01 from Table 2.1. For 400, 500, 600 and 750 km by introducing the geometrical term the BB84 does not lose validity (QBER $< 11\%$). Thus, obtaining respectively for each altitude at zenith QBER $= 3.33\%, 3.34\%, 3.35\%, 3.38\%$ for 400, 500, 600 and 750 km orbits. The uncertainty was calculated from shifts in trajectory as was observed in Fig 3.2 for the different altitudes of S/C.

3.1.2 Sifted Key rate

From Equation 3.4 the sifted key rate (K) can be also calculated by comparing the Alice's and Bob's basis $(\delta_{A_i}^{B_i})$ as seen in Equation 3.6. An added Gaussian white noise with standard deviation of $\sigma = 0.1$ was considered to account for systematic errors caused by thermal and hardware oscillations. The multiplicative behaviour of white noise comes from its dependence on the state of the receiver for each time step, hence, influencing on the sifted key rate [53].

$$K = \frac{\sum_i^{n_t} \delta_{A_i}^{B_i} e^{-\frac{x_i^2}{2\sigma^2}}}{\sigma n_t \sqrt{2\pi}} Q(P(d, D_R)) \tag{3.6}$$

Thence, in Fig 3.7 we obtain the expected photon fraction at GS. The photon fraction provides us with the ratio of received photons for each single photon sent from the S/C. In Fig 3.8 the measured sifted key rate is also present for different altitudes. As seen, when the satellite is nearest there is an increase in performance by a ratio of 1.594 ± 0.006 between the 500 km and 400 km orbit. If instead the same analysis was performed between the 600 km and 400 km orbit, we would increase the signal's performance by a ratio of 2.318 ± 0.003. For the 750 km orbit the performance increase reaches up to a ratio of 3.643 ± 0.001 compared to the 400 km orbit.

Looking at the results from Fig 3.8 we understand that a change in altitude keeps the key exchange performance within the same order of magnitude. Thus, we need to evaluate the choice of the orbit's altitude by additionally taking into consideration the mission's active time and the drag coefficient which is dominant at LEO.

Atmospheric and radiative drag originate perturbations in the satellite trajectory as well as oscillations in optical payload. Even with high precision accelerometers [54] the oscillatory behaviour is present generating a pointing offset of the signal at the GS.

We can estimate the drag force at different altitudes by considering that the spacecraft deceleration due to atmospheric drag is described by: $a_{drag} = \frac{1}{2}\rho|v^2|C_D\frac{S}{m}$ [55]. Here ρ is the atmospheric drag coefficient, v is the relative velocity between the atmospheric layer and the spacecraft, C_D is the drag coefficient, S is the reference surface area and m the mass of the body. Considering the JB2006 model [55], the ratio of $\Delta\rho$ can be estimated between altitudes 750 km and 400 km for low, medium and high intensity solar and geomagnetic activities. We obtain a ratio of $\Delta\rho = 10^3$ in the total atmospheric density profile, there a total deceleration of the spacecraft is of the same order of magnitude. Therefore, the oscillatory behaviour is greatly attenuated by three orders of magnitude by changing from a 400 km to a 750 km orbit.

Considering all dominant variables for the choice of the orbit, we believe that the latter one is dominant, hence choosing the 750 km orbit. On one hand the key rate on that altitude does not drop considerably on the other the active time of the mission maintains the same to perform successfully QKD. With this choice the mission compensates with added optical accuracy by minimizing the atmospheric drag effects by three orders of magnitude. Obtaining a viable sifted key rate of an order of 10^1 kbit/s even at a high altitude.

4

Background losses

Introduction

One of the greatest beauties and tragedies of science is that *the universe does not allow perfection* to coexist [1]. Every measurement comes with noise perturbations, irregular oscillatory behaviour and uncertainty. To crumble the figment of reality responsible for the ideal environment present in our mission concept, we shall perform a background analysis.

Thusly, in this section we propose a method to calculate the natural and artificial background, influencing the results at GS by adding a layer of complexity to the simulator. To specify further, we

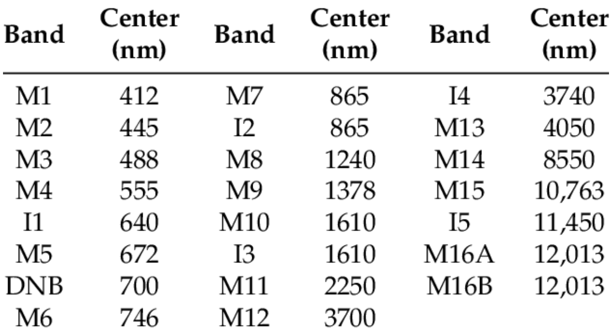

Band	Center (nm)	Band	Center (nm)	Band	Center (nm)
M1	412	M7	865	I4	3740
M2	445	I2	865	M13	4050
M3	488	M8	1240	M14	8550
M4	555	M9	1378	M15	10,763
I1	640	M10	1610	I5	11,450
M5	672	I3	1610	M16A	12,013
DNB	700	M11	2250	M16B	12,013
M6	746	M12	3700		

Figure 4.1: VIIRS filter bands with the corresponding wavelength centers. Image taken from [6].

---

[1] From Stephen Hawking, A Brief History of Time.

consider natural background as a combination of the emission lines at upper atmosphere, airglow, scattered moonlight, scattered starlight and zodiac light [7]. Considering the requirement CR-05 from table 2.1, we perform the simulations at night for low moon brightness.

We will use the VIIRS [2] open source data which provides satellite imagery of Earth in different ranges of wavelength along time. This analysis will be centered on the Alqueva region after 23:00 (GMT+1) as was stated by the requirements CR-04 and CR-05 from Table 2.1. Specifically, the Signal to Noise Ratio (SNR) will be of study. Afterwards, some background filtering processes will be introduced as well as their applicability to our results. In the final section we present briefly the importance of background polarization.

4.1 Background estimation

Astronomical observations choose their environment strategically in order to diminish the perturbations on the intensity profile of the object in study [56]. We shall apply the same method for optical communications.

At first we consider a ground site in the Alqueva region with latitude and longitude defined in Table 2.3. From that we use the NASA's open source VIIRS data centered at that location along time. This data has been provided from the S-NPP satellite mission which was first launched in October of 2011. VIIRS was one of the main set of sensors that constitute the payload of the mission as seen in Fig 4.1 [6]. The spatial resolution of the telescope may vary from 0.5 to 1 km.

This data can supply us with the local surface spectral reflectance, albedo, vegetation density, ice density as well as the local artificial brightness. This is done by combining different filters with diverse wavelength bands. In Fig 4.2 we show an example where by treating the provided data for M3, M10 and M11 filters we increase the contrast for snow, ice and clouds identification in the south region of Portugal. This is only possible due to high reflectance of ice at those wavelength ranges [57].

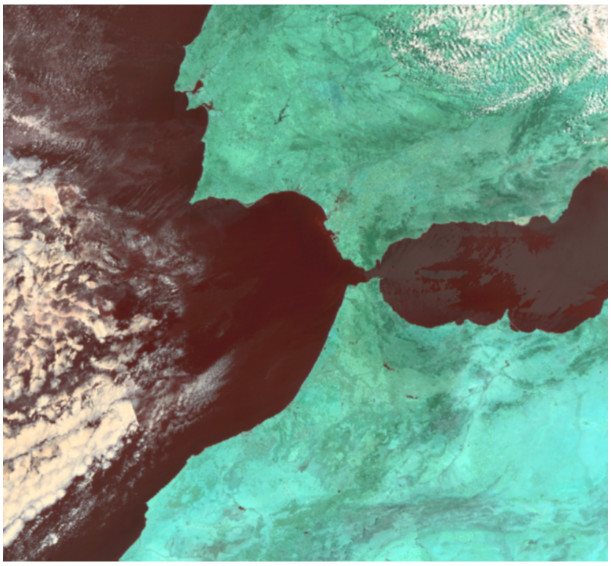

Figure 4.2: Treated image of the south region of Portugal taken with a satellite pass-by at 15:13:15, 25th of February 2021. M3, M10 and M11 band filters were used.

---

[2] Visible Infrared Imaging Radiometer Suite (VIIRS) is an open source product from NASA's/NOAA's SUOMI-NPP and NOAA-20 satellite missions.

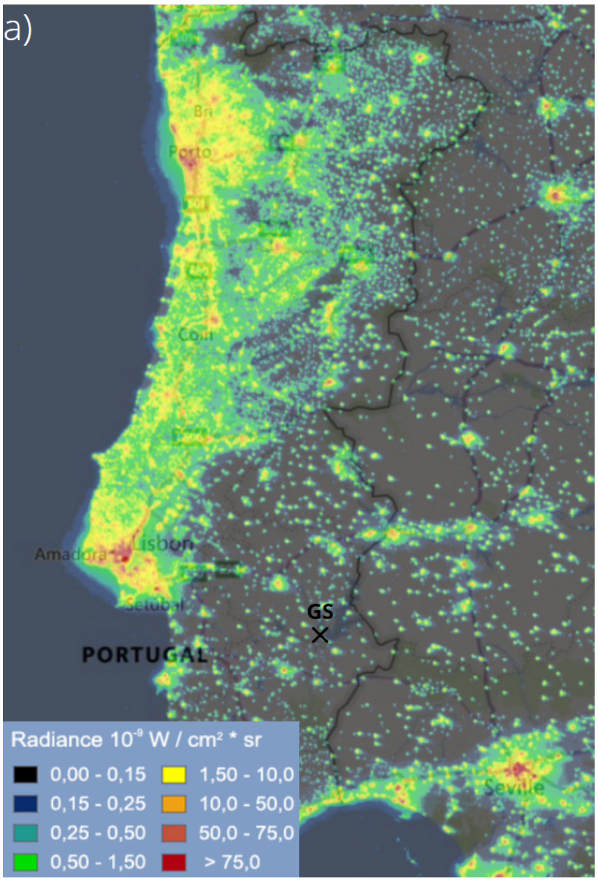

Figure 4.3: VIIRS data for the radiance profile for the region of Portugal. GS location has been indicated in the image obtaining radiance levels of 0.13×10^{-6} W/cm^{2}sr.

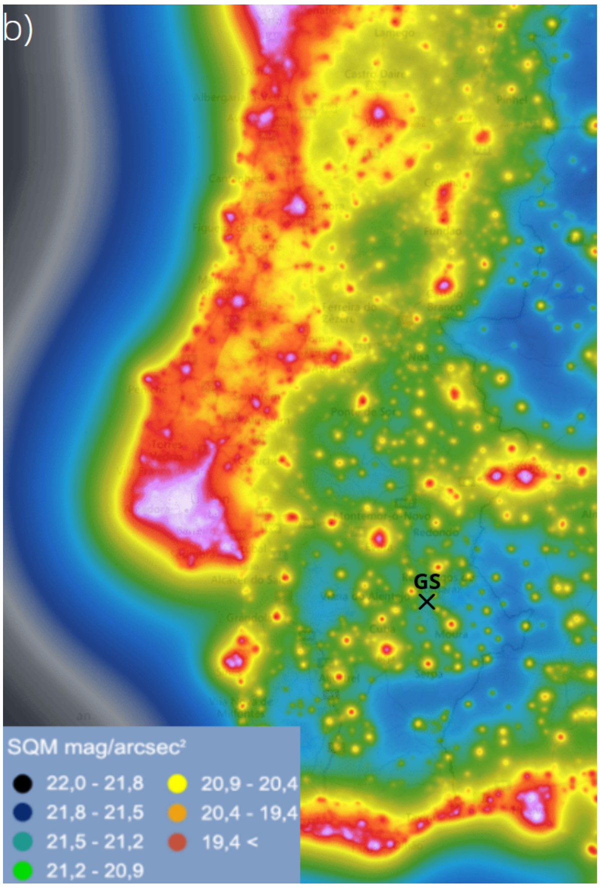

Figure 4.4: ATLAS 2015 data of the Quality Meter (SQM) profile of Portugal. SQM magnitudes of 21.35 ± 0.15 mag/arcsec^2 were obtained for GS. Image taken from [7].

However, for this work, from all the detectors present in Fig 4.1 we shall focus on the Day and Night Band (DNB). This filter band has sensitivity within the Infrared Range (IR) range of $\lambda \in [500, 900]$ nm [7] which contains the operational wavelength for our mission $\lambda = 850 \pm 1$ nm. This band compared to others is specially useful during night time observations which becomes practical considering the requirement CR-05 from Table 2.1 for our mission. Therefore, it allows to provide with the surface's radiation levels from all the artificial light sources situated nearby the GS as seen in Fig 4.3.

The data provided from VIIRS detector is obtained from the reference frame of the S-NPP satellite. Yet, if we want to look at zenith from the GS and gain information on the total artificial brightness we would need to modify that data to account for the scattering effect of light in the atmosphere. This conversion is performed with the ATLAS 2015 data-set as seen from the work of Fabio Falchi et al. [7] represented in Fig 4.4. As seen, considering the location of GS we obtain the total brightness at zenith of $B_{Total} = 0.000222 \pm 0.000011$ cdm^{-2}. For the natural mean sky brightness in the chosen region we have obtained values of $B_{Natural} = 0.000051 \pm 0.000005$ cdm^{-2}. The uncertainty is given based on the

SQM color scale range ± 0.15 mag/arcsec^2.

From those results we now pretend to calculate the number of photons based on the artificial and natural brightness at zenith. For that use Equation 4.1 [24], with an added term which considers the quantum efficiency (q_{eff}) of our telescope:

$$N_{tot} = \frac{1}{E_\lambda}\{(H_{nat} + H_{art}) \times \pi(FoV)^2 \times q_{eff} \times \frac{\pi}{4}D_R^2\} \tag{4.1}$$

N_{tot} is the background number of counts and D_R is the diameter of the telescope. H_{nat} and H_{art} are the natural and artificial night sky brightness respectively. FoV is the Field of view of the GS and E_λ is the energy of each photon with wavelength λ.

Despite of obtaining the background number of counts at zenith, the satellite moves along different elevations in the active time which was not yet considered in this model. In order to do so we must apply the van Rhijn effect [58]. This phenomenon states that the line of sight of the airglow layer lengthens with increase of the zenith angle. Being it mostly dependent on the Rayleigh airmass density for each elevation as seen in Equation 4.2 [8]:

$$X = \frac{1}{sin\{h + 244/(165 + 47h^{1.1})\}} \tag{4.2}$$

Here h is the apparent altitude defined as $h = 90 - z$ where z is the zenith angle. Finally we can obtain the expected change in the sky brightness along elevation as seen in Equation 4.3 [59]:

$$\Delta m = -2.5log\{(1 - f) + fX\} + K(X - 1) \tag{4.3}$$

$K = 0.032$ is the extinction coefficient for IR-band of $\lambda = 850.0 \pm 1.0$ nm [60]. Here $f = 0.6$, f is the fraction of sky brightness generated by airglow [61]. Here, Δm is the expected change in apparent magnitude along the elevation. Using Equation 4.3 we obtain the background counts per second during the active time of the key exchange as seen in Fig 4.5. Fig 4.6 represents the fraction of received photons at GS, defined as $S_F = \frac{Signal}{Background+Signal} \times 100\%$.

As seen in Fig 4.5 and Fig 4.6 the background is within a range of $B \in [3.0 \times 10^4, 5.3 \times 10^4]$ cps leading to a $S_F \in [36.1, 79.8]\%$. However, the previous values consider low moon brightness.

For different moon phases, the minimum background counts per second can increase up to an order of magnitude when the sky is totally moon lit [7].

In order to validate the obtained results we shall compare them with experimental results of the night

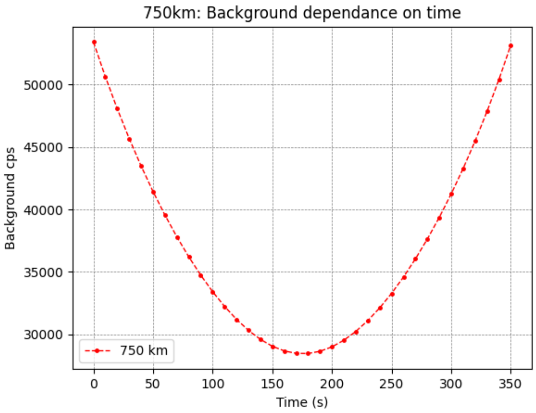

Figure 4.5: Background counts per second received at GS during active time.

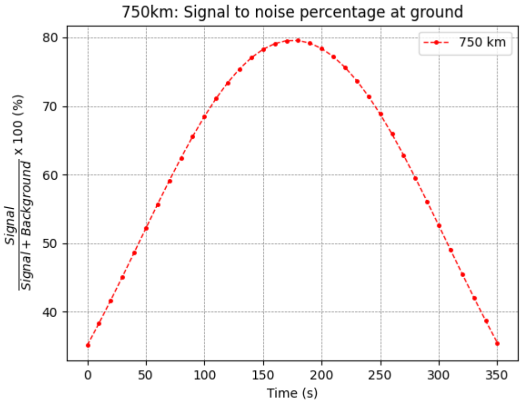

Figure 4.6: Fraction of signal received at GS during active time. At zenith, 79.8% of the received photons come from the S/C.

sky brightness at the ESO-Paranal ground site [8].

We also compare our results with the SkyCalc[3] simulator for the sky brightness which considers the Cerro Paranal Sky Model [58, 62]. The ESO-Paranal ground-site is located at a 2.635 km altitude, where the extinction coefficient (K) for IR-band was obtained with a 8.2m low dispersion spectograph with a 92.7% of filter usage.

Comparing to both methods in the IR band, our work obtains the same order of magnitude for the brightness calculations at zenith. For different elevations, we have compared experimental data from the ESO-Paranal ground site achieving a similar Δm profile [8] as seen in Fig 4.7.

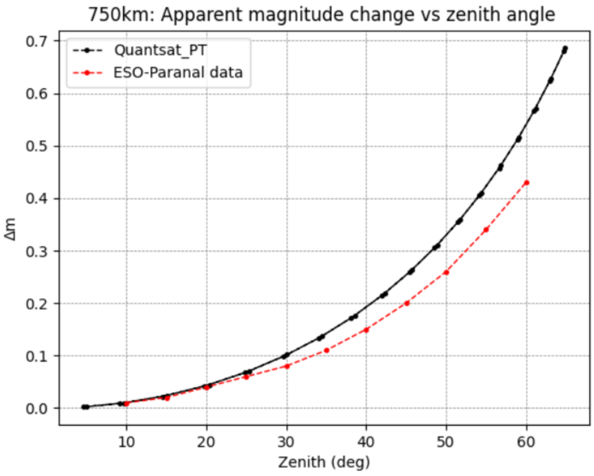

Figure 4.7: Apparent magnitude change of the night sky brightness for IR band at different zenith angles. ESO-Paranal data obtained from [8].

With the background profile defined for 750km in altitude, in the next section we shall analyse the use of filtering techniques to decrease the background influence and optimize the SNR.

---

[3] SkyCalc is an open source software which allows to simulate at a certain bandwidth the natural background at the ESO-Cerro Paranal ground site

4.2 Techniques for background filtering

A question for the reader: Can there be any way to distinguish between all the noise we obtain at our Single Photon Detector (SPD) and our signal?

Despite of the title of this section, the answer is actually tricky. Because yes, we can filter trough our background but we cannot exactly distinguish it.

Lets start from the beginning, from all the photons that we obtain, we can apply wavelength filtering (which was applied in our previous results). Wavelength filtering [63], chooses a band range for which only at those wavelengths photons may be detected by the SPD, in our case, it goes up to a range of ± 1 nm. State of the art filters achieve an even lower range of ± 0.01 nm by introducing hybrid quantum photonic circuits [64]. However, with added precision we must also consider the S/C velocity with respect to GS due to the existence of the Doppler shift effect on the signal [65]. Considering that the Doppler effect can be represented by $\lambda_{GS} = \lambda_{S/C} \frac{v_\gamma}{v_\gamma - v_{S/C}}$ [66], where λ_{GS} and $\lambda_{S/C}$ are received and sent wavelength consecutively. $v_\gamma = 0.9734 v_{vacuum} + 0.0267 v_{atmos}$ is the speed velocity of light in different media. For 750 km about 97.34% of the optical path is considered as vacuum and the other fraction is the atmosphere (most dense layers reach up to 20 km in altitude). From GMAT a mean velocity of 7.8 km/s for the S/C is achieved. Considering $\lambda = 850 \pm 1$ nm we obtain a Doppler shift of ± 0.02213 nm. As the filtering precision reaches up to ± 0.01 nm it means that compensation is needed as well as an accurate measurement of the S/C acceleration in order to not lose precision in the photon filtering at the GS.

Now the other parameter which is useful for background filtering is the time step between two consecutive photons sent by S/C [63]. We may apply time-gate filtering which deactivates the SPD only narrowing an opening when an expected photon responsible for the signal is about to reach the telescope.

However, three main problems may arise if this approach is considered:

1. **Precision of the gate opening [67]**: On one hand if temporal resolutions are too high, we may miss the photon responsible for the signal. On the other if they are too low we allow for an high background interference on our results. This effect is highly dependent on the used detector for the mission. Based on the state of the art detectors this limit reaches < 2.5 ns for high temporal resolutions and ≥ 7.5 ns for low temporal resolutions, respectively [67].

2. **Type of SPD chosen [68]**: Most commonly (and in our mission) a single photon avalanche diode is chosen to detect each photon. However, an inherent disadvantage of such detectors is the dead time after the trigger [69]. Meaning, that such detectors cannot be used in strong background environments which as a result highly interfere with the signal. A more novel solution suggest the use of superconducting nanowire single-photon detectors (SNSPD). With added disadvantage of

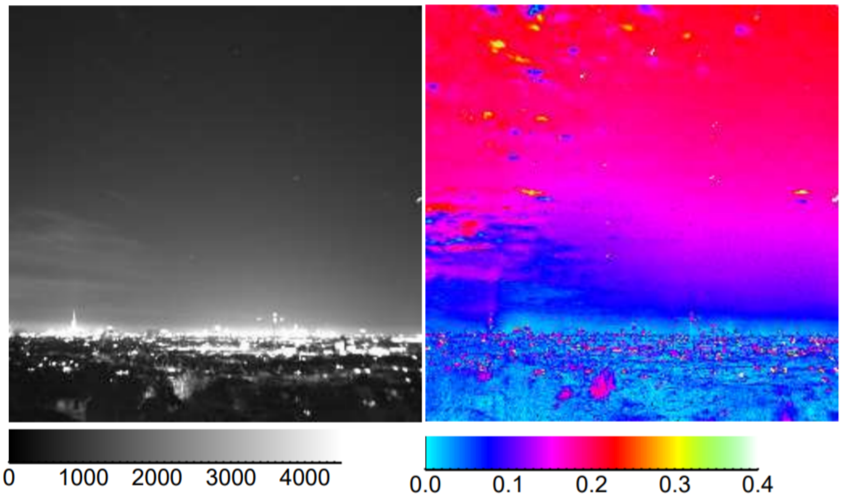

Figure 4.8: a) Normalized Stokes parameter S_0 of the night sky taken in January of 2011 in the Berlin, Germany. Darkest pixel has value ~ 550. **b)** Normalized DoP $\in [0.0, 1.0]$ of the night sky for the same image. Images with experimental data taken from [9].

additional cooling and cost, such detectors can enable high-rate QKD (1.3 GBit/s) outperforming any available SPD [68]. They can exhibit a jitter in the range of tens of ps, an almost 90$\%$ quantum efficiency, and extremely low dark count rates on the order of 10^{-4} Hz [70, 71].

3. **Synchronization [63]**: In order to know exactly the time step between two photons, the satellite to ground QKD must be assisted with the Acquisition, Tracking and Pointing (ATP). The beacon light for such as system should have an added purpose of QKD synchronization.

Background Polarizability

As BB84 and E91 protocols can be polarization encoded, it is essential to account how polarized background influences our results.

According to requirement CR-05 from Table 2.1 the mission is performed during the night time. In the presence of moon lit sky, the weakly polarized skyglow can be dominated by the moon's Rayleigh scattering [72]. As most of the moon's light is depolarized, the angle of the moon with respect to the atmospheric layer allows for Rayleigh scattering to occur, thus, polarizing the moonlight. Fig 4.8 represents experimental data acquired with the luminous filter representing the DoP of night sky taken in January of 2011 in the Berlin, Germany [9]. From this work we can see that the photon DoP can increase up to 40% at 10 deg of Moon's elevation in the IR band. With respect to our work this can be quite relevant, where on one hand the moon lit sky increases its brightness up to two orders of magnitude for IR [73] depending on the moon phase. On the other, an added effect from background polarization introduces an increase of error for the signal measurements performed at GS.

Furthermore, due to the fact that most of artificial light is unpolarized [9], having the GS location situated in an urban environment would greatly attenuate the signal polarizability up to an unnoticeable point at the GS. This can be seen in Fig 4.8 on the right, where at the horizon the influence of the artificial environment is dominant, depolarizing the moonlight.

For the simulator we consider a low lit moon, meaning that background polarization due to Rayleigh scattering is negligible. The time gating filtering is considered by decreasing up to an order of magnitude the received background. These results follow the work of Timm Kupko et al. [68] where the anti-bunching improves up to the same order with a 2.5 ns time-gating filter.

In the next chapter, instead of studying the background polarization, we will focus on the signal depolarization due to turbulence. Creating an atmospheric and turbulent model which deteriorates and changes the S/C signal.

5

Atmospheric losses

5.1 Atmospheric model

In this chapter we shall answer the following questions: How can we simulate and define the Earth's atmosphere and what are its main parameters? How does the atmosphere influence the propagation of the optical signal? Moreover, how does it change the performance of the BB84 and E91 QKD protocols? Most of the state of the art simulators [2, 52] when they compare their results with the experimental data [2, 26], they justify their most dominant source of errors from the atmospheric disturbances on the signal. As a result, in this chapter we strongly incentivize a more detailed study on the atmospheric influence on laser communications. Going all the way from an in-depth analysis of the atmospheric attenuation to the degree of depolarization of the signal at different elevations of S/C.

Methodology

To construct the atmosphere we shall use an open source software called libradtran 2.0.4 [1] [74]. A Python 3.9.7 [2] code was created combining in parallel multiple subprocesses in Cygwin64 [3] which were used to compile and run all operations and data of our program. LibRadtran is a library of radiative transfer routines and programs which focuses mostly on a radiative transfer tool called uvspec. Uvspec main property is to calculate spectral irradiances, however, its uniqueness comes from the fact that it contains multiple different radiative tools which we can combine for our purposes [75]. Hence, allowing for more adaptable approach to study different effects of the atmosphere. We shall mainly focus on the following two:

1. **Disort** [76–78]: Solves the radiative transfer equation in 1D geometry performing accurate calculations of radiance, irradiance, and actinic flux with the downside of not considering a model for photon polarization. This code was used in section 5.2 of this chapter.
2. **Mystic** [75, 79, 80]: Uses Monte-Carlo to solve the polarized radiative transfer equation in 1D and 3D geometries. Mystic was developed to perform photon forward tracing, where individual photons are traced from their source to their random paths through the 1D or 3D geometry atmospheres. Mystic can also handle polarization-dependent scattering by randomly oriented particles. Thus, providing us with a viable solution for depolarization calculations. This code was used in section 5.3 of this chapter.

In our simulator, these previous two algorithms propagate photons in a plane-parallel geometry solving the monochromatic Radiative Transfer Equation (RTE) for each elevation of the S/C presented in Equation 5.1 [75]:

$$-\mu\frac{dI(z,\mu,\phi)}{\beta_{ext}dz} = I(z,\mu,\phi) - \frac{w(z)}{4\pi}\int_0^{2\pi} d\phi^{'} \int_{-1}^{1} p(z,\mu,\phi,\mu^{'},\phi^{'})I(z,\mu^{'},\phi^{'})d\mu^{'} - (1-w(z))B[T(z)] \tag{5.1}$$

From the Equation 5.1, the first term on the right comes from the radiative loss due to photon extinction (which considers photon absorption and scattering), where $I(z,\mu,\phi)$ is the specific photon intensity. The second term is the scattering term for all directions in a parallel plane, where w(z) is the single scattering albedo term. The third term gives the thermal radiation emitted in the frequency range of interest, there, $B[T(z)]$ is the Plank function integrated over the wavelength of $\lambda = 850 \pm 1$ nm. Here, $\mu = cos(\theta)$ where θ and ϕ are the polar and azimuth angles respectively. $p(z,\mu,\phi,\mu^{'},\phi^{'})$ is the phase

---

[1] Documentation for the 2.0.4 version is available.

[2] Documentation for the 3.9.7 version is available.

[3] A large collection of GNU and Open Source tools which provide functionality similar to a Linux distribution on Windows.

function shift due to scattering, dependant on the molecule density and scattering cross section. β_{ext} is the extinction coefficient, composed of the sum of scattering and absorption coefficients which depend on the density of the atmospheric molecule species and the scattering and absorption cross section, respectively. Assuming a flat earth approximation, the atmosphere is defined in infinite x and y layers, reducing the photon position to altitude z.

For the simulations we consider the S/C photon source with parameters defined in Table 2.2. The S/C elevation data from chapter 3 has been also used for this section to plot the atmospheric transmissivities at different altitudes.

5.2 Atmospheric simulation

Before we move a step further, we must first evaluate the following parameters present in Table 5.1 for the Disort simulation. Based on surface albedo data from the Suomi-NPP satellite [4] [81] in a rural environment we shall consider an albedo ratio of 0.20 for the Earth's surface. The azimuth angle for both, the transmitter and receiver was considered the same. We have considered a mid latitude summer atmosphere file type as an input. The respective file contains parameters responsible for the temperature, pressure, air density as well as the O_3, O_2, H_2O, NO_2 concentrations along different altitudes for the atmospheric layers [82].

Another set of input parameters present in Table 5.1 are the aerosol ones. We examine a rural aerosol environment based on the OPAC dataset [83] which provides with the concentration of soil particles, sea salt mixtures, desert dust particles and sulfate droplets with a 75% concentration of H_2SO_4 [84]. The aerosol visibility was defined accordingly to experimental data in the same rural environment [85], reaching up to 23.0 km from the GS.

A REPTRAN [86] file is also provided which performs a band parametrization at the top of the atmosphere with a fine bandwidth resolution of 1.0 $cm^{-1}bin$ [75]. The final input to be considered is the statistical cloud data. This data was generated based on cloud parametrization which converts parameters such the effective droplet radius and optical cloud thickness propagated at different altitudes to optical parameters. For radiative calculations Mie theory was used [87] within the libradtran Mie tool [74]. To generate the optical properties from the cloud statistics a gamma distribution was assumed for the cloud droplets: $n(r) = Nr^{\alpha}exp(\frac{r}{r_{eff}v_{eff}})$ where $\alpha = \frac{1}{v_{eff}} - 3$. Here r_{eff} is the effective droplet radius, $v_{eff} = 0.1$ is the effective variance, N is a normalization constant [74].

All files used in our simulation are available for free in the public domain and can be found in section 5 at the following libradtran repository.

---

[4] Suomi-NPP Albedo Product Details available

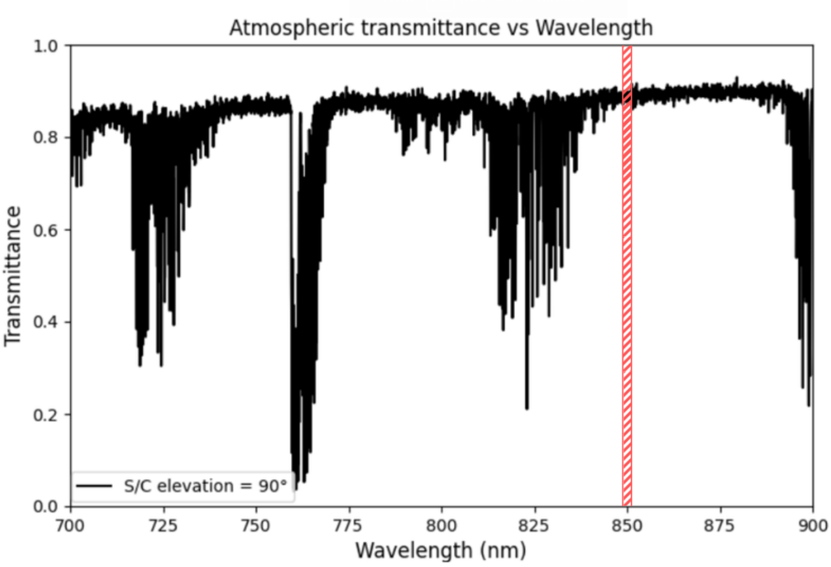

Figure 5.1: S/C photon transmissivity at zenith propagating along the atmosphere at different wavelengths.

In Fig 5.1 we show the results of our simulation where the transmissivity is plotted as a function of different wavelengths. We obtain a transmissivity of the signal for this atmosphere along zenith of $\tau_{atm} = 0.851^{+0.037}_{-0.018}$. The uncertainty is calculated based on the bandwidth filtering margin of ± 1.0 nm. As seen in Fig 5.1 we obtain a high transmittance ratio for the 850 ± 1 nm band compared to other not so reliable wavelengths for optical communications. This result reinforces à posteriori the choice of the 850 ± 1 nm band for our mission. Hence, contributing to the discussion performed in chapter 2.

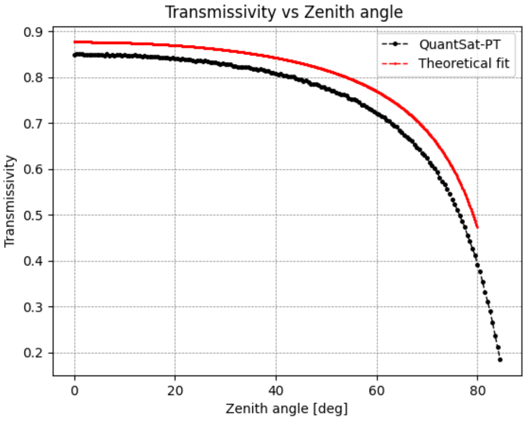

Figure 5.2: Photon transmissivity along the atmosphere for different S/C elevations. A theoretical model is presented in red to verify the results.

With the data from different elevations provided in chapter 3, we can obtain for the chosen wavelength the respective atmospheric transmissivity of the signal for different S/C elevations, as seen in Fig 5.2.

We compare our results for the atmospheric transmissivities along the elevation with a theoretical model which considers: $\tau_{atm} = \tau_{zen}^{sec(\theta_{zen})}$ [29]. Here τ_{zen} is the optical transmissivity at zenith, and θ_{zen} the corresponding zenith angle. As seen in Fig 5.2 we obtain a similar profile compared to the theoretical model. However, our method has a slightly decreased transmittance ratio due to its added complexity. We also compare our results with current state of the art methods [24, 51] which used the MODTRAN

Parameters	Description	Units
RTE solver	Disort [76]	-
Albedo ratio	0.20	-
Clouds file	Generated by libRadtran Mie tool [76]	-
Aerosol file	rural type [84]	-
Aerosol visibility	23.0	km
Atmospheric file	mid-latitude summer	-
Band parameterization	REPTRAN file [86]	-
Bandwidth resolution	1.0	$cm^{-1}bin$
Wavelength grid step	1.0	nm
Wavelength	850.0	nm
Sensor azimuth (ϕ)	0.0	deg
Source azimuth (ϕ_0)	0.0	deg

Table 5.1: Atmospheric parameters during S/C propagation.

6 [88] software. The results of our work are within same order of magnitude compared to the state of the art, thus, allowing us to validate our data.

In the next section, we shall study another effect, the degree of depolarization of our signal after it has encountered the atmosphere. This topic is of the utter importance as our main focus to perform QKD is centered on polarization dependent protocols.

5.3 DoP of signal

In chapter 4 we have talked about the DoP of the background, and how it interferes with our signal. In this section, we shall study the opposite by analysing how our signal depolarizes due to atmosphere. Consider a linerly or horizontaly polarized photon transmitted from the SPS from our S/C which will propagate towards the GS. Rayleigh scattering will occur in different layers of the atmosphere conditioning the degree of polarizability of our photons. Our objective is understand how much does it vary and what is the respective magnitude of error in our signal due to basis misalignment from this depolarization.

We shall consider the same atmosphere profile as it was defined in table 5.1, however this time, the chosen RTE solver is Mystic [75]. As it was mentioned in section 5.1, Mystic offers an enormous advantage with the forward tracing mode in polarized photonics, where with Monte-Carlo it computes and traces each photon along their random path through the atmosphere.

We classify the polarization using the Stokes parameters (S_0, S_1, S_2, S_3) = (I, Q, U, V) = ($Ex^2 + Ey^2$, $Ex^2 - Ey^2$, $2E_xE_ycos(\delta)$, $2E_xE_ysin(\delta)$) [89], for which their combination allows to characterize any type of photon polarization with DoP defined by $DoP = \frac{\sqrt{Q^2+U^2+V^2}}{I}$. Here E_x and E_y are respectively the x and y components of the photon's electric field in a 2D plane.

We consider that all our sent photons are linearly polarized $\gamma = (1, 1, 0, 0)$ during a timestep of 10s between acquisitions for each S/C elevation. The Monte-Carlo method is propagated consider-

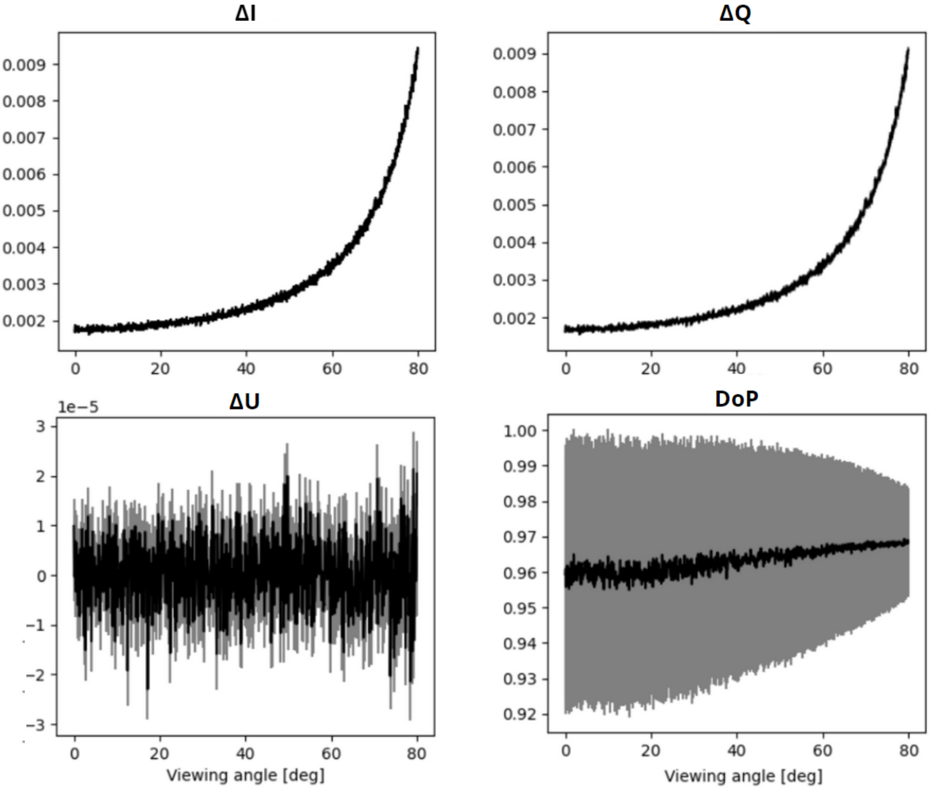

Figure 5.3: Variance for the Stokes parameters and degree of photon depolarization in terms of S/C elevation.

ing a SPS frequency of 100 MHz. The obtained results for the variance of the Stokes parameters $(\Delta I, \Delta Q, \Delta U, \Delta V)$ and DoP in terms of the S/C elevation can be seen in Fig 5.3. The error is shown in grey, which was calculated from the standard deviation performed by the Monte-Carlo method for each elevation.

In Fig 5.3 on bottom right, we obtain at the horizon $DoP(\%) = 96.1 \pm 3.9\ \%$ which means that depolarization can disturb the signal within a range of $[0.2, 8.1]\%$. By increasing the elevation, we observe a decrease in the Monte-Carlo root Mean Square Error (MSE) reaching a $DoP(\%) = 96.8 \pm 1.6\%$ at zenith.

We also observe in Fig 5.3 that the two parameters ΔI and ΔQ compensate each other from the definition of DoP ($\frac{\Delta Q}{\Delta I}$). This is further analysed in Fig 5.4 where ΔI and ΔQ deviations are studied in terms of the elevation obtaining a fit for the curve of $\Delta Q = 0.97126\Delta I - 0.00002$. This curve fit identifies a clear asymmetry between the two parameters, meaning that with the increase of elevation a slight increase of DoP shall occur. Thus, we obtain $\Delta I_{80} - \Delta I_0 = (9.42 \pm 0.11) \times 10^{-3}$ and $\Delta Q_{80} - \Delta Q_0 = (9.01 \pm 0.11) \times 10^{-3}$. In Fig 5.3 on bottom left we also observe that ΔU oscillates around zero. As ΔU oscillates up to an order of 10^{-5}, it contributes near to nothing to the overall DoP result.

Also as the circular polarization is not present from atmospheric Rayleigh scattering the plot of $\Delta V = 0$ has no relevance for the overall results.

We conclude this topic with a comparison of our results with the work of M.Toyoshima et al [90]. The authors of that work experimentally obtained the DoP of a circularly polarized photon source from a S/C propagating along the atmosphere, obtaining a photon depolarization up to 4.0%. By comparison, we achieve similar results with discrepancies within the uncertainty range. Moreover, we conclude that the main source of error for the photon basis misalignment is not only the depolarization ratio from the atmospheric disturbances, but also the intrinsic optical configuration misalignment between S/C and GS which typically deviates within a range of $[3, 5]\%$ [27].

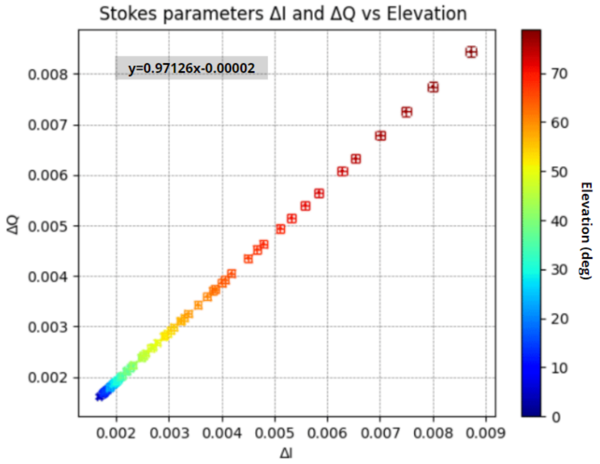

Figure 5.4: ΔI and ΔQ comparison in terms of the S/C elevation.

5.4 Atmospheric influence on QKD

A general overview of our atmosphere has been defined as well as the transmittivity and perturbation ratio due to the atmosphere on our original signal. We shall now use this added layer of our simulator to refine our results for the sifted key rate and QBER for both, BB84 and E91 polarization dependent protocols.

5.4.1 BB84

As it was mentioned way back in chapter 3 we can compute the key rate based on the expected photon fraction received at the GS from Equation 3.4. However this time, the atmospheric transmissivity (τ_{atms}) and the photon DoP (γ_{DoP}) are added to Equation 3.4 for each S/C elevation. Allowing us to obtain in Fig 5.5 and in Fig 5.6 the expected photon fraction and the resulting key rate respectively, with added atmospheric influence and DoP disturbances.

The expected photon fraction calculates the ratio for which the transmitted photon reaches the GS. This means that we are only targeting photons originated from the S/C apparatus. Thus, the SNR term obtained from chapter 4 wont have any influence on the photon fraction result, being not considered in Fig 5.5 and Fig 5.6. On the other hand, in the QBER calculation as we are comparing the error rate between Alice's and Bob's basis, we are looking from the GS perspective for which the SPD triggers for

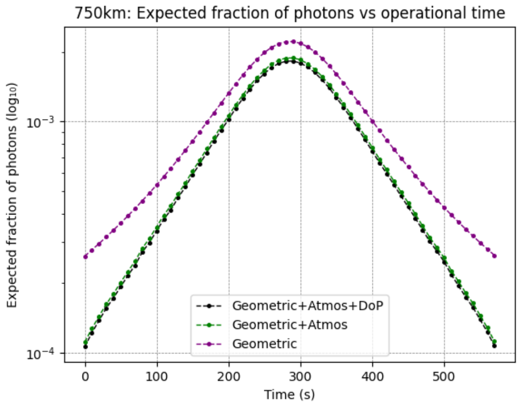

Figure 5.5: Expected photon fraction at the GS from the geometric, atmospheric and DoP terms along each S/C elevation.

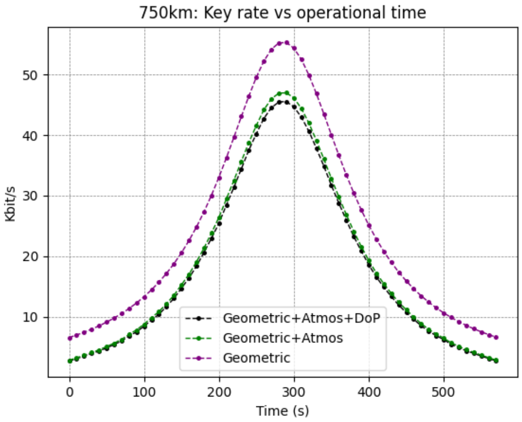

Figure 5.6: Sifted key rate at the GS based on the influence from the geometric, atmospheric and DoP terms along each S/C elevation.

any type of photon interaction. Meaning that in this case the SNR term must be considered as it has a dominant impact on the overall results.

By comparing each term in Fig 5.6 that contributes to a decrease in the sifted key rate, we are able to obtain Fig 5.7. More specifically in Fig 5.7, we compare the two added terms τ_{atms} and γ_{DoP} with our previously defined geometrical model which was obtained in chapter 3. Thus, at zenith, a sifted key rate loss of $15.04 \pm 0.31\%$ is obtained by considering an added τ_{atms} term and a $17.66 \pm 0.55\%$ loss is computed by also adding the γ_{DoP} term. At high zenith angles this loss reaches a key rate decrease of 60% as seen in Fig 5.7.

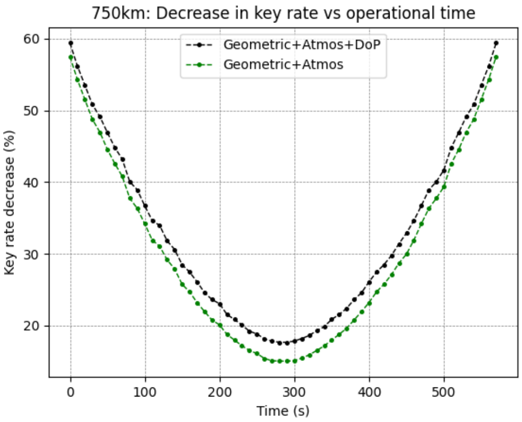

Figure 5.7: Key rate loss between the geometric term and the DoP and atmospheric attenuation added terms.

From Equation 3.5 we can calculate our new QBER by introducing the previously mentioned atmospheric and background terms (τ_{atms}, γ_{DoP}, γ_{SNR}) into the generalized loss function $\mu(\theta)$. Allowing us to obtain Fig 5.8 which represent the corrected QBER in terms of the elevation. A comparison between our current results for the QBER with the previously defined geometrical term in chapter 3 is also provided in Fig 5.8.

Considering only an added τ_{atms} term, the BB84 protocol does not lose validity for the whole segment. By adding the background noise however (SNR), we obtain at low zenith angles a QBER $\in$

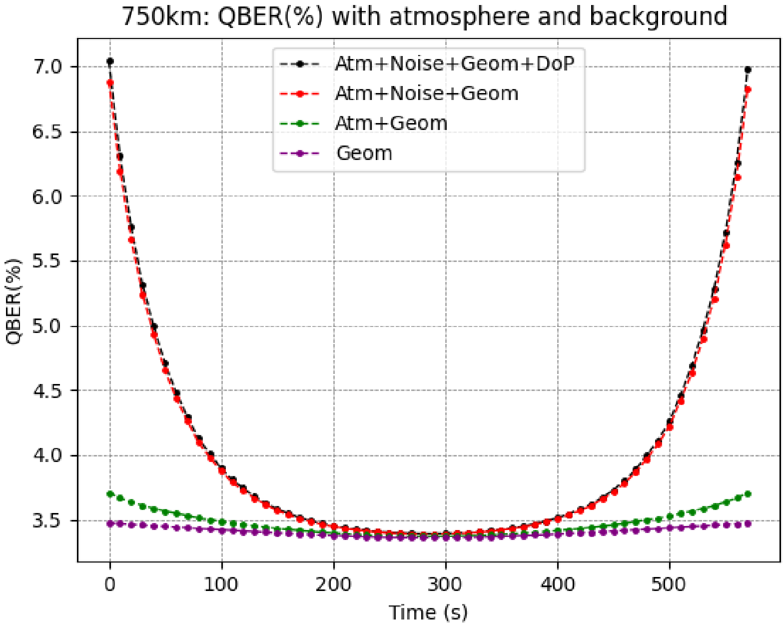

Figure 5.8: QBER comparison between the geometrical term, atmospheric term, background noise and DoP disturbances of the signal along the S/C elevation.

$[3.4, 3.6]\%$. For high zenith angles these values can reach up to 7%. By adding the photon depolarization as a source of error for basis comparison we observe that the results does not change considerably compared to previous results. As seen in Fig 5.8 the more the S/C elevation decreases the more dominant the added terms become.

The simulation uncertainties are calculated as they were in chapter 3 by considering the misalignment of the orbit by not being exactly centered at the GS, this can be seen more clearly in Fig 3.2. We must emphasise that the simulated uncertainty and the real time uncertainty are quite different. The prior is based on the orbit definition which calculates the uncertainty comparing it to the best case scenario of when S/C passes right above the GS. The latter is mostly dependent on the FoV of the tracking telescope [27], the GNSS [49] as well as on the GS beacon for which allows the uncertainty to decrease down to an order of 10^{-3} s to 10^{-5} s.

5.4.2 E91

As mentioned in chapter 3 an analysis on the E91 protocol was not previously performed for the geometric component due to the similarity of the results with the BB84 protocol. However, by adding the background aberration and DoP terms we can finally start to analyse the performance of this protocol. The objective for this section is to obtain the Clauser, Horne, Shimony and Holt (CHSH) test via the E91 protocol, considering only the SNR and the atmospheric DoP terms. Hence, meaning if the photon sent

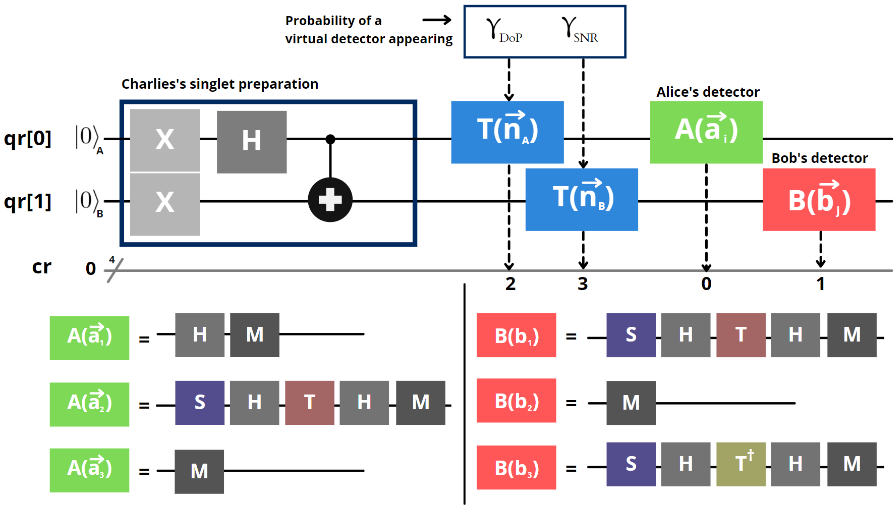

Figure 5.9: Schematic of the quantum circuit used for the E91 protocol. Below, with the use of quantum gates we can rotate the basis for Alice's and Bob's detection.

from S/C does not reach the GS it shall not be considered for the CHSH test validation. Moreover, if a photon is atmospherically absorbed or scattered outside the FoV of the GS, we shall measure at the GS the background influence at the expected time interval of the photon arrival.

We assume that for the simulation of the E91 protocol we use the same parameters as were used for the BB84 which were presented in Table 2.2 and Table 2.3.

We shall use a Qiskit Python toolbox [5], to create a modified E91 protocol which considers the depolarization and attenuation effects. Qiskit is an open source software development kit (SDK) for working with OpenQASM and the IBM Q quantum processors, we shall use it to create our quantum circuit for the E91 protocol. A schematic of the E91 circuit is shown in Fig 5.9. The loss is introduced by imposing for each photon a probability to shift their basis, hence, acting as an additional detector between Alice and Bob.

In Fig 5.9 we also define $A(a_i) = \vec{a_i} \cdot \sigma$ and $B(b_j) = \vec{b_j} \cdot \sigma$. Quantum gates are also presented in the same figure [91], where their combination form the detection states for different Bob's and Alice's basis, until the measurement is performed.

The main difference from the BB84 protocol is the use of three different basis for Alice $\{0, \frac{\pi}{4}, \frac{\pi}{2}\} = \{a_1, a_2, a_3\}$ as well as for Bob $\{\frac{\pi}{4}, \frac{\pi}{2}, \frac{3\pi}{4}\} = \{b_1, b_2, b_3\}$ which allows us to perform the CHSH test to obtain the correlation coefficient (S) between the basis sent from S/C and received at the GS. Charlie is also introduced, with the main purpose to prepare and propagate the singlets. We shall study this protocol in terms of the correlation coefficient between the S/C and GS basis, which is defined by [25]:

---

[5] Documentation for the 0.30.1 version is available.

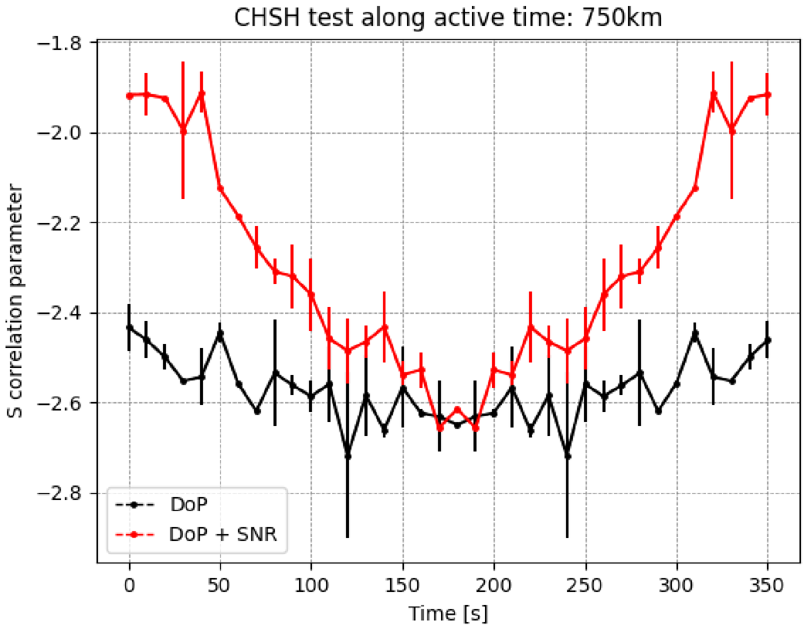

Figure 5.10: Correlation coefficient S during the active time of the mission. γ_{DoP} and γ_{SNR} parameters are present in order to study the vulnerability of the E91 protocol for our mission.

$$S = E(a_1, b_1) - E(a_1, b_3) + E(a_3, b_1) + E(a_3, b_3) \tag{5.2}$$

$$E(a_i, b_j) = \frac{N_{++} + N_{--} - N_{+-} - N_{-+}}{N_{++} + N_{--} + N_{+-} - N_{-+}} \tag{5.3}$$

Here N_{xy} is the number of coincident counts in a pair of x, y states from the Alice's transmitted and Bob's received photons.

Ideally $|S| = 2\sqrt{2}$ which tells us that the basis are anti-correlated between Alice and Bob, showing the viability of the protocol for secure communications. Without any environmental or geometrical perturbations considered, if the correlation coefficient follows $-\sqrt{2} \leq S \leq \sqrt{2}$, it means that either the received photons are not truly entangled (which could be due to an attempt to eavesdrop) or that there is some problem with the measurement device [92].

For our mission, this means that CHSH test cannot identify an eavesdropper if the signal is disturbed to a point where the following inequality $-\sqrt{2} \leq S \leq \sqrt{2}$ is always valid. Hence, we study the effect of the γ_{DoP} and γ_{SNR} on the CHSH test validating the viability of E91 for our mission. For this simulation we consider a basis misalignment of 3% between the S/C and GS [27]. Similarly to what was done with the BB84 protocol, we evaluate the γ_{DoP} and γ_{SNR} components in terms of the correlation coefficient (S) during the active time of the mission, as seen in Fig 5.10.

As seen in Fig 5.10, with only γ_{DoP} component present we obtain a valid S parameter of $\in [-2.67 \pm 0.23, -2.44 \pm 0.04]$. By introducing the SNR our CHSH test shifts. Where the Bell's test for the E91 protocol is only valid between $\in [46, 321]$ s. If the geometrical term and atmospheric absorption term is also considered, using this method the E91 protocol loses its validity. All the uncertainties are calculated based on the obtained standard deviation for different trials of the same E91 simulation at each S/C elevation.

In the next chapter, we are going to analyse the turbulent behaviour of the atmosphere with a statistical model. Characterizing the main effects which lead to the perturbation and scintillation of the signal. Additionally, we are going to add another layer of complexity to our simulator by not only considering the turbulent behaviour but also taking into account the pointing error of the S/C.

6

Turbulence losses

6.1 Turbulent effects

We encounter turbulence in everyday life, from the flow of water to smoke coming from a possible burnt cake that you forgot in your oven while reading this work. What do all these examples have in common? The chaotic behaviour of particles.

In this section we are centering on this specific topic. We are going to study the chaotic behaviour of particles or eddies which perturb our QKD optical path in the atmosphere. The objective here, is to define the most dominant effects and study the respective optical losses. In section 6.2, we shall reformulate our transmissivity model into a statistical one accounting for all the turbulent effects as well as adding the off pointing behaviour of the satellite.

As seen in Fig 6.1 we shall consider three main effects: Beam spreading , scintillation and beam wandering [93]. These effects are dependent on the relative size between the eddies of the turbulent layer and the beam width of the signal. As shown in Fig 6.1 for beam width sizes bigger than the eddies radius we consider that the beam spreading effect is dominant. If the size is of the same order of magnitude then scintillation dominates, this effect is mainly relevant for satellite downlinks. Beam

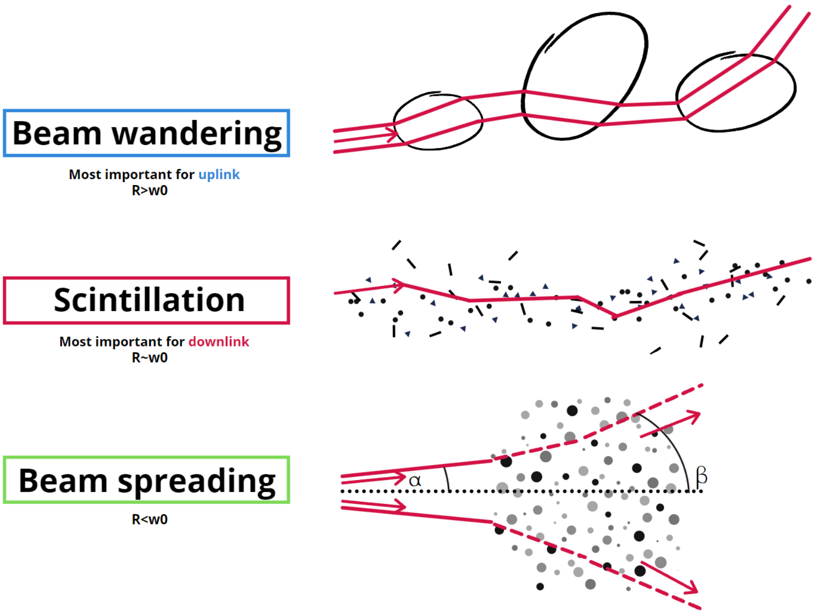

Figure 6.1: Main turbulent effects: Beam wandering, scintillation and beam spreading all dependent on the eddies size. Arrows in red represent the direction of photon propagation.

wandering mostly occurs for uplinks, this can be justified due to an immediate entry of the signal in the atmospheric layer where the beam width is at its minimum being much more negligible compared to the eddies radius.

6.1.1 Beam Spreading

To start with, we must first define our turbulent profile. In this section, instead of only choosing a method from the state of the art and applying it, we shall also perform a comparison between each model and its overall performance on the signal loss.

We propose to compare the following three different models:

1. **Model A** [93]: A low zenith model which performs better at lower intensity profiles for the Kolmogorov turbulence [94]. This method is the one chosen for QKD mission as most of the key exchange is performed at low zenith angles.

2. **Model B** [93]: A high zenith model which considers higher orders of magnitude for turbulent perturbations in the Kolmogorov theory. Thus, being more accurate for high zenith angles near the horizon.

3. **Model C** [95]: A more generic non-Kolmogorov model based on the α parameter, if $\alpha = \frac{11}{3}$ we recover the Kolmogorov theory.

For this section we use the Kolmogorov theory [94] which is based on several assumptions. Firstly, it assumes that at high Reynolds numbers the turbulent profile is completely random. Secondly, it assumes that the energy cascades for eddies are only performed in one direction, from large scale eddies to smaller ones. Even though that experimentally [96, 97] a lower fraction of inverted order cascades were also observed. We shall still use this theory as our framework due to the high fidelity of the model for optical communications [98].

The turbulence profile is generally defined by an altitude-dependent refractive index structure coefficient C_n^2. We consider a Hufnagel-Valley model $H - V_{5/7}$ that can be described by [93]:

$$C_n^2 = 0.00594 \left[\frac{w}{27}\right]^2 (10^{-5}h)^{10} e^{-\frac{h}{1000}} + 2.7 \times 10^{-16} e^{-\frac{h}{1500}} + A_0 e^{-\frac{h}{100}} \tag{6.1}$$

Here, w is the root mean square wind speed, and A_0 is a nominal value of C_n^2 at the GS. In this work we consider $w = 21$ ms^{-1} and $A_0 = 1.7 \times 10^{-14}$ m$^{-\frac{2}{3}}$.

In order to have a metric for the disturbed signal performance due to the beam spreading effect, we shall introduce the scintillation index parameter (σ_I). The scintillation index measures the normalised intensity variance of the signal caused by atmospheric turbulence for a chosen turbulent strength.

For the atmospheric turbulent models A, B and C respectively we can describe σ_I by:

$$\sigma^2_{A:I} \approx r_0^2 = 2.24 k^{\frac{7}{6}} sec(\theta_{zen})^{\frac{11}{6}} \int_{h_0}^{h_0+L} C_n^2(h) h^{\frac{5}{6}} dh \tag{6.2}$$

$$\sigma^2_{B:I} = exp\left[\frac{0.49 r_0^2}{(1 + 1.11 r_0^{\frac{6}{5}})^{\frac{7}{6}}} + \frac{0.51 r_0^2}{(1 + 0.69 r_0^{\frac{6}{5}})^{\frac{7}{6}}}\right] \tag{6.3}$$

$$\begin{aligned} \sigma^2_{C:I} &= 4\pi^2 k^2 A(\alpha) \left[\frac{16}{D_R^2}\right]^{1-\frac{\alpha}{2}} \Gamma\left[1 - \frac{\alpha}{2}\right] sec(\theta_{zen}) \\ \times \int_{h_0}^{\frac{L}{sec(\theta_{zen})}} & C_n^2 (1-\Xi)^{\frac{\alpha}{2}-1} \left[\left(\frac{1}{\Xi}\right)^2 - 1\right]^{\frac{1}{2}(\frac{\alpha}{2}-1)} cos\left[\left(\frac{\alpha}{2} - 1\right) arctan(\Xi)\right] dh \end{aligned} \tag{6.4}$$

In Equation 6.2 we define θ_{zen} as the zenith angle relative to the horizon. In Equation 6.3 we present the Rytov parameter r_0 [93] which is defined in Equation 6.2 being another metric for the scintillation intensity acting on a photon when propagated in a turbulent environment.

Finally, in Equation 6.4, α is the spectral index, for which it defines the type of the turbulent theory in study. If we consider $\alpha = \frac{11}{3}$ we recover the Kolmogorov theory. The definition in Equation 6.4 considers a plane wave model for the downlink. As the distance between the S/C and the GS is of the order of 10^3 km, the plane wave model becomes a good approximation for the key exchange simulation. $A(\alpha)$ is described by $A(\alpha) = \frac{1}{4\pi^2}\Gamma(\alpha - 1) cos(\frac{\alpha\pi}{2})$ where $\Gamma(\alpha - 1)$ is the gamma function. $D_R = 2.0$ m is the

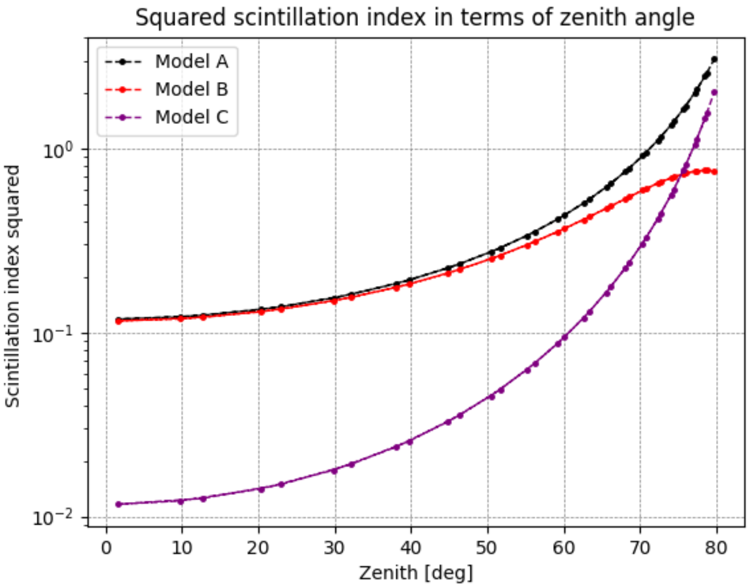

Figure 6.2: Scintillation index squared in terms of the zenith angle for models A, B and C for the atmospheric turbulence.

diameter of the receiver defined in Table 2.3. In Equation 6.4, Ξ is characterized by $\Xi = \frac{16h}{kD_R^2 cos(\theta_{zen})}$.

By combining the σ_I^2 parameter from Equation 6.2, 6.3 and 6.4 with the distance profile of the satellite defined in chapter 3 we obtain Fig 6.2. Fig 6.2 compares the performances of models A, B and C via the scintillation parameter squared for the same turbulent profile from Equation 6.1.

We observe in Fig 6.2 that model A which describes more robustly low turbulent profiles differs from other models for zenith angles above 50 degrees, being this discrepancy also described in the work of Larry C. Andrews et al [99]. Thus, becoming not viable at those ranges compared to model B.

Model C which is the most generic one, differs considerably from the rest up to an order in magnitude at low zenith angles. At higher profiles, this model tends to perform similarly to model A. These results for Model C show that the method used for Kolmogorov theory ($\alpha = \frac{11}{3}$) loses in robustness compared to other methods.

We can now study how relevant is the beam spreading effect for our mission. Our objective is to compute the additional geometric losses from the turbulent behaviour. Therefore, we must consider how this turbulent term affects the effective signal's width (W_{eff}). Generally, we can describe the effective signal's width by [100]:

$$W_{eff} = w(1 + T_A) \tag{6.5}$$

Where w is the Gaussian beam width at the GS and T_A is the turbulent scale factor which deforms the overall beam.

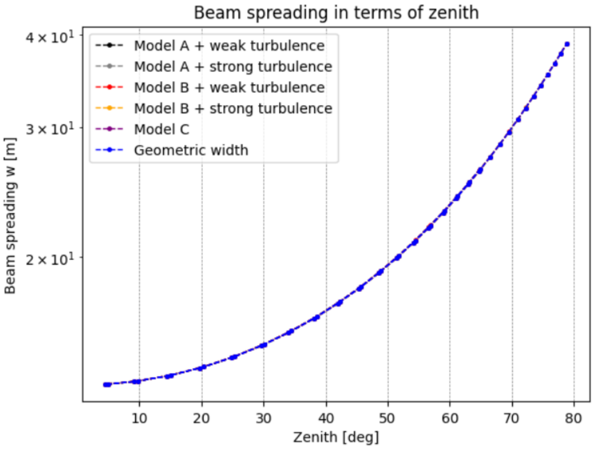

Figure 6.3: Effective beam width considering different models (A, B, C) and fluctuation environments (weak and strong theories) for turbulence.

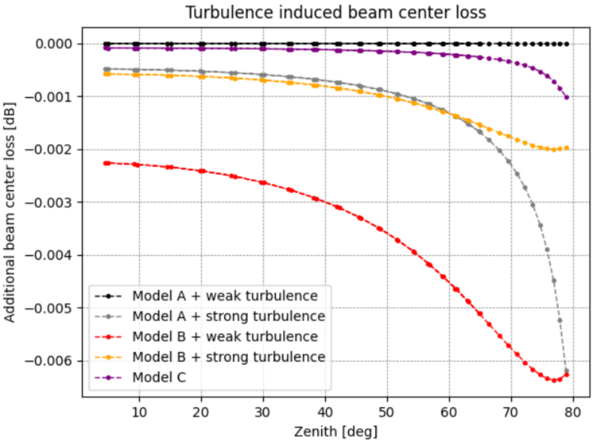

Figure 6.4: Additional signal loss considering different models (A, B, C) and fluctuation environments (weak and strong theories) for turbulence.

Moreover, the T_A factor can differ in A-C models. We shall now consider how our models behave in different fluctuation environments. As we know, if we increase the zenith angle we also increase the turbulence strength. We emphasise that the type of model (A, B or C) optimizes the performance of the results in different environments either in high or low zenith fluctuation theories. In that case, if the model is computed with low zenith angles we define that we are working in a weak fluctuation framework. To define the limit for which the weak fluctuation theory is valid we define from Fig 6.2 the point where models A and B start to differ considerably. This point is considered to be at $\theta_{zen} = 50$ deg for our mission. As a result T_A can then be defined by [100]:

$$T_A = \begin{cases} 1.33\sigma_I^2\Sigma^{\frac{5}{6}}, & \text{if } \theta_{zen} < 50deg, \\ 1.63\sigma_I^{\frac{12}{5}}\Sigma, & \text{if } \theta_{zen} > 50deg, \end{cases} \tag{6.6}$$

Finally, for a generalized version of a non-Kolmogorov turbulence profile (if $\alpha = \frac{11}{3}$ we reduce our framework to the Kolmogorov theory) the turbulent scale factor (T) can be obtained from:

$$\begin{aligned} T_C = -2\pi^2 A(\alpha)\Gamma\left(1-\frac{\alpha}{2}\right)k^{3-\frac{\alpha}{2}}\left(\frac{2L}{kw}\right)\left(\frac{L}{sin(\theta_{zen})}\right)^{\frac{\alpha}{2}-1} sec\left(\theta_{zen}\right)^{\frac{\alpha}{2}} \\ \times\int_0^{\frac{L}{sin(\theta_{zen})}} C_n^2\left(\frac{hsin\left(\theta_{zen}\right)}{L}\right)^{\alpha-2} dh \end{aligned} \tag{6.7}$$

Combining Equation 6.5 with Equation 6.6 and 6.7 for each S/C elevation defined in chapter 3, we compute in Fig 6.3 the effective width (w_{eff}) from the turbulence spreading. We consider the performance of models A and B in two different frameworks for weak and strong fluctuation theory.

As seen in Fig 6.3, the influence from the spreading effect is minimal, only differing our results up to

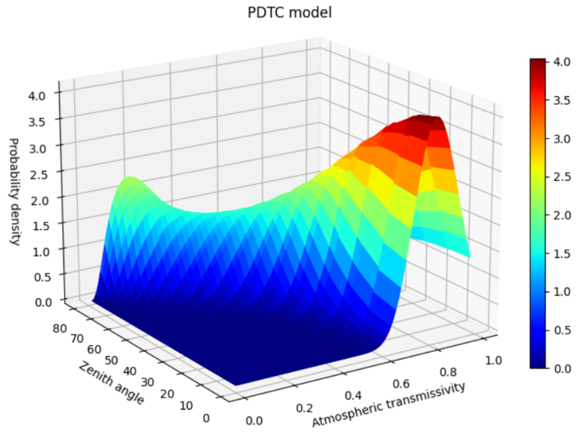

Figure 6.5: Probability density as a function of the S/C zenith angle and the atmospheric transmissivity. The color bar on the right is a metric for the probability density.

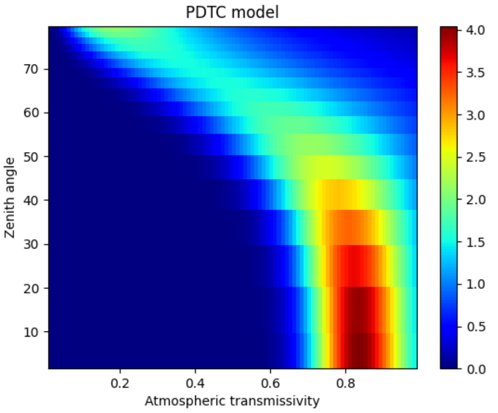

Figure 6.6: A top view of Fig 6.5. Probability density as a function of the S/C zenith angle and the atmospheric transmissivity. The color bar on the right is a metric for the probability density.

an order of 10^{-2} m for the beam divergence. At high zenith angles when considering a strong turbulent environment we obtain a maximal added beam width of $w_{turb} = 0.0634$ m from the turbulent influence.

In order to compare the three models we also have computed in Fig 6.4 the added loss ($Loss = 20log\left(\frac{w}{W_{eff}}\right)$) that our signal is subject to by considering the added photon spreading effects. As described in Fig 6.4 we observe that in a strong fluctuation environment the model A ($\theta_{zen} > 50$ deg) loses its robustness to describe the turbulent behaviour, thus, the additional loss exceeds to -0.006 dB in that domain compared to other models. The same effect occurs for model B at low zeniths, inaccurately describing the turbulent behaviour compared to model A with losses reaching -0.002 dB at low zenith angles. Model C for high zenith angles reaches to an order of -0.001 dB.

From all this we understand that the beam spreading effect exists for our mission however it loses relevance compared to the main geometric term studied in chapter 3, where by choosing the appropriate geometric parameters the losses could vary up to -10 dB.

6.1.2 Scintillation effect

For this section, we shall study the scintillation effect which is described by an oscillation in the intensity of the received signal resulting in a sparkling of the target over space and time. The objective is to compute the order of magnitude of the additional losses by considering this effect.

As the scintillation of the signal occurs within a certain probability at the receiver, we shall consider a statistical model for the turbulent behavior [101]. We consider that for weak turbulence the intensity statistics can be described with a PDTC with a log normal profile, which ignoring phase-front fluctuations can be viewed by [102, 103]:

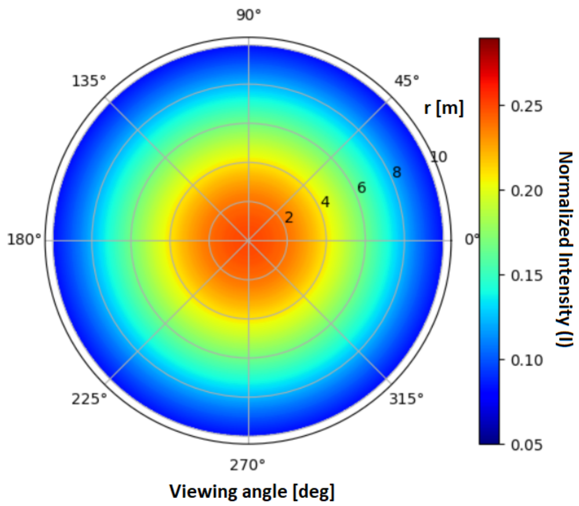

Figure 6.7: Normalized intensity profile without the scintillation effect viewed when S/C is at zenith right above the GS.

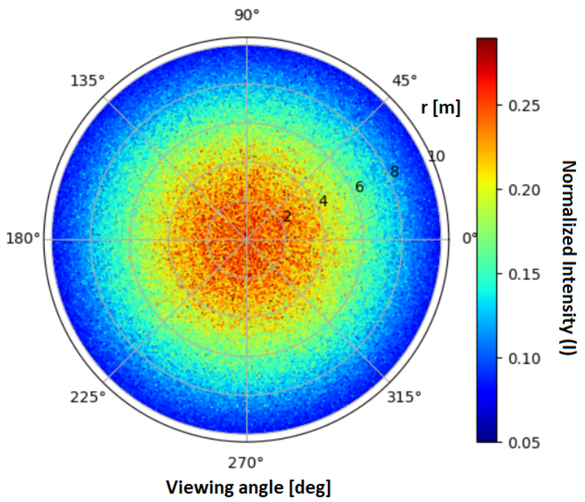

Figure 6.8: Normalized intensity profile with the scintillation effect viewed when S/C is at zenith right above the GS.

$$p(\eta) = \frac{1}{\sqrt{2\pi}\sigma_I \eta} exp\left(- \frac{\left(ln(\frac{\eta}{\eta_0}) + \frac{1}{2}\sigma_I^2 \right)^2}{2\sigma^2} \right) \tag{6.8}$$

Equation 6.8 allows us to create a transmission probability mapping at the receiver dependent on the SPS power. Here σ_I is the scintillation index defined in section 6.1.1 and η is the atmospheric transmissivity in a turbulent domain.

We consider the S/C trajectory from chapter 3 and the scintillation model A (σ_I) from section 6.1.1, to obtain Fig 6.5. If we project Fig 6.5 from a top view, we obtain Fig 6.6. From the results we obtain that only for zenith angles above 50 degrees the function shifts more steeply, indicating the introduction of the strong turbulent behaviour.

We can describe the loss profile by considering instead of a PDTC a full irradiance mapping at the receiver from the S/C view, as seen from the following equation [100]:

$$p_I(\eta) = \frac{1}{\sqrt{2\pi}\sigma_I I(r,L)} exp\left(- \frac{\left(ln(\frac{I(r,L)}{<I_0(r,L)>}) + \frac{1}{2}\sigma_I^2 \right)^2}{2\sigma^2} \right) \tag{6.9}$$

Here, I(r,L) is the irradiance profile, r is the radius from the center of the receiver and L is the optical path. $\langle I(r,L) \rangle$ can be defined by $\langle I(r,L) \rangle = A(\frac{w_0}{w_I})^2 exp(\frac{-2r}{w_I}^2)$ [100], where A is a normalization constant and w_0 is the Gaussian beam width.

In Fig 6.7 we obtain the usual normalized Gaussian intensity profile viewed when the S/C is at zenith right above the GS. The Gaussian profile is a function of the S/C viewing angle as well as the radius from the center of the GS.

In Fig 6.8 we consider the scintillation effect, as seen the profile is highly disturbed compared to Fig 6.7. In order to study the influence from scintillation effect we have considered the absolute mean error (%) between the two intensity profiles present in Fig 6.7 and Fig 6.8 respectively, allowing to obtain Fig 6.9. As a result, a maximal deviation of 30% is computed for the intensity profile, meaning that signal losses can also reach that order of magnitude. As a result, in a worst case scenario, among all three effects, the scintillation remains the most dominant between the signal and turbulence interaction over time.

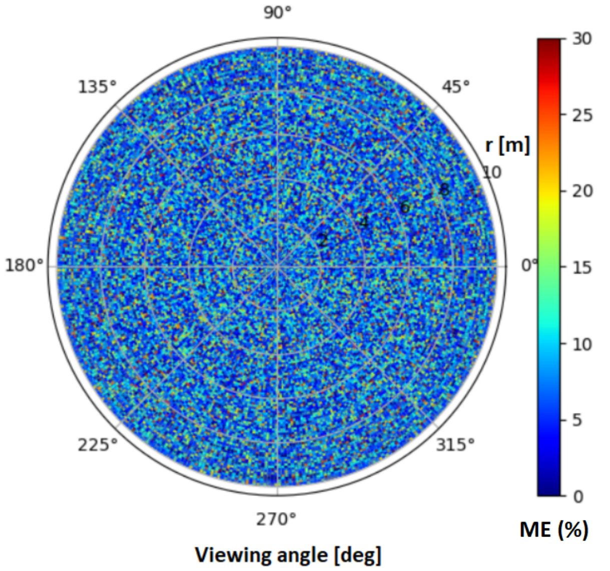

Figure 6.9: Absolute mean error between Fig 6.7 and Fig 6.8 viewed when S/C is at zenith right above the GS.

6.1.3 Beam wandering

For this section we shall consider the effect of beam wandering which describes how the atmospheric turbulence creates time-dependent random lateral beam displacements. To study the order of magnitude of such effect we must consider the PDTC model. There, we must compare the intrinsic pointing error influence with the beam wandering.

To express the S/C pointing error we use the Weibull distribution [26, 93]:

$$P = \frac{r}{\sigma_r^2} exp\left(-\left(\frac{r}{\sqrt{2}\sigma_r}\right)\right) \tag{6.10}$$

Here, σ_r is the standard deviation for the Weibull distribution and r is the shift deflection distance from the GS center. Also, σ_r can be described by [29]:

$$\sigma_r = \sqrt{(\theta_p L)^2 + \sigma_w^2} \tag{6.11}$$

Where θ_p is the pointing error of the S/C and σ_w is the variance of the beam center due to turbulence. In weak turbulence theory considering a collimated beam in Kolmogorov turbulence with infinite outer scale, the σ_w term can be defined by $\sigma_w = 1.919 C_n^2 z^3 (2w_0)^{-\frac{1}{3}}$. Here, C_n^2 is traced from Equation 6.1, z is the optical path in the atmosphere and w_0 is the beam waist when entering the atmosphere.

We consider the distance profile of the S/C from chapter 3 as well as $\theta_p = 1.0\mu m$ from the precision of the Micius mission S/C [26]. Thus, obtaining $(\theta_p L)^2 = 0.56m^2 >> 10^{-3}m^2 = \sigma_W^2$. As seen, the order of magnitude for the beam wandering effect is near to negligible, but this is to be expected considering its physical interpretation. Photons from the S/C are considered to propagate 97% of the time in near vacuum (see chapter 4). When finally the signal enters the upper atmospheric layers (∼ 20 km) the size of the beam width is already considerable ($w_0 = 13.17 \pm 0.14$ m at high zenith angles) compared to the eddies mean radius [104]. The uncertainty has been calculated based on the simulation off center from the optimal orbit, being it more clearly described in Fig 3.2.

In the following section we shall add another layer of complexity to our simulator, by considering the off pointing behaviour as well as the turbulent effects described in sections. 6.1.1, 6.1.2 and 6.1.3.

6.2 A PDTC model for losses

If we had left it here neither I nor the reader would appreciate the product of sections. 6.1.1, 6.1.2 and 6.1.3. We shall complete this chapter with some applications towards our simulator by applying what was learned to our results.

Let us consider the PDTC statistical model which describes the transmission efficiency (T) received at GS by Equation 6.12 [105]:

$$T^2 = T_0^2 exp\left(-\left(\frac{r}{R_1}\right)^{-\lambda_1}\right) \tag{6.12}$$

T_0 is the maximal transmission coefficient for a given beam size (W), λ_1 and R_1 are the shape and scale parameter respectively, which can be defined by [105]:

$$T_0^2 = 1 - exp\left(-\left(\frac{a\sqrt{2}}{W}\right)^2\right) \tag{6.13}$$

$$\lambda_1^2 = 8\frac{a^2}{W^2}\frac{exp\left(\frac{-4a^2}{W^2}\right) I_1\left(\frac{4a^2}{W^2}\right)}{1 - exp\left(\frac{-4a^2}{W^2}\right) I_0 \frac{4a^2}{W^2}}\left[ln\left(\frac{2T_0^2}{1 - exp\left(-\frac{-4a^2}{W^2}\right) I_0 \frac{4a^2}{W^2}}\right)\right]^{-1} \tag{6.14}$$

$$R_1 = a\left[ln\left(\frac{2T_0^2}{1 - exp(-\frac{-4a^2}{W^2}) I_0 \frac{4a^2}{W^2}}\right)\right]^{-\frac{1}{\lambda_1}} \tag{6.15}$$

The $a = \frac{D_R}{2}$ parameter is the radius of the receiver and r is its beam-deflection distance. I_0 and I_1 are the modified Bessel functions of the first kind. Considering that the beam center is distributed accordingly to the profile described by Equation 6.10, we can combine it with Equation 6.12, 6.13, 6.14 and 6.15 to obtain the transmission coefficient accounting for the inner off pointing profile of the S/C. We assume that the beam fluctuates around the aperture center, allowing us to obtain the PDTC

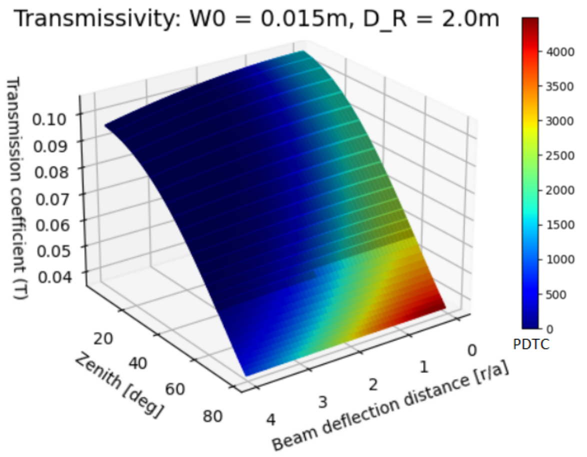

Figure 6.10: Transmission coefficient in terms of S/C elevation, the PDTC and deflection distance r/a.

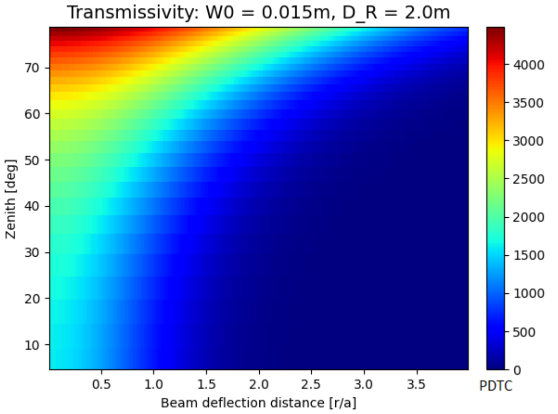

Figure 6.11: Top view of Fig 6.10. Deflection distance r/a in terms of the S/C elevation and the PDTC.

($\mathcal{P}$) [29, 105]:

$$\mathcal{P}(T) = \frac{2R_1^2}{\sigma_r^2 \lambda_1 T} \left(2ln\left(\frac{T_0}{T}\right)\right)^{\frac{2}{\lambda_1}-1} exp\left[-\frac{1}{2\sigma_r} R_1^2 \left(2ln\left(\frac{T_0}{T}\right)^{\frac{2}{\lambda_1}}\right)\right] \tag{6.16}$$

We shall now use Equation 6.16 with the S/C to GS distances from chapter 3. This allows us to obtain in Fig 6.10 the transmission coefficient containing the geometrical and turbulence behaviour (T) in terms of the S/C zenith angle, the probability for beam deflection $\frac{r}{a}$ from the center of the receiver and the effective distance from the center of GS.

From Fig 6.11 we can understand the statistical behaviour of the turbulent and geometric off pointing models. For low zenith angles, beam deflection probability is close to zero. If the transmissivity coefficient is squared, we obtain the total transmissivity (T^2) of the signal all the way from the S/C to GS. By normalizing the PDTC for each S/C zenith angle we obtain the accomulative probability of an event. In our case, for low zenith angles, an accumulative probability of 46.23% is calculated for our beam deflection to be within a range of $\frac{r}{a} \in [0.0, 0.5]$. On the other hand, for high zenith angles the elliptic behaviour of the beam is dominant. Therefore, an increased turbulent deflection is shown for higher zenith angles. Thus, we shift the accumulative probability to higher deflection distances decreasing it for lower deflections ratios ($\frac{r}{a} \in [0.0, 0.5]$) down to 16.45%.

To have a better understanding of this behaviour, we propose to renormalize the PDTC to one for each zenith angle. Allowing to calculate the beam mean deflection ratio for each zenith angle as seen in Fig 6.12. Afterwards, with the use of the LMFIT Python package [1] we are able to apply a polynomial regression to our data for a $\mathcal{O}(3)$ order polynomial. Hence, allowing to obtain a correspondence of $\chi^2 = 9.8032 \times 10^{-04}$ and $\chi_\gamma = 2.2798 \times 10^{-05}$ for the Chi-Square and reduced Chi-Square parameters,

---

[1] Documentation for the 1.0.2 version available.

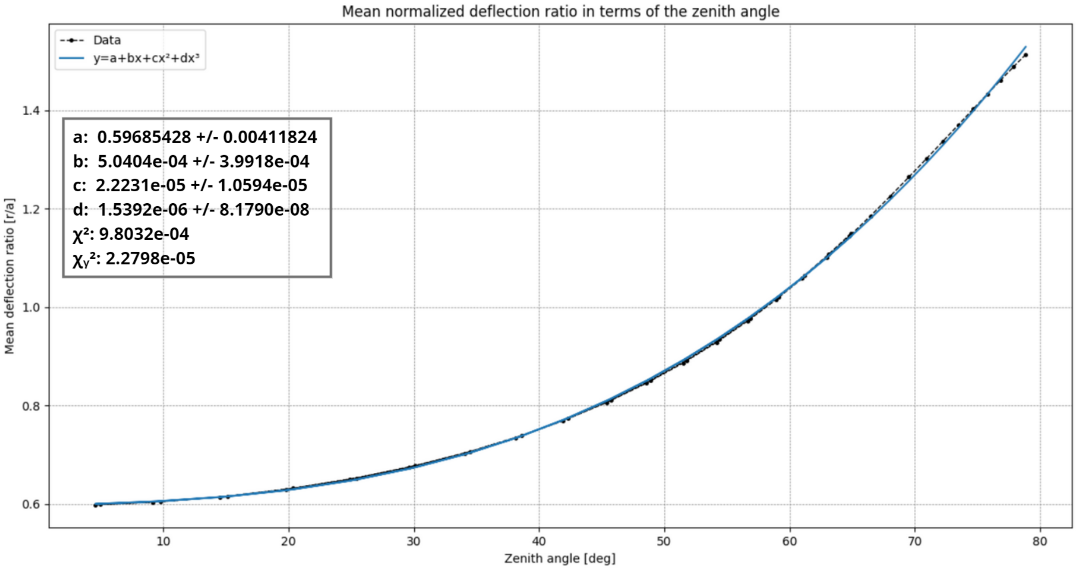

Figure 6.12: Mean beam deflection distance considering a mean renormalization of the PDTC parameter for each zenith angle of the S/C. A polynomial regression of $\mathcal{O}(3)$ order is performed, to characterize the statistical off pointing behaviour of our system.

respectively.

A mean beam deflection of $\frac{r}{a} = 0.60$ is obtained for low zenith angles increasing up to $\frac{r}{a} = 1.51$ for high zenith angles. The obtained regression parameters of $y = a + bx + cx^2 + dx^3$ are presented in Fig 6.12.

The results shown achieve the same order of magnitude for the transmissivity coefficent (T) being in accordance to the work of D. Yu. Vasylyev et al. [105] and Daniele Dequal et al. [29], as well as with the equivalent eliptical model for QKD from the work of Carlo Liorni et al. [28]. Daniele Dequal et al. [29] obtains a transmission efficiency (T^2) of 1.6% for an altitude of 750km. This was performed, considering the geometric parameters for GS and S/C focusing on the Micius mission. By considering the same geometrical parameters for our mission, we obtain similar results within the same order of magnitude compared to the work of Daniele Dequal et al.

In the next chapter, we shall propose a new method for atmospherically perturbed signal correction of phase-dependent QKD protocols. Combining Artificial Neural Networks (ANN), Adaptive Optics (AO) with previous data for the intensity profiles of the signal.

7

A new CNN method for turbulence correction

7.1 Introduction

For the last segment of our work, we shall propose a new method for phase-dependent QKD signal corrections based on a combined CNN and Gradient Descent Optimization (GDO) algorithm.

Instead of having the BB84 and E91 protocols polarization encoded as it was considered in previous chapters, we shall study phase encoded schemes. This leads to the use of interferometers, where the encoding is implemented by changing the relative optical path lengths or phase between the internal arms of the interferometer [106].

As a result, the S/C optical key exchanges are now directly dependent on signal aberrations produced by atmospheric turbulence, which introduces spatial and temporal variations in the refractive index of the optical path along the line of sight [107]. This effect leads to broadening the Point Spread Function (PSF) of the intensity profile for the phase-dependent QKD protocols, which significantly increases the tomographic errors. Indeed, for wide-field AO systems, sky coverage becomes the primary source of these types of errors. Therefore, in order to keep an acceptable bandwidth error, this effect must be compensated for such limitation by increasing the integration time of the wavefront [108].

One possible solution to solve this problem is to introduce an additional optical network that provides a PSF reference from well known signal profiles or astronomical bodies, allowing the AO system to locally correct for the turbulence [109]. Here, we propose an algorithm to improve further the signal's performance. However, such a method does not depend on the use of an improved optical system, but dependents solely on the prediction of the proposed algorithm that uses the previous history of intensity profiles of the S/C signals or astronomical objects to make reliable predictions [110].

This solution is beneficial for ground-based telescopes but also for space missions such as Hubble [111], JWST [112] and LiteBird [113] as a way to correct for medium interstellar turbulence. For example, this corrective method may be used to observe a given object in a certain wavelength within the FoV of the telescope behind a turbulent layer created by cosmic dust.

In this work, to that end, we study a closed feedback loop system that feeds on the disturbing intensity profiles. The objective is to adapt the algorithm used in Orbital Angular Momentum (OAM) communications to improve the quality of our space mission by using a more robust atmospheric model with a multi-layer tested turbulence profile. For example, consider a simulated Gaussian beam that propagates towards a telescope: on the one hand, the turbulence intensity is more dominant at lower altitudes, thus allowing the generation of an equivalent phase screen description; on the other hand, it will enable us to classify, predict and deconvolve the distorted image with the estimated PSF on the focal plane, obtaining the corrected version of our signal.

In the next section, we overview the state-of-the-art methods used to correct optical systems. In Section 7.3, we describe the fundamental parameters used to define an atmospheric profile and the signal propagation through the atmosphere. Moreover, in the same section, we present the CNN and GDO components' architecture and the parameters used in our simulation. In Section 7.4, we discuss the performance of CNN and GDO and the accuracy of the signal recovery. Hence, making the comparison with other recent methods. Afterwards, in Section 7.5, we conclude our study, giving an outline of the main results.

7.2 Overview

Here, we present a method based on the framework provided by the work of S.Lohani et al. [114]: the author's goal was to create a robust yet viable strategy to improve satellite to ground optical communications. First, they have determined the GDO images from different OAM modes using an artificial neural

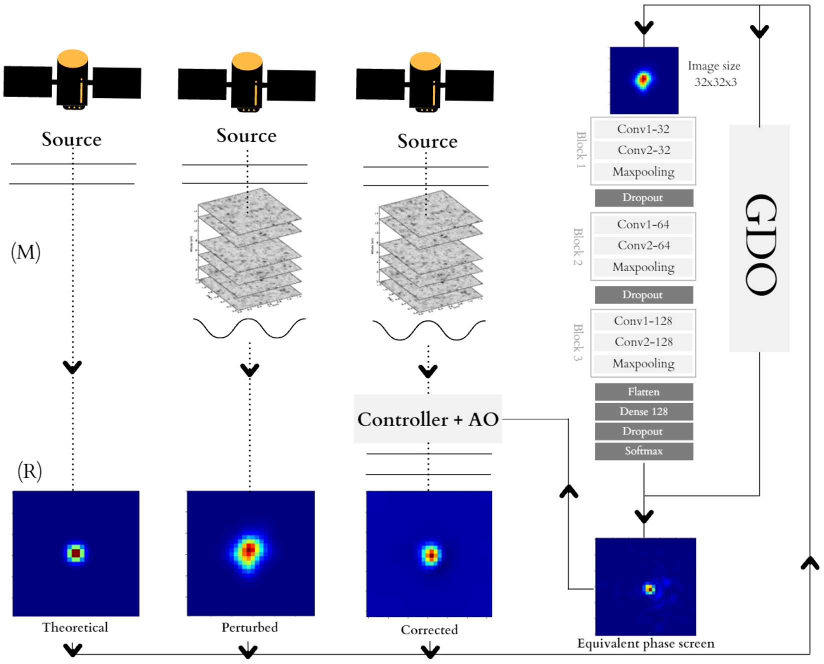

Figure 7.1: Schematic of the turbulence mitigating network, which is composed of adaptive optics, a source, medium with turbulence (M), a receiver (R), and a feedback network with a CNN and a GDO. The optical profiles correspond to the desired image (left), the distorted image due to turbulence (middle), and the turbulence-corrected image at the receiver (right).

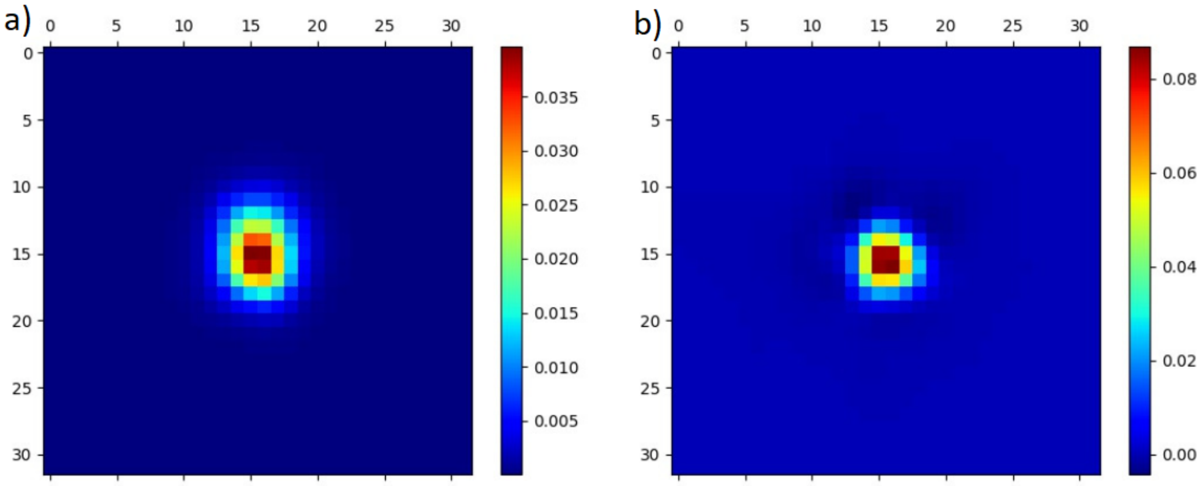

Figure 7.2: Target intensity pattern at the receiver: **a)** With turbulence. **b)** Corrected via Controller.

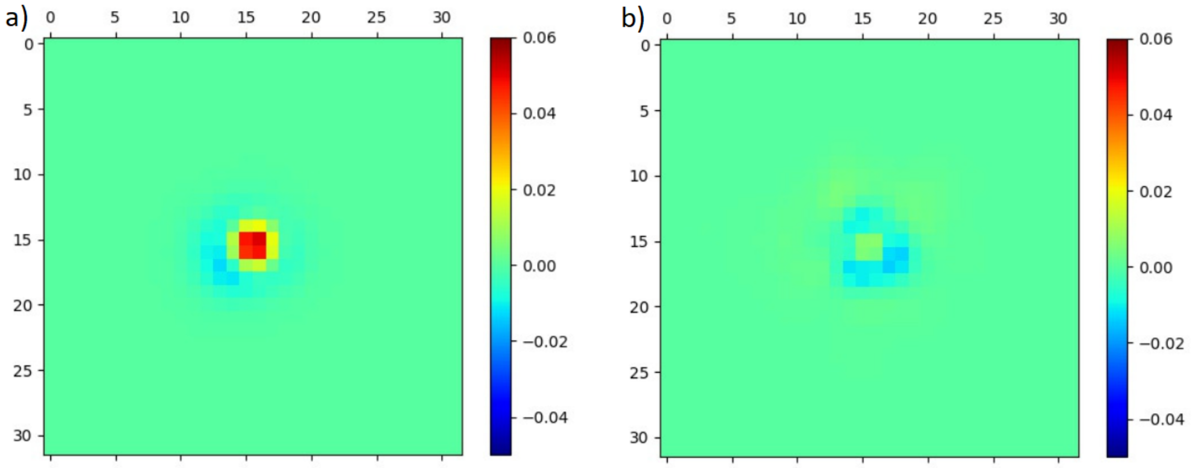

Figure 7.3: Target Mean Error profile compared to the theoretical Gaussian profile with no perturbations: **a)** Before correction. **b)** After correction.

network. Then, they have applied a wavefront correction to the signal source with Spatial Light Modulators (SLM) by changing the wavefront phase to compensate for the single turbulent layer, improving the overall signal.

Other applications of OAM multiplexing communications showed an increase of performance of the mode purity of the distorted vortex beam [115]. For example, improving it from 26.91% to 93.12% through the compensation with a CNN algorithm.

More recently, X. Liu et al. [116] proposed a different approach: a simulation method that assumes the frozen flow hypothesis for the turbulent layer. In this method, the turbulent volume within a single phase screen is modelled as a linear composition of static independent layers, each of them dependent on the wind profile.

The focus was the simulation and prediction of the wavefront slopes data using long short-term memory artificial neural networks, creating a non-linear framework for wavefront prediction. This approach allowed to predict open-loop wavefront slopes at the Shack–Hartmann wavefront sensor [117]. In addition, frame dependence was studied in advance to compensate for the frame delays using AO.

In recent works, M. Chen et al. [118] and H. Ma et al. [119] chose a CNN model to extract features from a phase mapping that rely on Zernike's polynomials to categorize the turbulent layer. In that case, the network is trained to use two extensive data sets based on distorted images as input and Zernike coefficients as an output. The algorithm predicts such coefficients by using the CNN method, which improves the overall signal's performance for different signal to noise ratio conditions. However, the accuracy is dependent mainly on higher-order Zernike polynomials, which are a challenge to consider due to the turbulent layer's arbitrary profile. Therefore a source of error may arise as a result [120].

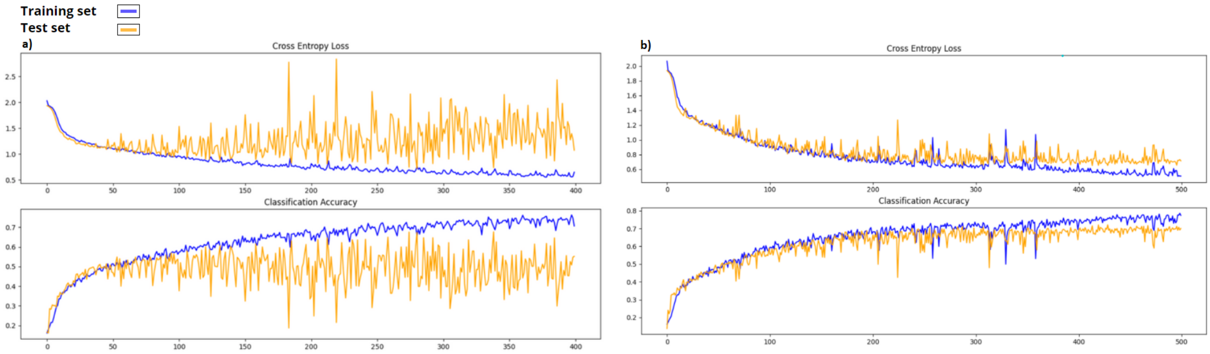

Figure 7.4: Classification accuracy and cross entropy loss: **a)** With a biased test set. **b)** With an unbiased test set.

Conversely, our method uses a realist multi-layered local profile of the atmosphere, which minimizes these errors with added adaptability towards the chosen turbulence.

7.3 Methodology

The current work aims to improve the methods used in optical communications for aberrated phase-dependent protocols, adding a layer of complexity with multiple phase screens compared to previous results [20].

First, we define each phase screen of the atmosphere turbulence via a Kolmogorov phase with the Von Karman power spectrum [121]. Then, we quantify the strength of the turbulence via a refractive index C_n^2. Thus, the overall phase screen can be defined as follows:

$$\Phi(\mathbb{C}_{xy}, r_0) = \mathbb{R}\{\mathcal{F}^{-1}(\mathbb{C}_{xy}\sqrt{\Phi_{xy}(r_0)})\} \tag{7.1}$$

Here $\mathbb{R}$ and $\mathcal{F}^{-1}$ symbolize the real part and the inverted Fourier transform of the function, respectively. $\mathbb{C}_{xy}$ corresponds to an arbitrary complex number for each pixel which was chosen via a Gaussian distribution around zero with white noise. In the simulation, we define $\mathbb{C}_{xy}$ in the GDO segment. $\Phi_{xy}(r_0)$ is the phase power spectrum corresponding to $\Phi_{xy}(r_0) = 0.023 r_0(\nu^2 + 1/L_0^2)^{11/6}$. As for the parameters: ν corresponds to the spatial frequency and L_0 is the outer scale beyond which the power asymptotically flattens. In the simulation $\Phi_{xy}(r_0)$ is predicted in the CNN component based on the Fried parameter, r_0. The dependence on C_n^2 varies on the approach taken [122–124], for this work we choose $r_0 = \{0.423(2\pi/\lambda)^2 \int_{Path} {C_n}^2 dz\}^{-\frac{3}{5}}$, which becomes dependent on the propagation path.

The multi-layer profile is modelled based on the work of M. J. Jee et al. [125]. Here, we use the atmospheric measurements of the site of the Gemini-South telescope located in Cerro Pachón, Chile [126]. It consists of six turbulence layers at altitudes 0.00, 2.58, 5.16, 7.73, 12.89, and 15.46 km with relative

Parameter	Description	Unit	Parameter	Description	Unit
Grid size	32x32	-	Obscuration ratio	0.4	-
Gaussian beam	PDF of a single photon with $\sigma = 0.2$	-	Screen scale	r_0	-
Exposure length	5.0	s	Time step	5.0	ms
Wavelength (λ)	850.0	nm	Altitude of turbulence layers	[0, 2.58, 5.16, 7.73, 12.89, 15.46]	km
Wind Speed in each layer	[14.823, 4.612, 7.177, 10.023, 7.694, 2.857]	m/s	Wind Direction in each layer	[2.006, 6.128, 2.167, 5.024, 4.8159, 2.594]	rad
Inner scale of Turbulence (l)	1.0	mm	Outer scale of Turbulence (L)	25.0	m
Fried parameter (r_0)	[0.08,0.20]	m	Diameter of Telescope	2.0	m

Table 7.1: The setup of parameters for the simulation of the propagator is as follows: we consider a Gaussian beam with a defined standard deviation (σ) propagating through the atmosphere, originating an intensity profile representing a PDF of a single photon. The time step between consecutive observations, screen scale, exposure length and obscuration ratio are the main parameters that characterize the telescope used in this simulation.

weights for the turbulence aberration of the signal being 0.652, 0.172, 0.055, 0.025, 0.074, and 0.022, respectively. For the simulation, the wind direction $\in [0, 6.28]$ rad and velocity $\in [0, 20]$ m/s are chosen arbitrary for each layer. In Table 7.1 we present the parameters used in our simulation.

We consider the propagation of a Gaussian beam light profile in this environment coming from our S/C to our telescope, whereby using and modifying the package Galsim [1] [127] we obtain the resulting intensity pattern at the receiver as seen in Fig 7.2.

Fig 7.1 from left to right show the main method. We start by obtaining the intensity profile of the distorted object, and we also get the non-perturbed data from a known reference source within the same FoV of the telescope. Therefore, now we can get a theoretical profile of our reference source with low to zero signal disturbances.

CNN and GDO model

Next, we include the turbulent profile that leads to obtaining a distorted intensity mapping, representing the PDF of a photon along the FoV.

For the last step, we introduce a feedback system with a controller correlated with AO to compensate for the atmospheric turbulent behaviour. For the unknown turbulent multi-layer profile $\Phi(\mathbb{C}_{xy}, r_0)_{real}$, our objective is to generate an equivalent one, $\Phi(\mathbb{C}_{xy}, r_0)_{pred}$, in order to create the predicted PSF for all

---

[1] Documentation for the 2.3 version available.

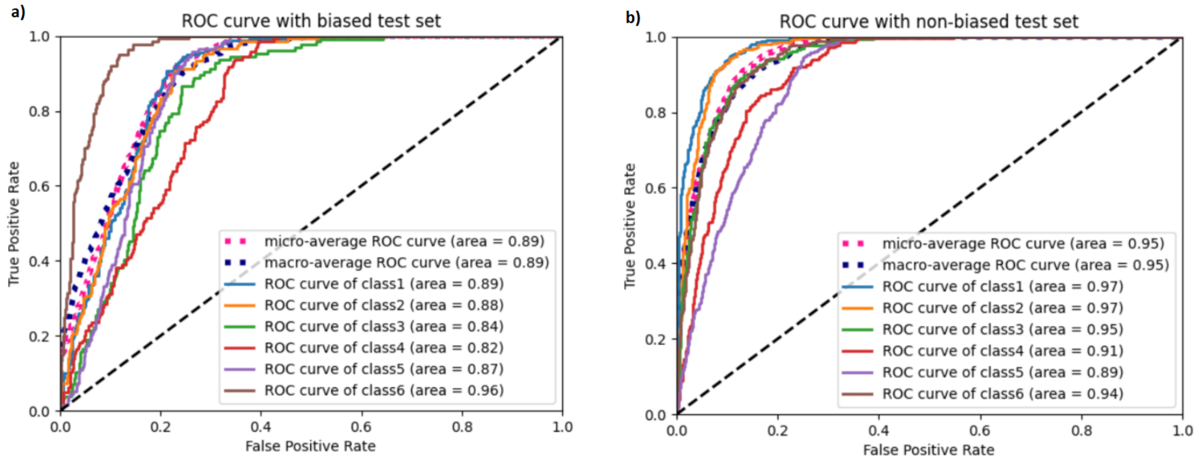

Figure 7.5: ROC curves **a)** With a biased test set. **b)** With an unbiased test set.

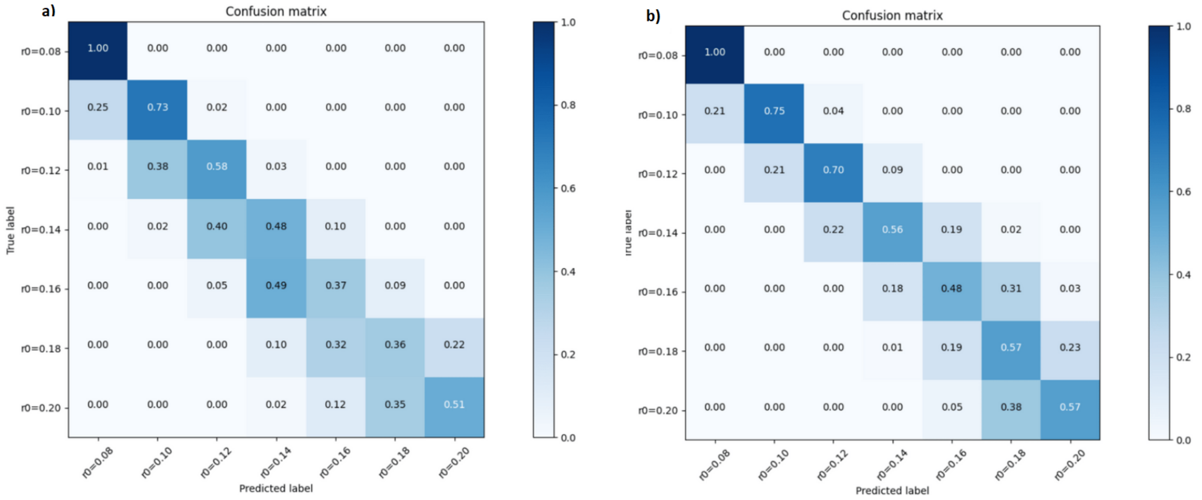

Figure 7.6: Normalized confusion matrices **a)** With a biased test set. **b)** With an unbiased test set.

atmospheric layers. The pre-trained CNN algorithm tries to foresee the intensity profile $\Phi(\mathbb{C}_{xy}, r_0)_{pred}$, by predicting the Fried parameter (r_0).

However, due to the randomness of $\mathbb{C}_{xy}$, we also include a GDO algorithm. Such procedure minimizes the loss function for each pixel by comparing the $\mathbb{C}_{xy}$ parameters between the theoretical and perturbed profiles, thus minimizing the MSE.

As a result, our system correctly predicts the equivalent phase screen profile for turbulence leading to the anticipated PSF. As a final step, we deconvolved the PSF profile with the signal's distorted version, leading to a corrected intensity profile using AO.

We start by correcting the equivalent phase screen of the multi-layer system by introducing the CNN and GDO models responsible for the r_0 and $\mathbb{C}_{xy}$ parameters respectively.

The network is composed of three main blocks, each consisting of two fully connected convolutional networks with 32, 64 and 128 connections (see Fig 7.1), respectively. To prevent over-fitting, we use a 2x2 max pooling mask combined with a dropout function with a ratio of 0.2. In the output, we use a softmax layer to predict the probability for all seven training classes (composed of r_0) having a spacing of $r_0 = 0.02$ m between each other. Additionally, in the test set, the strength of the turbulence is defined randomly within the same range as was implemented for the training classes.

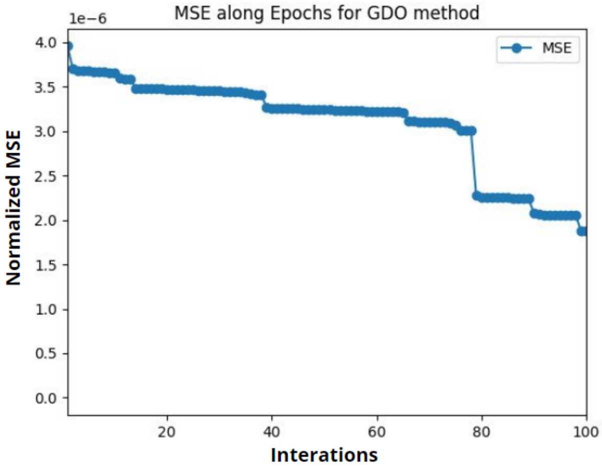

Figure 7.7: GDO performance along the first 100 interactions. The performance is more relevant at lower interactions were the step function has the highest order of magnitude.

Moreover, we provide a second training of the data sets to test the fidelity and the level of overfitting of the results. For each $\mathbb{C}_{xy}$, we implement a Gaussian noise for each layer of the atmospheric turbulence that influences the results directly. We accomplish this procedure by applying a range of deviation up to $r_0 = \pm 0.02$ m in the classification scheme. For the training and testing, we supply the CNN algorithm with 2000 images (array with 32x32). In the fidelity phase, we provide the algorithm 2000 images for training and 1000 images for testing. The simulation runs for 400 epochs. The optimization archived efficiency depends on the stabilization rate of the accuracy and entropy for the training and test sets. For the loss function, we apply a GDO algorithm on $\mathbb{C}_{xy}$ for up to 1000 interactions at each pixel, leading to MSE minimization. This procedure allows finding an optimal convergence point between the distorted and theoretical intensity profiles. Furthermore, the GDO algorithm stops the minimization upon an absolute error of ± 5, between the real and imaginary components of $\mathbb{C}_{xy}$ for both intensity profiles.

7.4 Discussion and Results

In this section, we shall discuss the performance of the CNN and GDO algorithms and comment on our two main results (as seen in Fig 7.2 and Fig 7.3).

In the left panel of Fig 7.2, we show the distorted intensity profile of the S/C signal. The scale describes the probability density of finding a photon in a specific pixel, where the sum of all pixels reaches up to unity. In the right panel of Fig 7.2, we recover the original signal corrected via this feedback in loop CNN

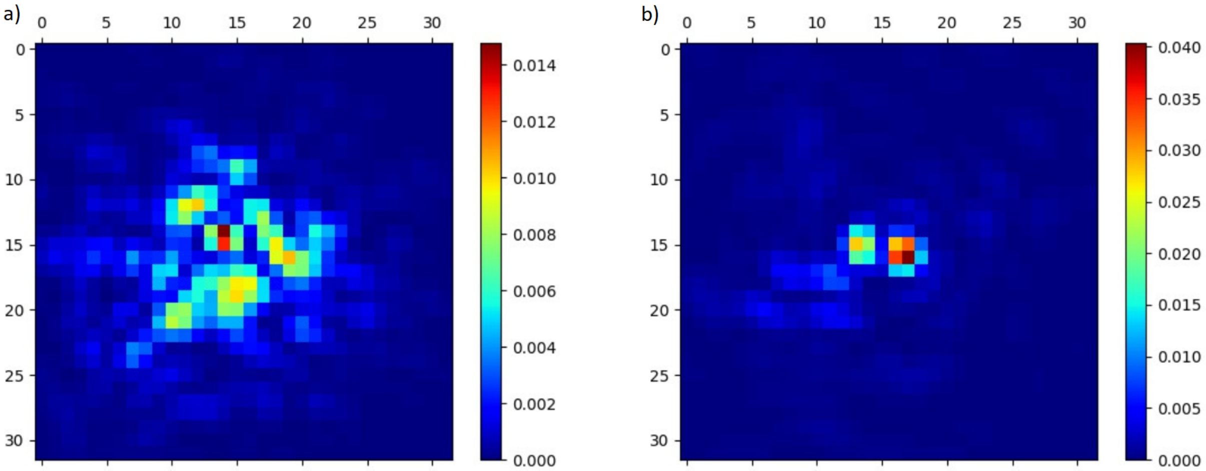

Figure 7.8: a) Simulated PSF to obtain the perturbed intensity profile. **b)** Calculated PSF to be deconvoluted with the perturbed signal which allows to recover the original image of the object.

algorithm.

In Fig 7.3, we compare the theoretical Gaussian profile of the signal before (on the left) and after (on the right) correction using our method.

We start to analyze the CNN component of the global algorithm. The accuracy and cross-entropy loss parameters of the CNN algorithm are crucial for evaluating the training and test of the data sets. Fig 7.4 shows these parameters: on the left panel, we show the classification accuracy and cross-entropy loss for a biased test set. Despite the high magnitude of oscillations for the test data set, both reach stabilization after 400 epochs. As we show in the right panel of Fig 7.4 we obtain a similar result for unbiased test data set. However, this time both stabilize within the same order of magnitude.

We evaluate the performance of the CNN algorithm by comparing the strength of the predicted class and the real one. Figs 7.5 and 7.6 show the multivariate ROC curve and confusion matrix for all r_0 classes.

In Fig 7.5 left panel, we compare the prediction provided by the CNN algorithm with the result of the biased test data set. The area underneath each curve indicates the accuracy for the predictive power of each class of r_0. Ideally, the area underneath each curve should sum to one. We validated the performance of the training data set with a biased and unbiased test data set. The biased data set decreases in accuracy and becomes asymmetric, as seen on the left panel of Fig 7.6.

Furthermore, we notice that by increasing the Rytov parameter (r_0), the CNN algorithm decreases its prediction performance. This effect is more visible by comparing the confusion matrices of the biased and unbiased test sets as seen in Fig 7.6.

We perform a biased analysis to avoid overfitting the results. As shown in the left panel of Fig 7.6, if the training data set is overfitted, even with a Gaussian deviation up to $r_0 = \pm 0.02$ m, the prediction would be incoherent, which is not the case.

Now we shall study the GDO component of the global algorithm. The GDO algorithm uses a parallelization (CUDA Toolkit 11.4 [2]) for each pixel of the 32x32 array image. To optimize the performance time of the algorithm, we use an adjustable step function parameter. Consequently, the algorithm finds the local minimum, at which time the step decreases by order of magnitude. This procedure is used until the algorithm meets the error requirements. The algorithm analyses its performance by comparing the theoretical model of the signal to the corrected one via a local change of the $\mathbb{C}_{xy}$ parameter for each pixel. Thus, the algorithm also provides an MSE study along with each interaction, as seen in Fig 7.7. As identified, the performance of the GDO is more relevant at lower interactions where the order of magnitude for the step function between two points is higher until it reaches stabilization.

From the results of GDO and CNN algorithms (see Equation 7.1), they can recreate the equivalent atmospheric phase-screen. As seen on the left panel of Fig 7.8, the simulated PSF is present, which accounts not only for the atmospheric behaviour but also for the inner optical architecture of the telescope. On the right panel of Fig 7.8, we show the phase-screen profile of an equivalent PSF of the multi-layered turbulent system. By performing a deconvolution of the image with the distorted signal, the original image is recovered as shown on the right panel of Fig 7.2.

We test the viability of our method by computing the MSE between the theoretical and real intensity profiles obtaining $MSE_{\text{original}} = 4.42 \times 10^{-3}$ for the perturbed signal. We found that by comparing to the corrected intensity profile, the MSE ($MSE_{\text{corrected}} = 2.05 \times 10^{-4}$) improves up to an order of magnitude. Thus, such a procedure increases the signal performance from 64.61% up to 91.75% using only a training procedure with a small data set of 2000 images.

Comparing our results to state of the art or recent technological methods for correcting astronomical images, we found that our algorithm achieves the same level of performance as the work of W. Xiong et al. [115]. In this work, the authors use a Zernike coefficients method applied to an experimental setup with a simulated set of wavefront perturbed data. W. Xiong et al. [115] recover the original profile of the non-distorted vortex beam by 93.12% with the use of CNN. Thus, our algorithm reaches the same level of performance as the method proposed in our work.

Nevertheless, there is an essential difference between the two methods: despite achieving the same order of magnitude for the recovery ratio of the intensity profile, the method proposed by W. Xiong et al. [115] only simulates a single phase screen layer with a strength parameter described by $C_n^2 \in [10^{-3}, 10^{-2}]$ for the training set. Although the procedure, providing an experimental view on the telescope's optical components for optical multiplexing, this method does not consider a realistic characterization of the turbulent profile in the simulator as is done in our work.

---

[2] Documentation for the 11.4.1 version available.

We also compare our results with the work of H. Ma et al. [119] which also utilizes the Zernike coefficients method. Both procedures achieve a decrease of the residual wavefront variance up to an order of magnitude. Although H. Ma et al. [119] provides in-depth analysis for the in-focus and out of focus image profile, the simulated data is obtained from only a single phase-screen with strength described by the Strehl ratio ($\frac{D}{r_0} \in [1.0, 15.0]$). Moreover, the data in the training set is described by the atmospherically distorted wavefronts using the Zernike expansion of randomly weighted Karhunen–Loeve functions [128]. Thus, even though our work reaches the same level of performance as in H. Ma et al. [119], our model distinguishes from this work by including a more complete data set for the simulations, once it contains data from the simulated telescope and an improved model for the Earth's atmosphere.

Finally, by comparing our algorithm to the one used on work of S. Lohani et al [114], our algorithm is more sophisticated since its predictions use data sets from the telescope and multi-layer turbulent profile of the earth atmosphere. Indeed in our method, the algorithm uses a more refined model for the telescope that includes information about the obscuration ratios and exposure length intervals. Equally, the fact the algorithm uses a more complete data set of Earth's atmosphere allows for a more efficient key exchange in phase-dependent QKD S/C missions.

7.5 Conclusions

In this section, we propose a new CNN based algorithm to improve the quality of the S/C signal for phase-dependent QKD protocols. This new algorithm uses a realistic multi-layer turbulent profile of the earth atmosphere and a more refined model of the telescope optical system. Moreover, we estimate an equivalent phase-screen for the atmosphere through a global algorithm that combines the CNN and GDO algorithms. Such a procedure allows us to deconvolute the distorted image that recovers almost the original one.

The new method shows promising results towards the optimization and correction of distorted signals due to atmospheric turbulence. For our mission, we found that this method has recovered up to 91.75% of the original intensity profile of the signal in the study as seen in Fig 7.2, decreasing the MSE up to an order of magnitude compared to the distorted image.

Nevertheless, we can improve further this method, by increasing the algorithm's accuracy through an in-depth study of the intrinsic brightness fluctuations of the S/C aperture. We carry out this procedure to have a better dissimilitude between the turbulent behaviour of the image and the actual image of the object.

A context in which such an algorithm can be also of relevant interest is to improve astronomical images coming from deep space. Adapting the algorithm to a satellite observation mission could significantly improve the image quality of faraway objects, helping in that way possible optical systems on board the satellite's telescope. Therefore, changing the objective from recreating an equivalent phase-screen of a turbulent atmospheric profile to a generalized turbulent profile produced by intergalactic cosmic dust.

8

Discussion and main results

8.1 Optical link budget

For this chapter we shall combine all our results in one section, by providing the optical budget for the QKD mission.

In chapter 2 we have defined the most essential requirements and propagated the S/C orbit, determining the propagator errors and the orbit life-cycle.

Resulting into the geometric losses analysis for the sifted key rate and QBER in chapter 3. This chapter considers a Gaussian beam propagation of the signal for each S/C elevation.

In chapter 4 we have added the background perturbation term from the natural and artificial noise to our simulator. Calculating the SNR and the respective loss, comparing all results with ESO-Panaral simulator and experimental data.

Another layer has been added in chapter 5 with the introduction of atmospheric and depolarization losses via a Monte-Carlo propagation. The atmospheric transmissivity calculated in chapter 5 only accounts for the ratio of photons reaching down to the Earth surface.

Parameters	**Description (at zenith)**	**Units**
Signal ratio (S_F) (Fig 4.6)	79.8	$\%$
S/C mean off-pointing ($\frac{2r}{D_R}$) (Fig 6.12)	0.639	-
Geometric loss (Fig 3.4)	28.201 ± 0.001	dB
Atmospheric loss (Fig 5.7)	$1.422^{+0.184}_{-0.374}$	
Atmospheric depolarization loss (Fig 5.3)	$0.284^{+0.142}_{-0.139}$	
Background SNR loss (Fig 4.6)	1.988	
Beam spreading loss (Fig 6.4)	0.003	
Beam wandering loss (Section.6.1.3)	0.015	
Scintillation loss (Fig 7.7)	$[0.000, 3.091]$	
Mean off-pointing loss (Fig 6.11)	1.861	
Basis rotation shift loss [27]	0.265	
Wavefront aberration loss (Fig 7.2)	0.619	
Total loss for entangled based BB84 protocol	$[34.008, 37.099] \pm 0.400$	

Table 8.1: Optical budget for the Quantsat-PT mission at zenith for the 750 km orbit.

In order to account for the dynamic behaviour of the atmosphere, we needed to consider the main turbulent effects which disturb the profile of the signal at the GS. This was performed in chapter 6 by introducing beam wandering, beam spreading and scintillation effects.

Chapter 6 comes as an upgrade to the geometrical analysis performed in chapter 3, to account for the optical off-pointing of the S/C apparatus in a statistical PDTC theory.

For phase dependent protocols, there's an added loss coming from the aberration of the intensity profile of the signal due to turbulence. This added effect which was calculated in chapter 7 was also accounted for in a newly proposed method for signal correction, recovering up to 93.12% of the original wavefront profile. From all these contributions and considering the S/C orbital profile from chapter 2 we can obtain the optical link budget as shown in Table 8.1.

The main uncertainties were calculated based on the orbit misalignment from an ideal case where elevation reaches 90 degrees. For the atmosphere, the presented uncertainties are based on combination of the Monte-Carlo error and the 850 ± 1 nm wavelength band profile. For the total loss, we only propagate the most dominant errors for each contributing term. As scintillation is based on a photon probability distribution a higher and lower range was defined for the losses, this is highly dependent on the intensity profile of the turbulent layers. From Table 8.1, by adding each attenuation term to our simulator, we obtain a loss rate at zenith of $\in [34.008, 37.099] \pm 0.400$ depending on the scintillation conditions.

Mission Concept (chapter 2)

From chapter 2 the satellite orbit was propagated via the GMAT R2020a software as well as the end-of-life orbit using ESA's DRAMA software. Furthermore, propagator errors for the S/C position and velocities were studied by considering different Runge-Kutta methods. Obtaining non-dominant systematic errors up to an order of 10^{-5} km from these results. Also, an end-of-life cycle for the QuantSat-PT mission of 4 and 20 years was estimated for 500 km and 600 km orbits, respectively.

Geometric analysis (chapter 3)

From chapter 3 an in depth analysis is performed to justify the choice for the receiver and transmitter aperture radius as well as for the orbit altitude. Thus, obtaining $D_R = 2.0$ m and $D_T = 0.03$ m and 750km respectively. The atmospheric drag effects in terms of the elevation were discussed, concluding that the S/C oscillatory behaviour is greatly attenuated by three orders of magnitude by changing from a 400km to a 750km orbit.

Background losses (chapter 4)

From chapter 4 based on the data provided from the NASA's/NOAA's SUOMI-NPP mission, we have obtained a natural and artificial backgrounds for the Alqueva region of $B_{Total} = 0.000222 \pm 0.000011$ cdm^{-2} and $B_{Natural} = 0.000051 \pm 0.000005$ respectively. Moreover, thorough an airmass model for the sky-glow in terms of the elevation, for all the photons obtained at the GS only $S_F = 79.8\%$ belonged to our signal at zenith as seen from Fig 4.6. These results were also compared with the data from ESO-Paranal ground site and the SkyCalc simulator achieving similar results for the variance in the sky brightness from the natural and artificial background sources.

Atmospheric losses (chapter 5)

From chapter 5 the atmospheric and depolarization loss was calculated:

For the former, the atmospheric transmissivity coefficient for each elevation was calculated based on the Libradtran package. This transmissivity contains the effects of the atmospheric absorption and Rayleigh scattering. Thus, obtaining at zenith $\tau_{atm} = 0.851^{+0.037}_{-0.018}$ as seen in Fig 5.2. Our work for the atmospheric transmissivity not only follows the results from the MODTRAN 6 software but also follows the theoretical fit from the work of Daniele Dequal et al. [29].

For the latter, a Monte-Carlo method was used propagating each linearly or horizontally polarized photon trough its deformed path. Moreover, we have obtained a $DoP(\%) = 96.1 \pm 3.9\%$ which means that depolarization can disturb the signal within a range of $[0.2, 8.1]\%$ from this effect. The asymmetry of the Stokes parameters were also studied obtaining an elevation dependence between ΔQ and ΔI of $\Delta Q = 0.97126\Delta I - 0.00002$. All results are in accordance with the work of M.Toyoshima et al [90], obtaining similar results.

Lastly, in section.5.4.2 we have also performed the E91 protocol analysis. There have assumed that if a photon does not reach the GS it shall not be considered for the CHSH test. Instead, a background photon will be considered in the expected arrival time of the signal. To compute the E91 protocol a quantum gates circuit was simulated in order to perform statistically the CHSH test, thus, obtaining a correlation factor of $S \in [-2.63 \pm 0.02, -1.91 \pm 0.03]$. There, the E91 protocol is only valid between the active time of $\in [46, 321]$ s for the mission.

Turbulence losses (chapter 6)

From chapter 6 by performing the turbulent analysis for the scintillation, beam wandering and spreading effects. We understood that only scintillation plays a key role for the decrease in quality of the signal for the Quantsat-PT mission, decreasing it up to 3.091 dB (30% of the signal) with a log-normal distribution.

PDTC

We also computed the mean off-pointing profile of the satellite, considering the off pointing accuracy of the S/C telescope, reaching at zenith to a 0.639 m deviation from the center of the GS as seen from Table 8.1 and Fig 6.12. This profile follows the results from the QUARC mission [27] as well as from the work of Daniele Dequal et al. [29] allowing to characterize statistically the mean pointing offset.

A new CNN method for turbulence correction (chapter 7)

For phase-dependent protocols an additional loss is present which accordingly to our simulation and the work of W. Xiong et al. [115] can perturb the signal's wavefront down to 64.61% compared to the original one. By implementing the new CNN intensity profile turbulence correction method presented in chapter 7, we were able to recover up to 93.12% of the original wave front profile, with low quantities of training data-sets (2000 32x32 images) for the signal profile. Thus, allowing us to decrease the $MSE_{\text{original}} = 4.42 \times 10^{-3}$ for the perturbed signal down to $MSE_{\text{corrected}} = 2.05 \times 10^{-4}$ improving the MSE up to an order of magnitude.

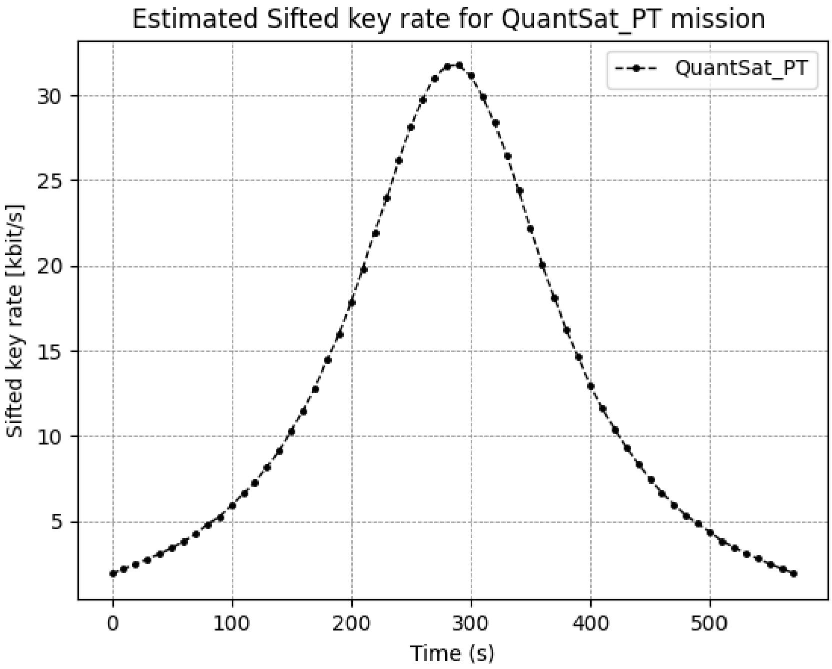

Figure 8.1: Sifted key rate in terms of the S/C elevation for the QuantSat-PT mission considering all losses from Table 8.1.

8.2 QBER and sifted key rate

For the BB84 protocol, to obtain the key rate, we use the overall loss rate presented at Table 8.1 for each S/C elevation. Hence, allowing to obtain Fig 8.1. Fig 8.1 shows that the key rate for the mission reaches up to 32.1 kbit/s considering a MPN $= 0.5$. The attenuation effects greatly decrease at high turbulent zenith angles the overall signal performance reaching down to 3 kbit/s at $\theta_{zen} = 80$ deg.

For QBER, compared to Fig 5.8 we also have added all the losses presented in Table 8.1 obtaining Fig 8.2. At low zenith angles up to $\theta_{zen} = 60$ deg the quality of the BB84 protocol remains practically the same within a range of QBER $\in [3.8, 5.1]\%$. When in high turbulent environment the QBER can reach above the 11%. Hence, from there the protocol looses its validity, allowing for an eavesdropper to obtain relevant information without being noticed. Our active time for the mission shortens down to $\in [31, 540]$ s as seen from Fig 8.2.

This result is validated according to the work of Carlo Liorni et al. [28], J-P Bourgoin et al. [24] and Daniele Dequal et al. [29]. Where considering similar S/C trajectory profiles and initial parameters we obtain results down to a 2 dB error. Carlo Liorni et al. [28] considers an altitude of 500 km, with a $w_0 = 0.05$ m and $D_R = 1.0$ m. The author's work achieves for Cubesats a QBER $= 3\%$ at low zenith

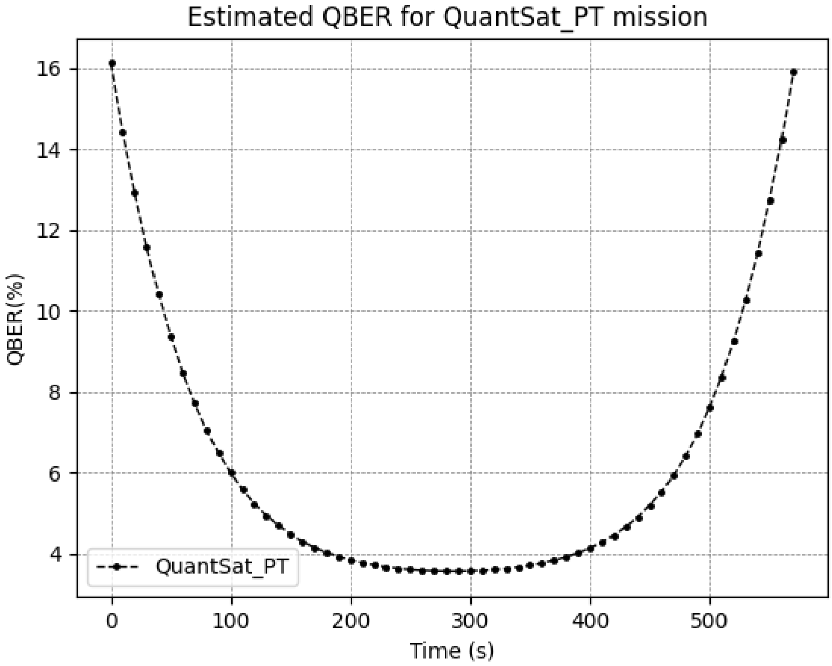

Figure 8.2: QBER in terms of the S/C elevation for the QuantSat-PT mission considering all losses from Table 8.1.

angles going up to QBER $= 14\%$ at zenith angles above $\theta_{zen} = 75\%$. Our simulator reaches the same QBER profile being within the uncertainty range for the total losses.

We also compared our simulator with the work of Bourgoin et al. [24] which considers a 600km orbit, with the same parameters as defined previously from the work of Carlo Liorni et al. The author's achieve a QBER below 11% between zenith angles of $\theta_{zen} \in [0, 70]$ deg. Once again, considering similar geometrical parameters our results reach the same order of magnitude as their work.

To verify if our end results are in compliance with the simulator requirements we compare them with Table 2.1. For the mission we have considered a FoV $= 7.14 \times 10^{-05}$ following TR-01. CR-01 requirement for the BB84 protocol and E91 protocol is only followed during active times of $\in [31, 540]$ s and $\in [46, 321]$ s respectively. Requirement CR-02 is followed accordingly to the orbit end of life cycle (30 years), being purely dependent on the hardware life cycle. CR-03 is also followed considering the choice of the geometrical parameters from chapter 3. Requirements CR [04,05] are also followed by choosing the ground-site at (Latitude, Longitude) = (38.21585 , -7.58783) and by considering a sun-synchronous orbit from chapter 2.

In this work, a more accurate turbulent analysis was performed for the QKD communications for the BB84 and E91 protocols. Also, a more detailed numerical and theoretical analysis for the photon depolarization was also computed. Moreover, we also have introduced some new outside of the box methods (such in chapter 7) contributing greatly for a more detailed analysis and key performance in the optical communications and QKD fields. This work not only contributes as a viable simulator for the QuantSat-PT mission, but also, is as step in the right direction for a more realistic simulation of future satellite QKD missions.

9

Conclusions and future work

This work contributes to solve one of the major problems in QKD space missions which is the precise consideration of atmospheric losses on the signal. The simulator was developed as part of the QuantSat-PT project, that aims to perform the first ever Portuguese QKD space mission on a 2U Cubesat.

In this thesis we have computed the sifted key as well as the QBER for the BB84 protocol which reach up to 32.1 kbit/s and 4% at zenith respectively for a 750 km orbit. For the E91 protocol a similar analysis was performed, however this time, the CHSH test was studied. By creating a quantum circuit for the E91 protocol, we have obtained a correlation factor of $S \in [-2.63 \pm 0.02, -1.91 \pm 0.03]$ for the mission, considering the depolarization and SNR terms. Moreover, in-depth analysis for the turbulent behaviour was performed as well as the depolarization ratio on our signal with the study of the Stokes parameters. A statistical analysis was also proposed for our mission, which considered the mean off-pointing behaviour of the satellite in a turbulent environment. Furthermore, the photon propagation along the atmosphere was simulated with Monte Carlo allowing to obtain the atmospheric transmissivity considering the absorption and Rayleigh scattering effects. At zenith we have obtained a transmissivity of $\tau_{atm} = 0.851^{+0.037}_{-0.018}$. For phase-dependent protocols a new corrective method for disturbed intensity profiles is proposed with the use of a closed feedback CNN method which recovers the signal up to 93.12%.

To improve even further the simulator, we must take into account the hardware behaviour of the optical payload. Thus, by performing the hardware in loop testing we could create a more realistic model for the signal's intensity profile. This would also allow for a more robust modelling for the optical and quantum efficiencies for each optical segment which lead to a more realistic QKD performance.

In order to improve the accuracy of the night sky background behaviour, it is essential to perform a local set of measurements for the brightness of night sky in the Alqueva region in order to realistically calibrate the simulator considering the mean natural and artificial background noise.

For the algorithm presented in chapter 7, we can increase the algorithm's accuracy by studying the intrinsic brightness fluctuations of the signal's source. We carry this out, in order to better distinguish the turbulent and intrinsic behaviour of the source. This algorithm, not only is pivotal for phase-dependent protocols but can also be applied for extra-planetary observation missions, which could significantly improve the image quality of faraway objects, helping in that way possible optical systems on board the satellite's telescope.

Bibliography

[1] S.-K. Liao, W.-Q. Cai, W.-Y. Liu, L. Zhang, Y. Li, J.-G. Ren, J. Yin, Q. Shen, Y. Cao, Z.-P. Li, F.-Z. Li, X.-W. Chen, L.-H. Sun, J.-J. Jia, J.-C. Wu, X.-J. Jiang, J.-F. Wang, Y.-M. Huang, Q. Wang, Y.-L. Zhou, L. Deng, T. Xi, L. Ma, T. Hu, Q. Zhang, Y.-A. Chen, N.-L. Liu, X.-B. Wang, Z.-C. Zhu, C.-Y. Lu, R. Shu, C.-Z. Peng, J.-Y. Wang, and J.-W. Pan, "Satellite-to-ground quantum key distribution," *Nature*, vol. 549, no. 7670, pp. 43–47, Sep 2017. [Online]. Available: https://doi.org/10.1038/nature23655

[2] H. Takenaka, A. Carrasco-Casado, M. Fujiwara, M. Kitamura, M. Sasaki, and M. Toyoshima, "Satellite-to-ground quantum-limited communication using a 50-kg-class microsatellite," *Nature Photonics*, vol. 11, no. 8, pp. 502–508, Aug 2017. [Online]. Available: https://doi.org/10.1038/nphoton.2017.107

[3] "Standard 2u cubesat components," https://alen.space/basic-guide-nanosatellites/, accessed: 2021-12-10.

[4] B. Rödiger, C. Menninger, C. Fuchs, L. Grillmayer, S. Arnold, C. Rochow, P. Wertz, and C. Schmidt, "High data-rate optical communication payload for CubeSats," in *Laser Communication and Propagation through the Atmosphere and Oceans IX*, J. A. Anguita, J. P. Bos, and D. T. Wayne, Eds., vol. 11506, International Society for Optics and Photonics. SPIE, 2020, pp. 12 – 24. [Online]. Available: https://doi.org/10.1117/12.2567035

[5] "Source for the image PIXL-1 payload," https://www.dlr.de/content/en/articles/news/2021/01/20210124_pioneering-launch-compact-satellite-with-smallest-laser-terminal.html, accessed: 2021-09-03.

[6] J. McIntire, D. Moyer, T. Chang, H. Oudrari, and X. Xiong, "Pre-launch JPSS-2 VIIRS response versus scan angle characterization," *Remote Sensing, doi:10.3390/rs9121300*, 2017.

[7] F. Falchi, P. Cinzano, D. Duriscoe, C. C. M. Kyba, C. D. Elvidge, K. Baugh, B. A. Portnov, N. A. Rybnikova, and R. Furgoni, "The new world atlas of artificial night sky

brightness," *Science Advances*, vol. 2, no. 6, p. e1600377, 2016. [Online]. Available: https://www.science.org/doi/abs/10.1126/sciadv.1600377

[8] K. A. Pickering, "The Southern Limits of the Ancient Star Catalog and the Commentary of Hipparchos," *DIO*, vol. 12, pp. 3–27, Sep. 2002.

[9] C. C. M. Kyba, T. Ruhtz, J. Fischer, and F. Hölker, "Lunar skylight polarization signal polluted by urban lighting," *Journal of Geophysical Research: Atmospheres*, vol. 116, no. D24, 2011. [Online]. Available: https://agupubs.onlinelibrary.wiley.com/doi/abs/10.1029/2011JD016698

[10] S. Hallgren, A. Smith, and F. Song, "Classical cryptographic protocols in a quantum world," *International Journal of Quantum Information*, vol. 13, no. 04, p. 1550028, Jun 2015. [Online]. Available: http://dx.doi.org/10.1142/S0219749915500288

[11] R. L. Rivest, A. Shamir, and L. Adleman, "A method for obtaining digital signatures and public-key cryptosystems," *Commun. ACM*, vol. 21, no. 2, p. 120–126, Feb. 1978. [Online]. Available: https://doi.org/10.1145/359340.359342

[12] M. A. Nielsen and I. L. Chuang, *Quantum computation*. Cambridge University Press, 2010.

[13] F. Arute, K. Arya, R. Babbush, D. Bacon, J. C. Bardin, R. Barends, R. Biswas, S. Boixo, F. G. S. L. Brandao, D. A. Buell, and et al., "Quantum supremacy using a programmable superconducting processor," *Nature*, vol. 574, no. 7779, p. 505–510, Oct 2019. [Online]. Available: http://dx.doi.org/10.1038/s41586-019-1666-5

[14] P. Jurcevic, A. Javadi-Abhari, L. S. Bishop, I. Lauer, D. F. Bogorin, M. Brink, L. Capelluto, O. Günlük, T. Itoko, N. Kanazawa, A. Kandala, G. A. Keefe, K. Krsulich, W. Landers, E. P. Lewandowski, D. T. McClure, G. Nannicini, A. Narasgond, H. M. Nayfeh, E. Pritchett, M. B. Rothwell, S. Srinivasan, N. Sundaresan, C. Wang, K. X. Wei, C. J. Wood, J.-B. Yau, E. J. Zhang, O. E. Dial, J. M. Chow, and J. M. Gambetta, "Demonstration of quantum volume 64 on a superconducting quantum computing system," 2020.

[15] Y. Wu, W.-S. Bao, S. Cao, F. Chen, M.-C. Chen, X. Chen, T.-H. Chung, H. Deng, Y. Du, D. Fan, M. Gong, C. Guo, C. Guo, S. Guo, L. Han, L. Hong, H.-L. Huang, Y.-H. Huo, L. Li, N. Li, S. Li, Y. Li, F. Liang, C. Lin, J. Lin, H. Qian, D. Qiao, H. Rong, H. Su, L. Sun, L. Wang, S. Wang, D. Wu, Y. Xu, K. Yan, W. Yang, Y. Yang, Y. Ye, J. Yin, C. Ying, J. Yu, C. Zha, C. Zhang, H. Zhang, K. Zhang, Y. Zhang, H. Zhao, Y. Zhao, L. Zhou, Q. Zhu, C.-Y. Lu, C.-Z. Peng, X. Zhu, and J.-W. Pan, "Strong quantum computational advantage using a superconducting quantum processor," 2021.

[16] "First quantum computer to pack 100 qubits enters crowded race," https://doi.org/10.1038/d41586-021-03476-5, accessed: 2021-12-10.

[17] D. J. Bernstein and T. Lange, “Post-quantum cryptography,” *Nature*, vol. 549, no. 7671, pp. 188–194, Sep 2017. [Online]. Available: https://doi.org/10.1038/nature23461

[18] T. Bi Irie guy cedric, “A comparative study on aes 128 bit and aes 256 bit,” *INTERNATIONAL JOURNAL OF COMPUTER SCIENCES AND ENGINEERING*, vol. volume 6, pp. 30–33, 09 2018.

[19] E. Diamanti and A. Leverrier, “Distributing secret keys with quantum continuous variables: Principle, security and implementations,” *Entropy*, vol. 17, no. 9, pp. 6072–6092, 2015. [Online]. Available: https://www.mdpi.com/1099-4300/17/9/6072

[20] E. Diamanti, H.-K. Lo, B. Qi, and Z. Yuan, “Practical challenges in quantum key distribution,” *npj Quantum Information*, vol. 2, no. 1, Nov 2016. [Online]. Available: http://dx.doi.org/10.1038/npjqi.2016.25

[21] N. Gisin, G. Ribordy, W. Tittel, and H. Zbinden, “Quantum cryptography,” *Rev. Mod. Phys.*, vol. 74, pp. 145–195, Mar 2002. [Online]. Available: https://link.aps.org/doi/10.1103/RevModPhys.74.145

[22] R. Horodecki, P. Horodecki, M. Horodecki, and K. Horodecki, “Quantum entanglement,” *Rev. Mod. Phys.*, vol. 81, pp. 865–942, Jun 2009. [Online]. Available: https://link.aps.org/doi/10.1103/RevModPhys.81.865

[23] T.-S. Lin, I.-M. Tsai, H.-W. Wang, and S.-Y. Kuo, “Quantum authentication and secure communication protocols,” in *2006 Sixth IEEE Conference on Nanotechnology*, vol. 2, 2006, pp. 863–866.

[24] J.-P. Bourgoin, E. Meyer-Scott, B. L. Higgins, B. Helou, C. Erven, H. Hübel, B. Kumar, D. Hudson, I. D'Souza, R. Girard, R. Laflamme, and T. Jennewein, “A comprehensive design and performance analysis of low earth orbit satellite quantum communication,” *New Journal of Physics*, vol. 15, no. 2, p. 023006, feb 2013. [Online]. Available: https://doi.org/10.1088/1367-2630/15/2/023006

[25] S. Pirandola, U. L. Andersen, L. Banchi, M. Berta, D. Bunandar, R. Colbeck, D. Englund, T. Gehring, C. Lupo, C. Ottaviani, and et al., “Advances in quantum cryptography,” *Advances in Optics and Photonics*, vol. 12, no. 4, p. 1012, Dec 2020. [Online]. Available: http://dx.doi.org/10.1364/AOP.361502

[26] J. Yin, Y.-H. Li, S.-K. Liao, M. Yang, Y. Cao, L. Zhang, J.-G. Ren, W.-Q. Cai, W.-Y. Liu, S.-L. Li, R. Shu, Y.-M. Huang, L. Deng, L. Li, Q. Zhang, N.-L. Liu, Y.-A. Chen, C.-Y. Lu, X.-B. Wang, F. Xu, J.-Y. Wang, C.-Z. Peng, A. K. Ekert, and J.-W. Pan, “Entanglement-based secure quantum cryptography over 1,120 kilometres,” *Nature*, vol. 582, no. 7813, pp. 501–505, Jun 2020. [Online]. Available: https://doi.org/10.1038/s41586-020-2401-y

[27] L. Mazzarella, C. Lowe, D. Lowndes, S. K. Joshi, S. Greenland, D. McNeil, C. Mercury, M. Macdonald, J. Rarity, and D. K. L. Oi, “Quarc: Quantum research cubesat—a

constellation for quantum communication," *Cryptography*, vol. 4, no. 1, 2020. [Online]. Available: https://www.mdpi.com/2410-387X/4/1/7

[28] C. Liorni, H. Kampermann, and D. Bruß, "Satellite-based links for quantum key distribution: beam effects and weather dependence," *New Journal of Physics*, vol. 21, no. 9, p. 093055, sep 2019. [Online]. Available: https://doi.org/10.1088/1367-2630/ab41a2

[29] D. Dequal, L. Trigo Vidarte, V. Roman Rodriguez, G. Vallone, P. Villoresi, A. Leverrier, and E. Diamanti, "Feasibility of satellite-to-ground continuous-variable quantum key distribution," *npj Quantum Information*, vol. 7, no. 1, p. 3, Jan 2021. [Online]. Available: https://doi.org/10.1038/s41534-020-00336-4

[30] H. Kaushal and G. Kaddoum, "Optical communication in space: Challenges and mitigation techniques," *IEEE Communications Surveys Tutorials*, vol. 19, no. 1, pp. 57–96, 2017.

[31] F. Shen and A. Wang, "Fast-fourier-transform based numerical integration method for the rayleigh-sommerfeld diffraction formula," *Applied optics*, vol. 45, pp. 1102–10, 03 2006.

[32] A. Berk, P. Conforti, R. Kennett, T. Perkins, F. Hawes, and J. van den Bosch, "Modtran® 6: A major upgrade of the modtran® radiative transfer code," in *2014 6th Workshop on Hyperspectral Image and Signal Processing: Evolution in Remote Sensing (WHISPERS)*, 2014, pp. 1–4.

[33] J. D. Liddle, A. P. Holt, S. J. Jason, K. A. O'Donnell, and E. J. Stevens, "Space science with cubesats and nanosatellites," *Nature Astronomy*, vol. 4, no. 11, pp. 1026–1030, Nov 2020. [Online]. Available: https://doi.org/10.1038/s41550-020-01247-2

[34] A. Ampatzoglou and V. Kostopoulos, "Design, analysis, optimization, manufacturing, and testing of a 2u cubesat," *International Journal of Aerospace Engineering*, vol. 2018, p. 9724263, Jun 2018. [Online]. Available: https://doi.org/10.1155/2018/9724263

[35] "Description of ECSS-E-ST-40C," https://ecss.nl/standard/ecss-e-st-40c-software-general-requirements/, accessed: 2021-09-03.

[36] M. Jones, E. Gomez, A. Mantineo, and U. Mortensen, "Introducing ecss software-engineering standards within esa: Practical approaches for space- and ground-segment software," 2002.

[37] "Ieee standard for application of systems engineering on defense programs," *IEEE Std 15288.1-2014*, pp. 1–65, 2015.

[38] Y. Zhou, Z. Wang, A. Rasmita, S. Kim, A. Berhane, Z. Bodrog, G. Adamo, A. Gali, I. Aharonovich, and W. bo Gao, "Room-temperature solid state quantum emitters in the telecom range," 2017.

[39] R. Bedington, J. M. Arrazola, and A. Ling, “Progress in satellite quantum key distribution,” *npj Quantum Information*, vol. 3, no. 1, p. 30, Aug 2017. [Online]. Available: https://doi.org/10.1038/s41534-017-0031-5

[40] A. Alkholidi and K. S. Altowij, “Free space optical communications — theory and practices,” 2014.

[41] E. Clements, R. Aniceto, D. Barnes, D. Caplan, J. Clark, I. del Portillo, C. Haughwout, M. Khatsenko, R. Kingsbury, M. Lee, R. Morgan, J. C. Twichell, K. Riesing, H. Yoon, C. Ziegler, and K. Cahoy, “Nanosatellite optical downlink experiment: design, simulation, and prototyping,” *Optical Engineering*, vol. 55, no. 11, pp. 1 – 18, 2016. [Online]. Available: https://doi.org/10.1117/1.OE.55.11.111610

[42] S. Hughes, R. Qureshi, S. Cooley, and J. Parker, “Verification and validation of the general mission analysis tool (gmat),” 08 2014.

[43] J. H. Verner, “Some runge-kutta formula pairs,” *SIAM Journal on Numerical Analysis*, vol. 28, no. 2, pp. 496–511, 2021/09/03/ 1991, full publication date: Apr., 1991. [Online]. Available: http://www.jstor.org/stable/2157825

[44] “Description of Earth centered equator inertial frame of reference (J2000),” https://gssc.esa.int/navipedia/index.php/Reference_Systems_and_Frames, accessed: 2021-09-03.

[45] V. Braun, Q. Funke, S. Lemmens, and S. Sanvido, “Drama 3.0 - upgrade of esa’s debris risk assessment and mitigation analysis tool suite,” *Journal of Space Safety Engineering*, vol. 7, no. 3, pp. 206–212, 2020, space Debris: The State of Art. [Online]. Available: https://www.sciencedirect.com/science/article/pii/S2468896720300847

[46] “Description of ISO 27852:2016,” https://www.iso.org/standard/44388.html, accessed: 2021-09-03.

[47] V. Braun, N. Sánchez-Ortiz, J. Gelhaus, C. Kebschull, S. Flegel, M. Moeckel, C. Wiedemann, H. Krag, and P. Vörsmann, “Upgrade of the esa drama oscar tool: Analysis of disposal strategies considering current standards for future solar and geomagnetic activity,” 04 2013.

[48] S. Cakaj, B. Kamo, V. Kolici, and O. Shurdi, “The range and horizon plane simulation for ground stations of low earth orbiting (leo) satellites,” *IJCNS*, vol. 4, pp. 585–589, 01 2011.

[49] A. Jäggi, R. Dach, O. Montenbruck, U. Hugentobler, H. Bock, and G. Beutler, “Phase center modeling for leo gps receiver antennas and its impact on precise orbit determination,” *Journal of Geodesy*, vol. 83, no. 12, p. 1145, Jul 2009. [Online]. Available: https://doi.org/10.1007/s00190-009-0333-2

[50] V. Nourrit, J.-L. de Bougrenet de la Tocnaye, and P. Chanclou, “Propagation and diffraction of truncated gaussian beams,” *J. Opt. Soc. Am. A*, vol. 18, no. 3, pp. 546–556, Mar 2001. [Online]. Available: http://josaa.osa.org/abstract.cfm?URI=josaa-18-3-546

[51] C. Zhang, A. Tello, U. Zanforlin, G. S. Buller, and R. J. Donaldson, “Link loss analysis for a satellite quantum communication down-link,” in *Emerging Imaging and Sensing Technologies for Security and Defence V; and Advanced Manufacturing Technologies for Micro- and Nanosystems in Security and Defence III*, G. S. Buller, R. C. Hollins, R. A. Lamb, M. Laurenzis, A. Camposeo, M. Farsari, L. Persano, and L. E. Busse, Eds., vol. 11540, International Society for Optics and Photonics. SPIE, 2020, pp. 18 – 29. [Online]. Available: https://doi.org/10.1117/12.2573489

[52] J. C. Denton, D. D. Hodson, R. G. Cobb, L. O. Mailloux, M. R. Grimaila, and G. Baumgartner, “A model to estimate performance of space-based quantum communication protocols including quantum key distribution systems,” *The Journal of Defense Modeling and Simulation*, vol. 16, no. 1, pp. 5–13, 2019. [Online]. Available: https://doi.org/10.1177/1548512916684562

[53] C. P. Maria Petrou, *Image Processing: The Fundamentals*. Wiley; 2nd edition, 2010.

[54] C. Siemes, J. de Teixeira da Encarnação, E. Doornbos, J. van den IJssel, J. Kraus, R. Pereštý, L. Grunwaldt, G. Apelbaum, J. Flury, and P. E. Holmdahl Olsen, “Swarm accelerometer data processing from raw accelerations to thermospheric neutral densities,” *Earth, Planets and Space*, vol. 68, no. 1, p. 92, May 2016. [Online]. Available: https://doi.org/10.1186/s40623-016-0474-5

[55] D. Mostaza Prieto, B. P. Graziano, and P. C. Roberts, “Spacecraft drag modelling,” *Progress in Aerospace Sciences*, vol. 64, pp. 56–65, 2014. [Online]. Available: https://www.sciencedirect.com/science/article/pii/S0376042113000754

[56] D. Herdiwijaya, R. Satyaningsih, Luthfiandari, H. Prastyo, E. Arumaningtyas, M. Sulaeman, A. Setiawan, and Y. Yulianti, “Measurements of sky brightness at bosscha observatory, indonesia,” *Heliyon*, vol. 6, no. 8, p. e04635, 2020. [Online]. Available: https://www.sciencedirect.com/science/article/pii/S2405844020314791

[57] S. Warren, “Optical properties of ice and snow,” *Philosophical transactions. Series A, Mathematical, physical, and engineering sciences*, vol. 377, 06 2019.

[58] Noll, S., Kausch, W., Barden, M., Jones, A. M., Szyszka, C., Kimeswenger, S., and Vinther, J., “An atmospheric radiation model for cerro paranal - i. the optical spectral range,” *A&A*, vol. 543, p. A92, 2012. [Online]. Available: https://doi.org/10.1051/0004-6361/201219040

[59] Patat, F., “Appendix c; ubvri night sky brightness during sunspot maximum at eso-paranal ***,” *A&A*, vol. 400, no. 3, pp. 1183–1198, 2003. [Online]. Available: https://doi.org/10.1051/0004-6361:20030030

[60] Patat, F., Moehler, S., O´Brien, K., Pompei, E., Bensby, T., Carraro, G., de Ugarte Postigo, A., Fox, A., Gavignaud, I., James, G., Korhonen, H., Ledoux, C., Randall, S., Sana, H., Smoker, J., Stefl, S., and Szeifert, T., “Optical atmospheric extinction over cerro paranal,” *A&A*, vol. 527, p. A91, 2011. [Online]. Available: https://doi.org/10.1051/0004-6361/201015537

[61] S. F. Sánchez, U. Thiele, J. Aceituno, D. Cristobal, J. Perea, and J. Alves, “The night sky at the calar alto observatory ii: The sky at the near-infrared,” *Publications of the Astronomical Society of the Pacific*, vol. 120, no. 873, p. 1244–1254, Nov 2008. [Online]. Available: http://dx.doi.org/10.1086/593981

[62] Jones, A., Noll, S., Kausch, W., Szyszka, C., and Kimeswenger, S., “An advanced scattered moonlight model for cerro paranal,” *A&A*, vol. 560, p. A91, 2013. [Online]. Available: https://doi.org/10.1051/0004-6361/201322433

[63] M. Er-long, H. Zheng-fu, G. Shun-sheng, Z. Tao, D. Da-sheng, and G. Guang-can, “Background noise of satellite-to-ground quantum key distribution,” *New Journal of Physics*, vol. 7, pp. 215–215, oct 2005. [Online]. Available: https://doi.org/10.1088/1367-2630/7/1/215

[64] A. W. Elshaari, I. E. Zadeh, A. Fognini, M. E. Reimer, D. Dalacu, P. J. Poole, V. Zwiller, and K. D. Jöns, “On-chip single photon filtering and multiplexing in hybrid quantum photonic circuits,” *Nature Communications*, vol. 8, no. 1, p. 379, Aug 2017. [Online]. Available: https://doi.org/10.1038/s41467-017-00486-8

[65] Q. Yang, L. Tan, and J. Ma, “Analysis of doppler-effect on satellite constellations with wavelength division multiplexing architectures,” *Chin. Opt. Lett.*, vol. 7, no. 1, pp. 19–22, Jan 2009. [Online]. Available: http://col.osa.org/abstract.cfm?URI=col-7-1-19

[66] ——, “Doppler characterization of laser inter-satellite links for optical leo satellite constellations,” *Optics Communications - OPT COMMUN*, vol. 282, pp. 3547–3552, 09 2009.

[67] T. Kupko, M. von Helversen, L. Rickert, J.-H. Schulze, A. Strittmatter, M. Gschrey, S. Rodt, S. Reitzenstein, and T. Heindel, “Tools for the performance optimization of single-photon quantum key distribution,” *npj Quantum Information*, vol. 6, no. 1, p. 29, Mar 2020. [Online]. Available: https://doi.org/10.1038/s41534-020-0262-8

[68] O. Lee and T. Vergoossen, “An updated analysis of satellite quantum-key distribution missions,” 2019.

[69] Z. Chen, B. Liu, and G. Guo, “Adaptive single photon detection under fluctuating background noise,” *Opt. Express*, vol. 28, no. 20, pp. 30 199–30 209, Sep 2020. [Online]. Available: http://www.opticsexpress.org/abstract.cfm?URI=oe-28-20-30199

[70] S. Bogdanov, M. Y. Shalaginov, A. Boltasseva, and V. M. Shalaev, “Material platforms for integrated quantum photonics,” *Opt. Mater. Express*, vol. 7, no. 1, pp. 111–132, Jan 2017. [Online]. Available: http://www.osapublishing.org/ome/abstract.cfm?URI=ome-7-1-111

[71] C. M. Natarajan, M. G. Tanner, and R. H. Hadfield, “Superconducting nanowire single-photon detectors: physics and applications,” *Superconductor Science and Technology*, vol. 25, no. 6, p. 063001, apr 2012. [Online]. Available: https://doi.org/10.1088/0953-2048/25/6/063001

[72] J. J. Foster, J. D. Kirwan, B. el Jundi, J. Smolka, L. Khaldy, E. Baird, M. J. Byrne, D.-E. Nilsson, S. Johnsen, and M. Dacke, “Orienting to polarized light at night – matching lunar skylight to performance in a nocturnal beetle,” *Journal of Experimental Biology*, vol. 222, no. 2, 01 2019, jeb188532. [Online]. Available: https://doi.org/10.1242/jeb.188532

[73] C. Benn and S. Ellison, “Brightness of the night sky over la palma,” *New Astronomy Reviews*, vol. 42, no. 6-8, p. 503–507, Nov 1998. [Online]. Available: http://dx.doi.org/10.1016/S1387-6473(98)00062-1

[74] C. Emde, R. Buras-Schnell, A. Kylling, B. Mayer, J. Gasteiger, U. Hamann, J. Kylling, B. Richter, C. Pause, T. Dowling, and L. Bugliaro, “The libradtran software package for radiative transfer calculations (version 2.0.1),” *Geoscientific Model Development*, vol. 9, no. 5, pp. 1647–1672, 2016. [Online]. Available: https://gmd.copernicus.org/articles/9/1647/2016/

[75] B. Mayer and A. Kylling, “Technical note: The libradtran software package for radiative transfer calculations - description and examples of use,” *Atmospheric Chemistry and Physics*, vol. 5, pp. 1855–1877, 03 2005.

[76] Z. Lin, S. Stamnes, Z. Jin, I. Laszlo, S.-C. Tsay, W. Wiscombe, and K. Stamnes, “Improved discrete ordinate solutions in the presence of an anisotropically reflecting lower boundary: Upgrades of the disort computational tool,” *Journal of Quantitative Spectroscopy and Radiative Transfer*, vol. 157, pp. 119–134, 2015. [Online]. Available: https://www.sciencedirect.com/science/article/pii/S0022407315000679

[77] S.-C. Tsay, K. Stamnes, W. Wiscombe, I. Laszlo, and F. Einaudi, “General purpose fortran program for discrete-ordinate-method radiative transfer in scattering and emitting layered media: An update of disort,” 02 2000.

[78] I. Laszlo, K. Stamnes, W. J. Wiscombe, and S.-C. Tsay, *The Discrete Ordinate Algorithm, DISORT for Radiative Transfer*. Berlin, Heidelberg: Springer Berlin Heidelberg, 2016, pp. 3–65. [Online]. Available: https://doi.org/10.1007/978-3-662-49538-4_1

[79] C. Emde, V. Barlakas, C. Cornet, F. Evans, S. Korkin, Y. Ota, L. C. Labonnote, A. Lyapustin, A. Macke, B. Mayer, and et al., "Iprt polarized radiative transfer model intercomparison project – phase a," *Journal of Quantitative Spectroscopy and Radiative Transfer*, vol. 164, p. 8–36, Oct 2015. [Online]. Available: http://dx.doi.org/10.1016/j.jqsrt.2015.05.007

[80] B. Mayer, S. W. Hoch, and C. D. Whiteman, "Validating the mystic three-dimensional radiative transfer model with observations from the complex topography of arizona's meteor crater," *Atmospheric Chemistry and Physics*, vol. 10, no. 18, pp. 8685–8696, 2010. [Online]. Available: https://acp.copernicus.org/articles/10/8685/2010/

[81] G. Stephens, D. O'Brien, P. Webster, P. Pilewskie, S. Kato, and J.-L. Li, "The albedo of earth," *Reviews of Geophysics*, vol. 53, 03 2015.

[82] A. J. Kantor and A. E. Cole, "Mid-latitude atmospheres, winter and summer," *Geofisica pura e applicata*, vol. 53, no. 1, pp. 171–188, Sep 1962. [Online]. Available: https://doi.org/10.1007/BF02007120

[83] M. Hess, P. Koepke, and I. Schult, "Optical properties of aerosols and clouds: The software package opac," *Bulletin of the American Meteorological Society*, vol. 79, pp. 831–844, 05 1998.

[84] M. Lefèvre, M. Schroedter-Homscheidt, and A. Arola, "Improving the mcclear model estimating the downwelling solar radiation at ground level in cloud-free conditions – mcclear-v3," *Meteorologische Zeitschrift*, vol. 28, 03 2019.

[85] S. Han, H. Bian, Y. Zhang, J. Wu, Y. Wang, X. Tie, Y. Li, X. Li, and Q. Yao, "Effect of aerosols on visibility and radiation in spring 2009 in tianjin, china," vol. 12, no. 2, pp. 211–217, 2012. [Online]. Available: https://doi.org/10.4209%2Faaqr.2011.05.0073

[86] J. Gasteiger, C. Emde, B. Mayer, R. Buras, S. A. Buehler, and O. Lemke, "Representative wavelengths absorption parameterization applied to satellite channels and spectral bands," , vol. 148, pp. 99–115, Nov. 2014.

[87] D. Jackèl and B. Walter, "Modeling and rendering of the atmosphere using mie-scattering," *Computer Graphics Forum*, vol. 16, no. 4, pp. 201–210, 1997. [Online]. Available: https://onlinelibrary.wiley.com/doi/abs/10.1111/1467-8659.00180

[88] A. Berk, P. Conforti, R. Kennett, T. Perkins, F. Hawes, and J. van den Bosch, “Modtran® 6: A major upgrade of the modtran® radiative transfer code,” in *2014 6th Workshop on Hyperspectral Image and Signal Processing: Evolution in Remote Sensing (WHISPERS)*, 2014, pp. 1–4.

[89] W. H. McMaster, “Polarization and the Stokes Parameters,” *American Journal of Physics*, vol. 22, no. 6, pp. 351–362, Sep. 1954.

[90] M. Toyoshima, H. Takenaka, Y. Shoji, Y. Takayama, Y. Koyama, and H. Kunimori, “Polarization measurements through space-to-ground atmospheric propagation paths by using a highly polarized laser source in space,” *Opt. Express*, vol. 17, no. 25, pp. 22 333–22 340, Dec 2009. [Online]. Available: http://www.osapublishing.org/oe/abstract.cfm?URI=oe-17-25-22333

[91] F. Delgado-Cepeda, “Universal quantum gates for quantum computation on magnetic systems ruled by heisenberg-ising interactions,” *Journal of Physics Conference Series*, vol. 839, p. 012014, 05 2017.

[92] A. Ling, M. Peloso, I. Marcikic, A. Lamas-Linares, and C. Kurtsiefer, “Experimental e91 quantum key distribution,” *Proc SPIE*, 03 2008.

[93] H. Kaushal and G. Kaddoum, “Optical communication in space: Challenges and mitigation techniques,” *IEEE Communications Surveys Tutorials*, vol. 19, pp. 57–96, 08 2016.

[94] S. B. Pope, *Turbulent Flows*. Cambridge University Press, 2000.

[95] I. Toselli, L. Andrews, R. Phillips, and V. Ferrero, “Free space optical system performance for laser beam propagation through non kolmogorov turbulence for uplink and downlink paths,” *Proceedings of SPIE - The International Society for Optical Engineering*, 10 2007.

[96] A. Alexakis and L. Biferale, “Cascades and transitions in turbulent flows,” *Physics Reports*, vol. 767-769, 08 2018.

[97] B. Dubrulle, “Beyond kolmogorov cascades,” *Journal of Fluid Mechanics*, vol. 867, 03 2019.

[98] J. Ma, K. Li, L. Tan, S. Yu, and Y. Cao, “Performance analysis of satellite-to-ground downlink coherent optical communications with spatial diversity over gamma–gamma atmospheric turbulence,” *Appl. Opt.*, vol. 54, no. 25, pp. 7575–7585, Sep 2015. [Online]. Available: http://www.osapublishing.org/ao/abstract.cfm?URI=ao-54-25-7575

[99] L. C. Andrews, R. L. Phillips, and C. Y. Young, “Scintillation model for a satellite communication link at large zenith angles,” *Optical Engineering*, vol. 39, no. 12, pp. 3272 – 3280, 2000. [Online]. Available: https://doi.org/10.1117/1.1327839

[100] S. Wang, P. Huang, T. Wang, and G. Zeng, “Atmospheric effects on continuous-variable quantum key distribution,” *New Journal of Physics*, vol. 20, no. 8, p. 083037, aug 2018. [Online]. Available: https://doi.org/10.1088/1367-2630/aad9c4

[101] M. Q. Vu, T. V. Pham, N. T. Dang, and A. T. Pham, “Design and performance of relay-assisted satellite free-space optical quantum key distribution systems,” *IEEE Access*, vol. 8, pp. 122 498–122 510, 2020.

[102] C. Erven, B. Heim, E. Meyer-Scott, J. P. Bourgoin, R. Laflamme, G. Weihs, and T. Jennewein, “Studying free-space transmission statistics and improving free-space quantum key distribution in the turbulent atmosphere,” *New Journal of Physics*, vol. 14, no. 12, p. 123018, Dec 2012. [Online]. Available: http://dx.doi.org/10.1088/1367-2630/14/12/123018

[103] A. A. Semenov and W. Vogel, “Entanglement transfer through the turbulent atmosphere,” *Physical Review A*, vol. 81, no. 2, Feb 2010. [Online]. Available: http://dx.doi.org/10.1103/PhysRevA.81.023835

[104] A. Mukherjee, S. Kar, and V. Jain, “Analysis of beam wander effect in high turbulence for fso communication link,” *IET Communications*, vol. 12, 09 2018.

[105] D. Y. Vasylyev, A. A. Semenov, and W. Vogel, “Toward global quantum communication: Beam wandering preserves nonclassicality,” *Physical Review Letters*, vol. 108, no. 22, Jun 2012. [Online]. Available: http://dx.doi.org/10.1103/PhysRevLett.108.220501

[106] K. Inoue, “Quantum key distribution technologies,” *Selected Topics in Quantum Electronics, IEEE Journal of*, vol. 12, pp. 888 – 896, 08 2006.

[107] R. Davies and M. Kasper, “Adaptive optics for astronomy,” *Annual Review of Astronomy and Astrophysics*, vol. 50, no. 1, p. 305–351, Sep 2012. [Online]. Available: http://dx.doi.org/10.1146/annurev-astro-081811-125447

[108] K. Jackson, C. Correia, O. Lardière, D. Andersen, and C. Bradley, “Linear prediction of atmospheric wave-fronts for tomographic adaptive optics systems: modelling and robustness assessment,” *Opt. Lett.*, vol. 40, no. 2, pp. 143–146, Jan 2015. [Online]. Available: http://ol.osa.org/abstract.cfm?URI=ol-40-2-143

[109] F. Rigaut and B. Neichel, “Multiconjugate adaptive optics for astronomy,” *Annual Review of Astronomy and Astrophysics*, vol. 56, no. 1, pp. 277–314, 2018. [Online]. Available: https://doi.org/10.1146/annurev-astro-091916-055320

[110] O. Guyon and J. Males, “Adaptive optics predictive control with empirical orthogonal functions (eofs),” 2017.

[111] V. Reddy, J.-Y. Li, L. Le Corre, J. E. Scully, R. Gaskell, C. T. Russell, R. S. Park, A. Nathues, C. Raymond, M. J. Gaffey, H. Sierks, K. J. Becker, and L. A. McFadden, "Comparing dawn, hubble space telescope, and ground-based interpretations of (4) vesta," *Icarus*, vol. 226, no. 1, pp. 1103–1114, 2013. [Online]. Available: https://www.sciencedirect.com/science/article/pii/S0019103513003205

[112] M. Greenhouse, "The james webb space telescope: Mission overview and status," in *2019 IEEE Aerospace Conference*, 2019, pp. 1–13.

[113] L. Montier, B. Mot, P. de Bernardis, B. Maffei, G. Pisano, F. Columbro, J. E. Gudmundsson, S. Henrot-Versillé, L. Lamagna, J. Montgomery, and et al., "Overview of the medium and high frequency telescopes of the litebird space mission," *Space Telescopes and Instrumentation 2020: Optical, Infrared, and Millimeter Wave*, Dec 2020. [Online]. Available: http://dx.doi.org/10.1117/12.2562243

[114] S. Lohani and R. T. Glasser, "Turbulence correction with artificial neural networks," *Opt. Lett.*, vol. 43, no. 11, pp. 2611–2614, Jun 2018. [Online]. Available: http://ol.osa.org/abstract.cfm?URI=ol-43-11-2611

[115] W. Xiong, D. Fan, P. Wang, M. Cheng, J. Liu, Y. He, X. Zhou, J. Xiao, Y. Li, and S. Chen, "Convolutional neural network based atmospheric turbulence compensation for optical orbital angular momentum multiplexing," *Journal of Lightwave Technology*, vol. PP, pp. 1–1, 01 2020.

[116] X. Liu, T. Morris, C. Saunter, F. J. de Cos Juez, C. González-Gutiérrez, and L. Bardou, "Wavefront prediction using artificial neural networks for open-loop adaptive optics," *Monthly Notices of the Royal Astronomical Society*, vol. 496, no. 1, p. 456–464, Jun 2020. [Online]. Available: http://dx.doi.org/10.1093/mnras/staa1558

[117] M. Aftab, H. Choi, R. Liang, and D. W. Kim, "Adaptive shack-hartmann wavefront sensor accommodating large wavefront variations," *Opt. Express*, vol. 26, no. 26, pp. 34 428–34 441, Dec 2018. [Online]. Available: http://www.opticsexpress.org/abstract.cfm?URI=oe-26-26-34428

[118] M. Chen, X. Jin, and Z. Xu, "Investigation of convolution neural network-based wavefront correction for fso systems," in *2019 11th International Conference on Wireless Communications and Signal Processing (WCSP)*, 2019, pp. 1–6.

[119] H. Ma, H. Liu, Y. Qiao, X. Li, and W. Zhang, "Numerical study of adaptive optics compensation based on convolutional neural networks," *Optics Communications*, vol. 433, pp. 283–289, 2019. [Online]. Available: https://www.sciencedirect.com/science/article/pii/S0030401818309118

[120] R. Swanson, M. Lamb, C. Correia, S. Sivanandam, and K. Kutulakos, “Wavefront reconstruction and prediction with convolutional neural networks,” in *Adaptive Optics Systems VI*, ser. Society of Photo-Optical Instrumentation Engineers (SPIE) Conference Series, L. M. Close, L. Schreiber, and D. Schmidt, Eds., vol. 10703, Jul. 2018, p. 107031F.

[121] T. Helin, S. Kindermann, J. Lehtonen, and R. Ramlau, “Atmospheric turbulence profiling with unknown power spectral density,” *Inverse Problems*, vol. 34, no. 4, p. 044002, mar 2018. [Online]. Available: https://doi.org/10.1088/1361-6420/aaaf88

[122] H. Kaushal and G. Kaddoum, “Optical communication in space: Challenges and mitigation techniques,” *IEEE Communications Surveys Tutorials*, vol. 19, no. 1, pp. 57–96, 2017.

[123] S. Wang, P. Huang, T. Wang, and G. Zeng, “Atmospheric effects on continuous-variable quantum key distribution,” *New Journal of Physics*, vol. 20, no. 8, p. 083037, aug 2018. [Online]. Available: https://doi.org/10.1088/1367-2630/aad9c4

[124] I. Toselli, L. C. Andrews, R. L. Phillips, and V. Ferrero, “Free space optical system performance for laser beam propagation through non Kolmogorov turbulence for uplink and downlink paths,” in *Atmospheric Optics: Models, Measurements, and Target-in-the-Loop Propagation*, S. M. Hammel, A. M. J. van Eijk, M. T. Valley, and M. A. Vorontsov, Eds., vol. 6708, International Society for Optics and Photonics. SPIE, 2007, pp. 17 – 28. [Online]. Available: https://doi.org/10.1117/12.732595

[125] M. J. Jee and J. A. Tyson, “Toward precision lsst weak-lensing measurement. i. impacts of atmospheric turbulence and optical aberration,” *Publications of the Astronomical Society of the Pacific*, vol. 123, no. 903, pp. 596–614, 2021/08/21/ 2011, full publication date: May 2011. [Online]. Available: https://doi.org/10.1086/660137

[126] F. Rigaut, B. Neichel, M. Boccas, C. d’Orgeville, F. Vidal, M. A. van Dam, G. Arriagada, V. Fesquet, R. L. Galvez, G. Gausachs, C. Cavedoni, A. W. Ebbers, S. Karewicz, E. James, J. Lührs, V. Montes, G. Perez, W. N. Rambold, R. Rojas, S. Walker, M. Bec, G. Trancho, M. Sheehan, B. Irarrazaval, C. Boyer, B. L. Ellerbroek, R. Flicker, D. Gratadour, A. Garcia-Rissmann, and F. Daruich, “Gemini multiconjugate adaptive optics system review – I. Design, trade-offs and integration,” *Monthly Notices of the Royal Astronomical Society*, vol. 437, no. 3, pp. 2361–2375, 11 2013. [Online]. Available: https://doi.org/10.1093/mnras/stt2054

[127] B. Rowe, M. Jarvis, R. Mandelbaum, G. M. Bernstein, J. Bosch, M. Simet, J. E. Meyers, T. Kacprzak, R. Nakajima, J. Zuntz, and et al., “Galsim: The modular galaxy image simulation toolkit,” Jun 2018. [Online]. Available: https://kilthub.cmu.edu/articles/journal_contribution/GALSIM_The_modular_galaxy_image_simulation_toolkit/6506855/1

[128] N. A. Roddier, “Atmospheric wavefront simulation using Zernike polynomials,” *Optical Engineering*, vol. 29, no. 10, pp. 1174 – 1180, 1990. [Online]. Available: https://doi.org/10.1117/12.55712

A

Integrator systematic error in orbit propagator

Mean error between RK89 and RK-DP78

Mean error for S/C orbit propagation between RK89 and RK-DP78 integrators leading to Table 2.5.

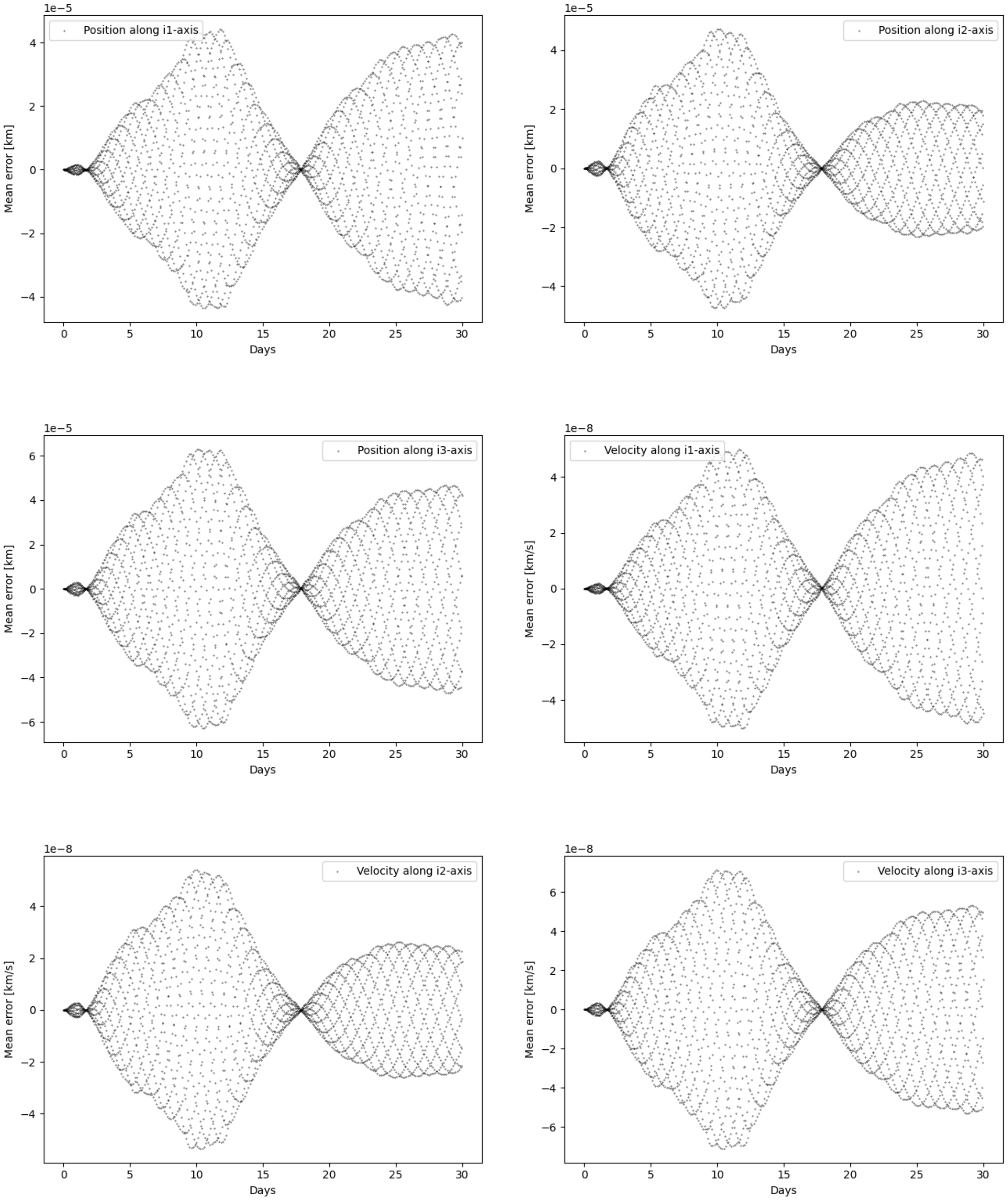

Figure A.1: Mean error in position and velocity components along $\hat{i_1}, \hat{i_2}, \hat{i_3}$ axis between RK89 and RK-DP78 integrators.

Mean error between RK89 and RK-DP45

Mean error for S/C orbit propagation between RK89 and RK-DP45 integrators leading to Table 2.5.

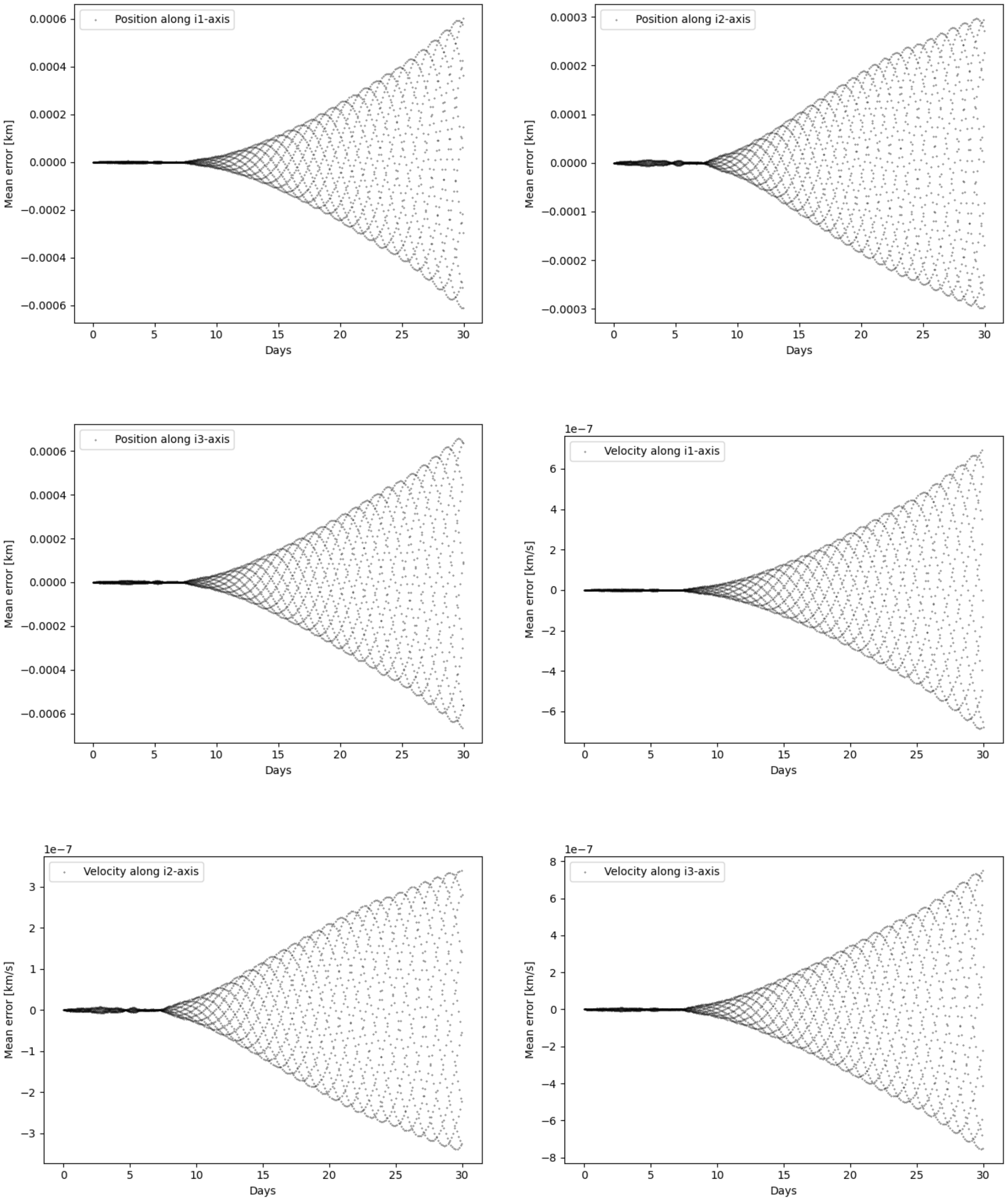

Figure A.2: Mean error in position and velocity components along $\hat{i_1}, \hat{i_2}, \hat{i_3}$ axis between RK89 and RK-DP45 integrators.

Mean error between RK89 and RK-DP853

Mean error for S/C orbit propagation between RK89 and RK-DP853 integrators leading to Table 2.5.

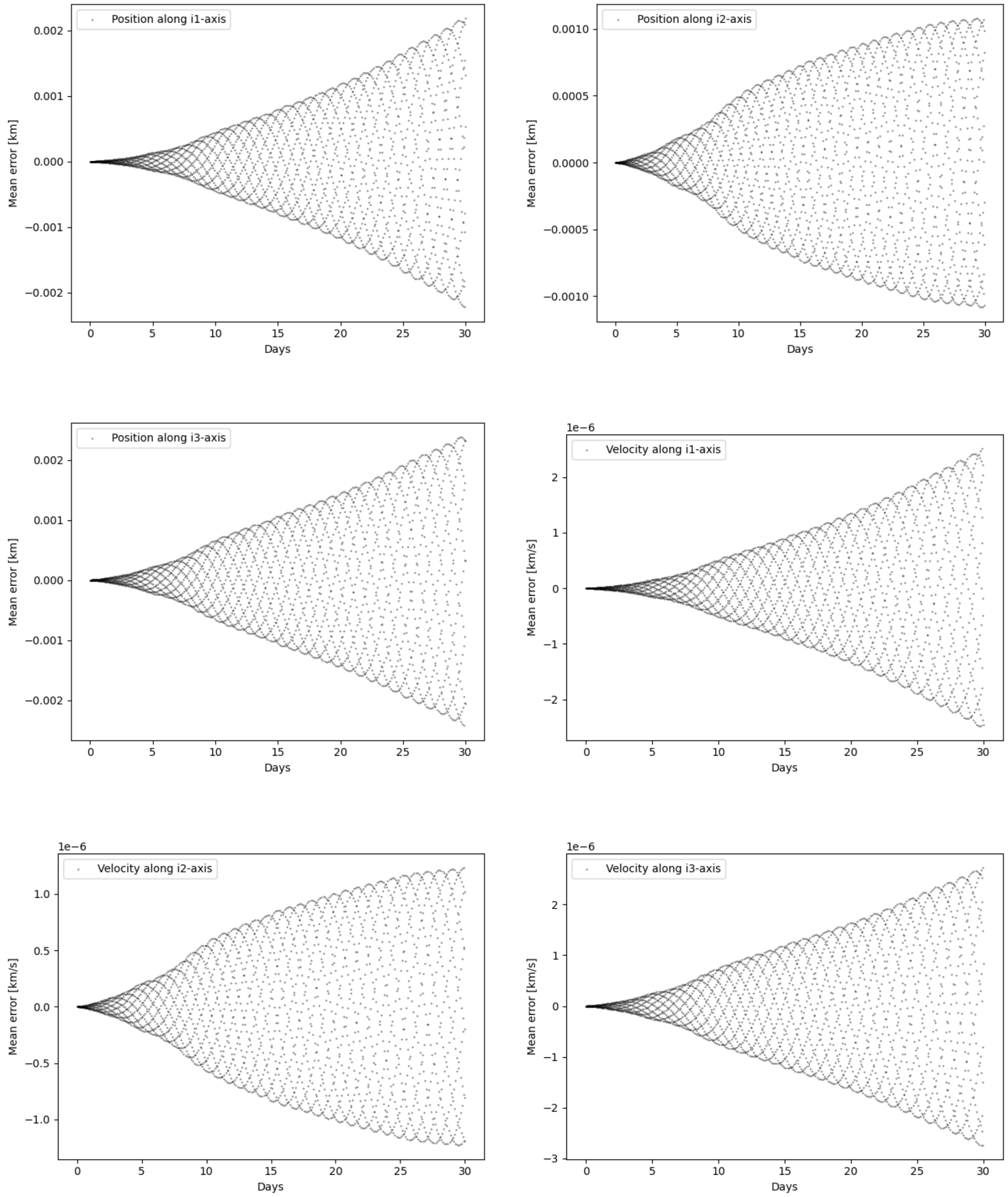

Figure A.3: Mean error in position and velocity components along $\hat{i_1}, \hat{i_2}, \hat{i_3}$ axis between RK89 and RK-DP853 integrators.

Mean error between RK89 and RK4

Mean error for S/C orbit propagation between RK89 and RK4 integrators leading to Table 2.5.

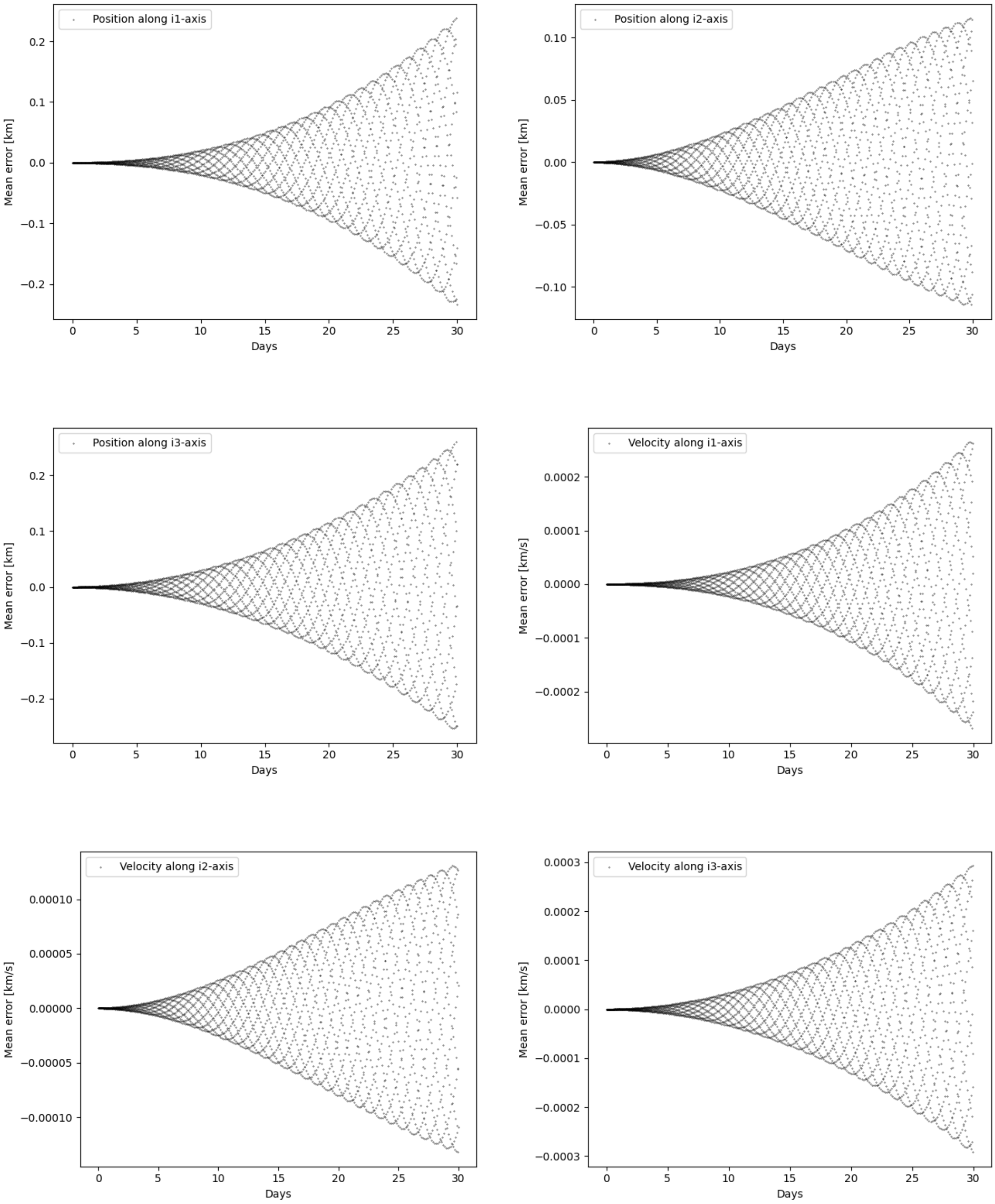

Figure A.4: Mean error in position and velocity components along $\hat{i}_1, \hat{i}_2, \hat{i}_3$ axis between RK89 and RK4 integrators.

B

DRAMA - OSCAR tool results

OSCAR - 400 km end of orbit

End-of-life cycle analysis from chapter 2 of the 400 km orbit for different parameters using DRAMA.

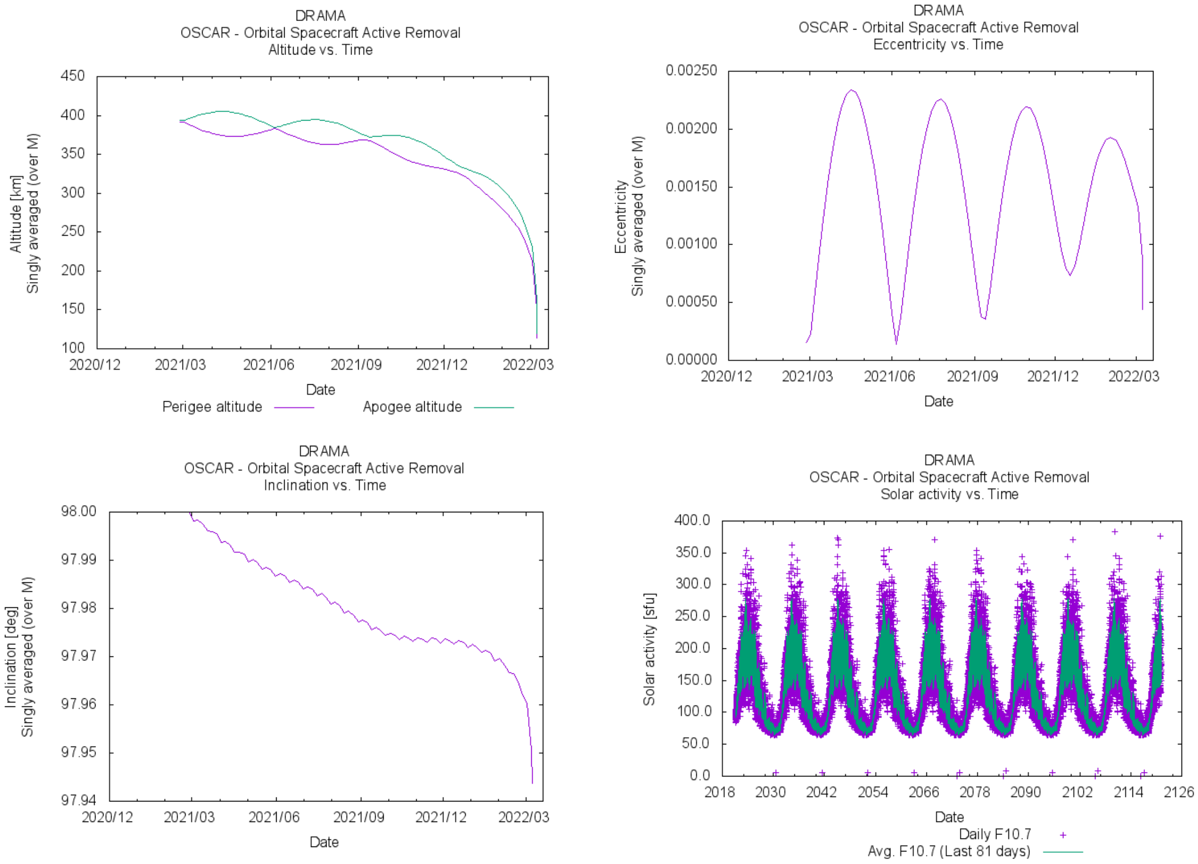

Figure B.1: Altitude, eccentricity, inclination and solar activity over time for altitude of 400 km.

OSCAR - 500 km end of orbit

End-of-life cycle analysis from chapter 2 of the 500 km orbit for different parameters using DRAMA.

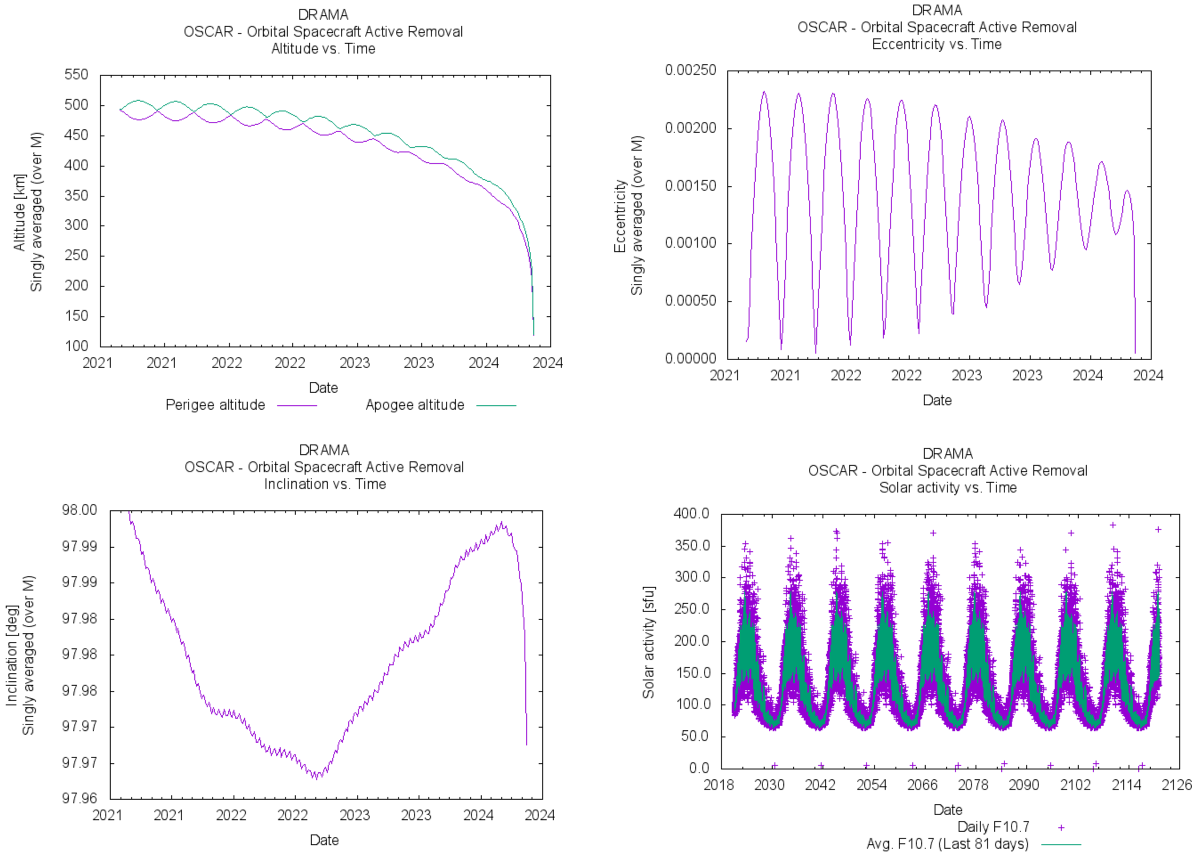

Figure B.2: Altitude, eccentricity, inclination and solar activity over time for altitude of 500 km.

OSCAR - 600 km end of orbit

End-of-life cycle analysis from chapter 2 of the 600 km orbit for different parameters using DRAMA.

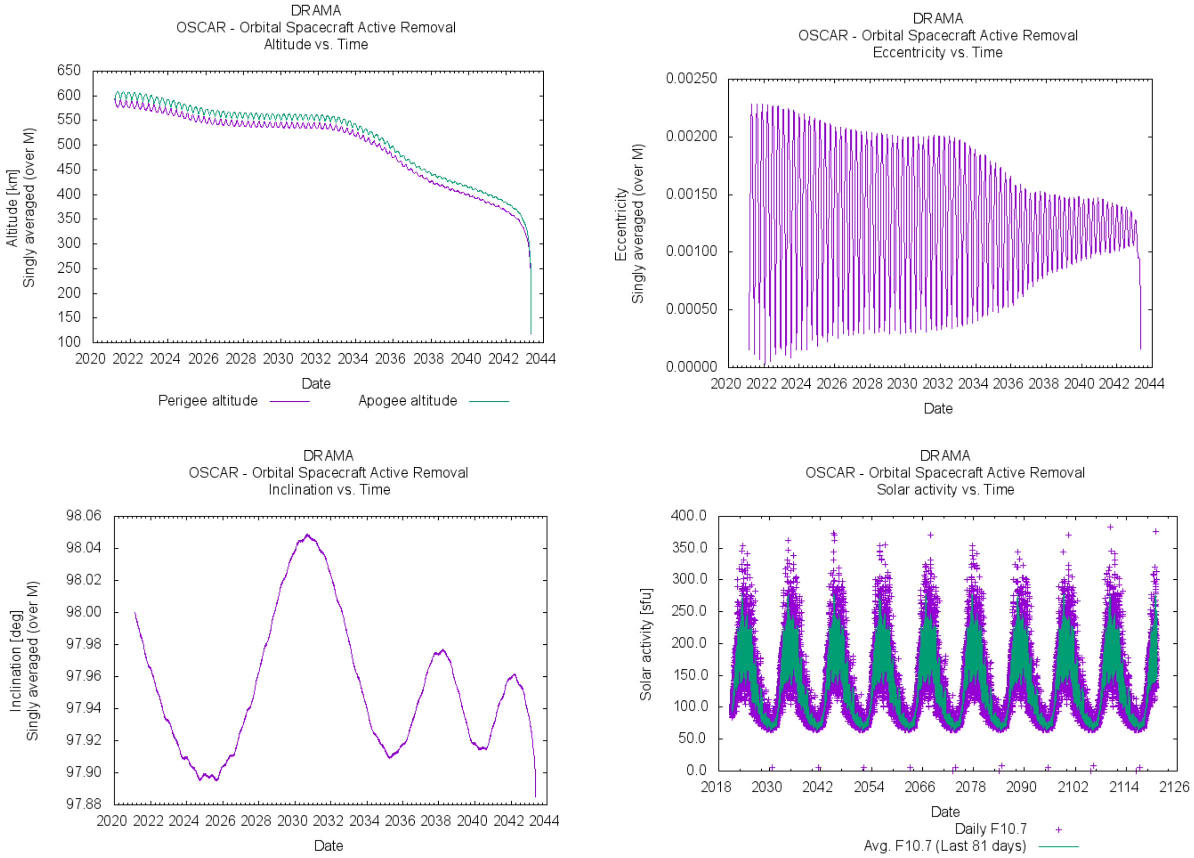

Figure B.3: Altitude, eccentricity, inclination and solar activity over time for altitude of 600 km.